Advanced Numerical and Experimental Beam Dynamics Investigations for the CW-Heavy Ion Linac HElmholtz LInear ACcelerator

Dissertation
zur Erlangung des Grades
„Doktor der Naturwissenschaften“
am Fachbereich Physik, Mathematik und Informatik
der Johannes Gutenberg-Universität
in Mainz

Simon F. Lauber
geb. in Frankfurt a. M.

Mainz, den 21.04.2022

Betreuer:	Prof. Dr. Winfried Barth
Gutachter:	Prof. Dr. Michael Ostrick
Prüfungsdatum:	07.10.2022

Zusammenfassung

In enger Zusammenarbeit von **GSI** Helmholtzzentrum für Schwerionenforschung (GSI) und **H**elmholtz-**I**nstitut **M**ainz (HIM) mit dem **I**nstitut für **A**ngewandte **P**hysik Frankfurt (IAP) wird am GSI Standort Darmstadt ein Dauerstrich-Linearbeschleuniger, der sogenannte **HE**lmholtz **LI**near **AC**celerator (HELIAC), gebaut. Dieser Linearbeschleuniger, der aus einem normalleitenden Injektor und einem supraleitenden Hauptbeschleuniger besteht, wird Dauerstrich-Schwerionenstrahlen für die Erforschung und Entdeckung von superschweren Elementen liefern. Ein wesentlicher Teil der Entwicklungsarbeiten wurde für den supraleitenden Linac-Teil mit dem Entwurf und der Konstruktion der ersten supraleitenden **C**rossbar **H**-mode (CH) Resonatoren mit einer speziell für eine variable Ausgangsenergie entwickelten **EQU**idistant m**U**ltigap **S**tructure (EQUUS) Strahldynamik bereits abgeschlossen. Der Linearbeschleuniger ist so konzipiert, dass er sich für Experimente auf dem Gebiet der Forschung an superschweren Elementen und für die Materialwissenschaften eignet und bietet im Dauerstrichbetrieb eine variable Beschleuniger-Ausgangsenergie im Bereich von 3.5 MeV/u bis 7.3 MeV/u, eine niedrige Energieunschärfe von ± 3 keV/u. Aufgrund der Anwendung von supraleitenden Komponenten hat der HELIAC hohe Anforderungen an die Strahltransmission, die nur durch eine geignete Strahlanpassung an die supraleitende Sektion erreicht werden kann. Diese Arbeit befasst sich hauptsächlich mit der Injektion in die supraleitende HELIAC-Sektion, d.h. mit der Vermessung und Optimierung des Strahltransports und dem Entwurf des normalleitenden Injektor-Linacs. Dazu wird ein im Rahmen der vorliegenden Arbeit entwickelter Rekonstruktionsalgorithmus zur Berechnung der Parameter der longitudinalen Teilchendichteverteilung und dessen Implementierung bzw. praktische Anwendung vorgestellt, der sowohl für die Optimierung des aktuellen HLI Injektors als auch des zukünftigen Standalone-HELIAC-Injektors geeignet ist. Darüber hinaus wurde ein neuartiges Strahlkollimationssystem entworfen und in Betrieb genommen, welches zur strahlbasierten Ausrichtung (Beam-Based Alignment) mittels eines sogenannten Pencil Beams verwendet werden soll. Schließlich wird das im Rahmen der Arbeit neu erstellte Design des normal leitenden Injektor Linacs vorgestellt, bei dem ein aus zwei **I**nterdigital **H**-mode (IH) Kavitäten bestehender Driftröhrenbeschleuniger mit **A**lternierender **P**hasen**F**okussierung (APF) zum Einsatz kommt. Besonderer Wert wurde dabei auf optimale Strahleigenschaften gelegt - durch Minimierung des Emittanzwachstums entlang des Driftröhrenbeschleunigers und der damit einhergehende Verbesserung der Strahlbrillianz wird so die Leistung des HELIAC erheblich verbessert werden.

Abstract

In close collaboration of **GSI** Helmholtz Centre for Heavy Ion Research (GSI) and **H**elmholtz **I**nstitute **M**ainz (HIM) with the **I**nstitute for **A**pplied **P**hysics Frankfurt (IAP) a continuous wave linear accelerator, the so-called **HE**lmholtz **LI**near **AC**celerator (HELIAC), is being built at the GSI facility in Darmstadt. This linear accelerator, consisting of an normal-conducting injector and an superconducting main accelerator, will provide continuous wave heavy ion beams for the research and discovery of **S**uper**H**eavy **E**lements (SHE). A significant part of the engineering development has already been completed for the superconducting linac part with the design and construction of the first superconducting **C**rossbar **H**-mode (CH) resonators with **EQU**idistant m**U**ltigap **S**tructure (EQUUS) beam dynamics, specifically developed for a variable output energy. The linear accelerator is designed to be suitable for experiments in the field of SHE research and materials science and offers a variable accelerator output energy in the range of 3.5 MeV/u to 7.3 MeV/u, a low energy uncertainty of ± 3 keV/u and continuous wave operation. Due to the application of superconducting components, the HELIAC has high beam transmission requirements, which can only be achieved by smart beam matching to the superconducting section. This work is mainly concerned with the injection into the superconducting HELIAC section, i.e., with the measurement and optimization of the beam transport and with the design of the normal-conducting injector linac. For this purpose, a reconstruction algorithm is developed in this thesis to calculate the parameters of the longitudinal particle density-distribution. Its implementation and practical application are presented, which is suitable for the optimization of both the current HLI injector and the future standalone HELIAC injector. Furthermore, a novel beam collimation system has been designed and put into operation, which will be used for beam-based alignment by means of a so-called pencil beam. Finally, the new design of the normal-conducting injector linac created in the course of the thesis is presented, using a drift-tube accelerator consisting of two **I**nterdigital **H**-mode (IH) cavities with **A**lternating **P**hase **F**ocusing (APF) beam dynamics. Special emphasis was placed on optimal beam characteristics. By minimizing the emittance growth along the drift-tube accelerator and the consequent improvement of the beam brilliance, the performance of the HELIAC can be significantly improved.

Contents

1. Introduction

For the synthesis of **S**uper**H**eavy **E**lements (SHE), collision experiments are performed on solid heavy ion targets with ion beams of intermediate to heavy masses. New heavy elements are obtained from fusion evaporation reactions with extremely low effective cross-sections. The probability of generating new elements is low. Therefore, stable, long-term and **C**ontinuous **W**ave (CW) operation is essential in order to perform SHE experiments with the highest particle mass in the future [1, 2].
The **GSI** Helmholtz Centre for Heavy Ion Research (GSI) substantially expands the existing accelerator facility with the construction of the large-scale **F**acility for **A**ntiproton and **I**on **R**esearch at Darmstadt (FAIR) project. This involves an upgrade of the existing **UNI**versal **L**inear **AC**celerator (UNILAC) for high pulse-current short pulse-length operation as part of the injector chain for the 100 T m synchrotron SIS100 of the FAIR facility [3–8].
With these new operational scopes, the UNILAC does not meet the demands of SHE research in terms of high repetition rate and long beam pulses at very high average particle current. Therefore, a new CW capable heavy ion accelerator is essential to fulfill the requirements of the SHE research at GSI.
In order to meet the requirements for the production of superheavy elements, a dedicated heavy ion CW linear accelerator is under construction. To provide beams for SHE experiments, the **HE**lmholtz **LI**near **AC**celerator (HELIAC) is going to be built at GSI Darmstadt: a **S**uper**C**onducting (SC) CW heavy-ion linear accelerator with variable output energy [9–11], comprising a normal-conducting injector linac and an SC main linac comprising four cryomodules, equipped with SC **C**rossbar **H**-mode (CH) cavities and SC solenoids [11].
A cooperation of multiple institutes is devoted to the R&D for this new accelerator, namely the GSI and **H**elmholtz **I**nstitute **M**ainz (HIM) [12, 13] under support of the **I**nstitute for **A**pplied **P**hysics Frankfurt (IAP) [14, 15] and formerly in collaboration with **K**urchatov **I**nstitute - **I**nstitute for **T**heoretical and **E**xperimental **P**hysics (KI-ITEP, Moscow) and **M**oscow **E**ngineering **Ph**ysics **I**nstitute (MEPhI, Moscow) [16, 17]. The application of SC linear accelerators is a crucial technology at several international accelerator-driven scientific institutions, as for boron neutron capture therapy, medium-energy applications in materials science, spallation neutron sources and isotope generation. Many of these ambitious accelerators rely significantly on state-of-the-art technology and precision machining of SC and/or CW multi-gap cavities [18–27]. As the first SC accelerator at GSI, HELIAC increases the number of already existing and planned advanced linacs at this research center: UNILAC [28–30], FAIR proton linac, linear decelerator **H**eavy **I**on **TRAP** (HITRAP) [31] and **L**aser **I**on **G**eneration, **H**andling and **T**ransport (LIGHT) [32].

1.1. Superheavy Ion Research

An essential part of the research on **S**uper**H**eavy **E**lements (SHE) is the synthesis of new, stable elements with a mass number above 103, also known as transactinide elements. Since the first discovery of element 103, Lawrencium [33], at the Lawrence Berkeley National Laboratory and Joint Institute for Nuclear Research in Dubna, up to now, 15 further superheavy elements have been reported to be discovered, of which twelve have been accepted and named by the International Union of Pure and Applied Chemistry.
The elements are formed in fusion reactions, in which two lighter elements have to overcome the Coulomb repulsion force to fuse. The majority of the fusion nuclei are not stable and decay into other elements. The low probability to produce a new superheavy nucleon makes new discoveries a considerable challenge, whilst elements with higher atomic numbers are more difficult to produce.
A common setup to produce and detect superheavy elements is to irradiate a target foil with a heavy ion beam at a sufficient beam velocity of roughly 10 % of the speed of light to overcome just about the coulomb barrier. The collision fragments are transported to dedicated experimental installations, either to prove solely the existence of the elements, or to analyze their chemical properties.
These experiments serve to validate and extend our knowledge of the modern, quantum chemical, fully relativistic model of atoms and to probably extend Mendeleev's tables of the elements further towards the *Island of Stability*, a region of proton-neutron composition that produces elements with closed shells, potentially yielding elements with magnitudes higher half-lives than previous superheavy ions.
Since the beginnings of research on superheavy elements in the 1960s, particle accelerators have always played a significant role in order to deliver a heavy ion beam to the interaction targets. The extremely small effective cross-sections of modern SHE experiments require a successive upgrade of the accelerators towards CW operation, which is promoted by recent advances in SC accelerator technology [34, 35].

The leading institutions in this field, such as GSI, the Russian Joint Institute for Nuclear Research, the U.S. Lawrence Berkeley National Laboratory, or the Japanese Rikagaku Kenkyūjo, upgrade and extend their accelerator equipment towards an improved supply of high power, high brilliance particle beams. Six out of the twelve superheavy elements have been discovered at GSI, namely elements 107 to 112 [34, 35].
After the synthesis of element 117 (Tenness [36, 37]) and 118 (Oganesson [38]), current SHE research examines the already discovered elements in more detail and proceeds to the search for the elements 119 and 120 [2, 39].

1.2. Helmholtz Institute Mainz

The **H**elmholtz **I**nstitute **M**ainz (HIM), a joint venture of the Johannes Gutenberg-Universität Mainz and the GSI Darmstadt, is a relatively new research institute built in 2009, in particular in cooperation with the Institut für Kernphysik, which is operating **MA**inzer **MI**krotron (MAMI), the future **M**ainz **E**nergy-Recovering **S**uperconducting **A**ccelerator (MESA).
HIM is dedicated to contributing to the FAIR research branches: Hadron Structure with **E**lectro **M**agnetic **P**robes (EMP), **SPEC**troscopy & **F**lavor (SPECF), **M**atter-**A**nti**M**atter Asymmetry (MAM), **S**uper**H**eavy **E**lements (SHE), **AC**celerator & **I**ntegrated **D**etectors (ACID) and **TH**eory **FL**oor (THFL).
While the SHE group is committed to the experimental part of the SHE research [2, 37], the ACID 1 group provides the key technology for the realization of the accelerator components for the HELIAC [40–44]. A dedicated test bunker to test single superconducting **R**adio **F**requency (RF) resonators as well as a dedicated cleanroom for the installation of up to 13 m long horizontal cryostats are provided at this facility and offer the key infrastructure to the HELIAC-Project.

1.3. GSI Helmholtz Centre for Heavy Ion Research

GSI Helmholtz Centre for Heavy Ion Research (GSI) is one of the main scientific institutions in the field of heavy element research and addresses a wide range of topics:

- Nuclear Physics
- Hadron physics
- Theoretical physics
- Atomic physics
- Plasma Physics
- Materials Research
- Biophysics & Medical Developments
- Information Technology

Currently, the GSI accelerators can provide for pulsed beam operation from two injector linacs: the High Charge State Injector (**H**och**L**adungs**I**njektor, HLI) and the High Current Injector (**H**och**S**trom**I**njektor, HSI). Both injectors are linked to the main accelerator, the UNILAC. An Alvarez-type main linac accelerates the beam from 1.4 MeV/u to 11.4 MeV/u for injection into the SIS18 and is in routine operation since 1975. Since the beginning, UNILAC has delivered heavy ion beams mainly to multiple users in the experimental hall directly behind the Alvarez **D**rift **T**ube **L**inac (DTL), as to the **S**eparator for **H**eavy **I**on Reaction **P**roducts (SHIP) velocity filter

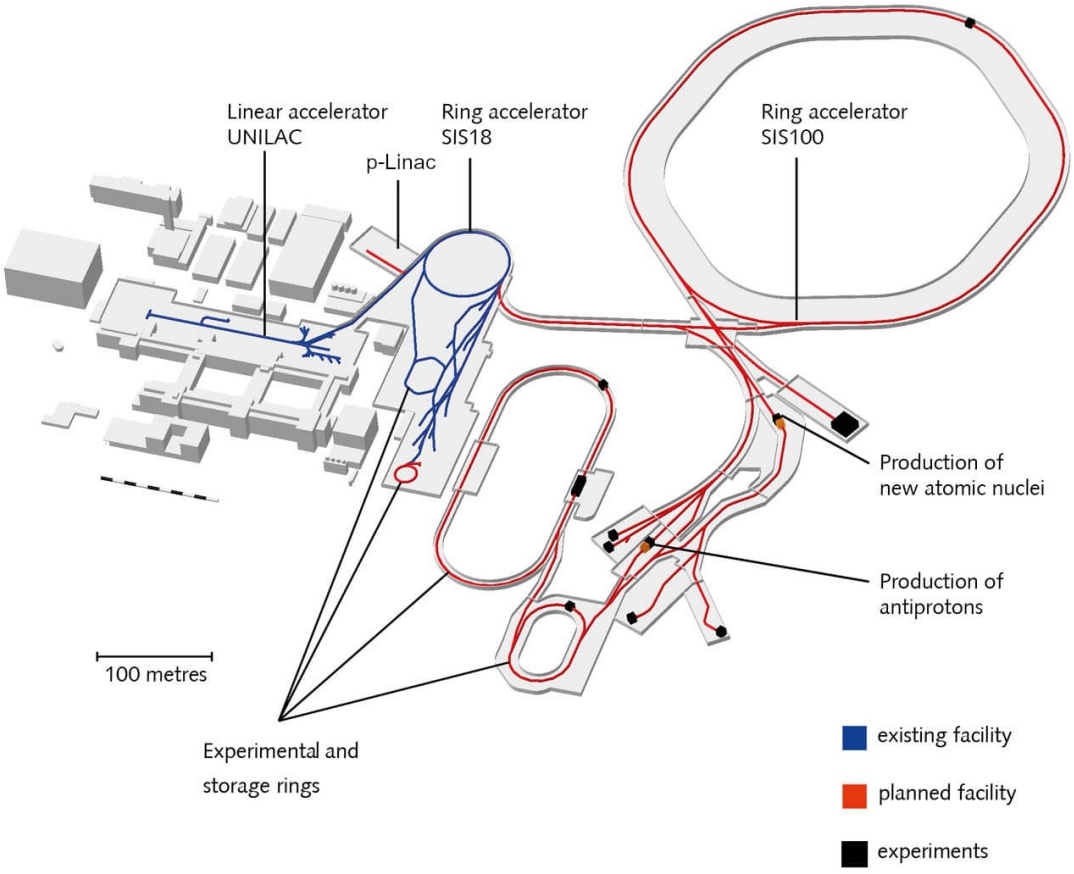

Figure 1.1: Overview of the GSI and the future FAIR complex [45].

and the **T**rans**A**ctinide **S**eparator and **C**hemistry **A**pparatus (TASCA), a recoil separator that is specialized in the synthesis and separation of neutron-rich isotopes of superheavy elements.

The SIS18, a 18 T m synchrotron accelerator with an end energy of 4.7 GeV for protons and 1 GeV/u for uranium (charge state 73+), provides for high energy heavy ion beams up to the highest masses at further experimental sites as the **E**xperimental **S**torage **R**ing (ESR), allowing for in-ring experiments. Furthermore, beam is provided for the **FR**agment **S**eparator (FRS), assisting in the investigation for rare isotopes, and for the **H**ighly charged **I**ons **TRAP** (HITRAP), the **H**igh **A**cceptance **D**i-**E**lectron **S**pectrometer (HADES), the Plasma Physics at GSI and to the medical irradiation room Cave M.

An extended portfolio of experimental sites will be realized with FAIR [46], as with the **C**ompressed **B**arionic **M**atter (CBM) physics program, the **H**igh **A**cceptance **D**i-**E**lectron **S**pectrometer (HADES), the **H**igh **E**nergy **S**torage **R**ing (HESR), the

Anti**P**roton **AN**nihilations at **DA**rmstadt (PANDA) and the **SUPER**conducting **FR**agment **S**eparator (SUPER-FRS), which will significantly extend the campus size (see Figure 1.1). The core accelerator will be the SIS100, providing for end energies of 29 GeV for protons and 2.7 GeV/u for uranium.

1.4. Helmholtz Linear Accelerator

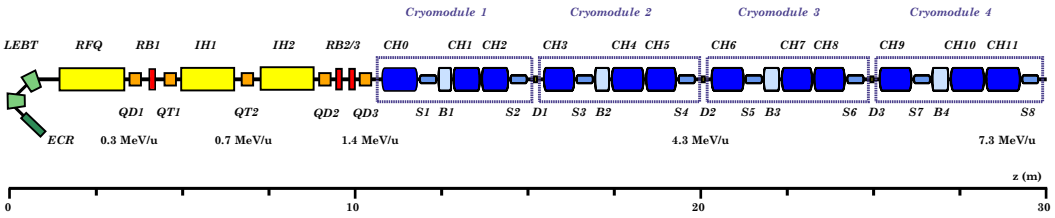

Figure 1.2: Recent design of the HELIAC: the **N**ormal **C**onducting (NC) cavities are shown in yellow and red, the SC section comprising four cryomodules in blue color. ECRIS: Electron Cyclotron Resonance Ion Source, LEBT: Low Energy Beam Transport, RFQ: Radio Frequency Quadrupole, QD: Quadrupole Doublet, RB: NC Rebuncher, QT Quadrupole Triplet, S: Solenoid, B: SC Rebuncher, IH: Interdigital H-Mode Cavity, CH: Crossbar H-Mode Cavity

The **HE**lmholtz **LI**near **AC**celerator (HELIAC) was initially planned as a superconducting extension of the existing GSI HLI injector, as mentioned in prior papers [9–11], to serve as CW linac for the SHE research.
Recent progress has steered the project towards using a new, dedicated injector in the future (see Figure 1.2), providing the possibility to reconsider parts of the beamline. Thus, the most advance in project progress has been made towards the SC section with the design and construction of the SC CH cavities with the **EQU**idistant m**U**ltigap **S**tructure (EQUUS) beam dynamics scheme (see Section 3.3 on page 37), specially developed for a variable output energy under strong support of the IAP.
Multiple R&D stages have been completed for the SC part, as the resonator RF testing in a vertical cryostat at IAP and a horizontal cryostat at GSI, the worldwide first CH resonator beam test with an 1.4 MeV/u Argon beam at GSI (supplied by the HLI injector and delivered to the adjacent *CW Demonstrator*, see Section 1.4.1) and also the tests of the first horizontal HELIAC-cryostat, comprising four SC CH resonators as well as an SC solenoid in an extended test bunker, the *Advanced Demonstrator*.
The core features of the fully equipped accelerator (see Table 1.1) are designed for an optimal supply of SHE and material science user experiments. Thus, HELIAC offers a variable output beam energy, a low energy spread and CW operation.
It is foreseen to use the existing buildings GSI **S**tripper-**H**all (SH) SH1 and SH2, which

Table 1.1: HELIAC design specifications

Property	Value
Frequency	108.408 MHz (216.816 MHz[1])
Mass-to-charge ratio	1 to 6
Repetition rate	Continuous wave
Max. beam current I	1 mA
Output energy W_{out}	3.5 MeV/u to 7.3 MeV/u
No. of NC IH cavities	2
No. of SC CH cavities	12

[1]The SC CH cavities operate at the second harmonic frequency.

are currently exploited as magnet testing hall for the FAIR SIS100 dipole magnets, to place the HELIAC parallel to the UNILAC, and to fix the injection point into the adjacent beamline in-place of the last single resonator (E10).
The new location allows for a reconsideration of the transport section from **R**adio **F**requency **Q**uadrupole (RFQ) output to CH input. This section is very critical for a redesign. It allows reducing the overall accelerator length by an optimal transport section layout, as well as a preserving the emittance with enhanced **I**nterdigital **H**-mode (IH) accelerator technology for improved beam quality and transmission along the SC HELIAC. Taking the special requirements into account, resulting from the use of SC technology and CW application, the SC HELIAC has the highest demands to the beam transmission, which can only be resolved by a proper commissioning, minimizing misalignment of the elements along the line and matching to the section. Thus, this thesis addresses these challenges by:

- A new reconstruction algorithm for the determination of the longitudinal beam parameters and density-distribution, suitable both for the optimization of linear accelerators and for the precise beam matching to the SC section [47].
- A dynamic collimation system for the commissioning and alignment of the individual cryostats and for further beam experiments [48].
- The rework of the matching section to the SC HELIAC towards a minimum length whilst maintaining full 6D matching capabilities [49].
- The design of an **A**lternating **P**hase **F**ocusing (APF) IH resonator chain providing for minimal emittance growth, significantly improving the SC HELIAC performance by reducing potential limitations due to non-optimal beam transmission [49].

1.4.1. Demonstrator

Figure 1.3: Cross-section of the HELIAC CH cavities. Demonstrator cavity CH0 [50] (*left*) and CH2 [51] (*right*); both to be placed in the cryomodule CM1.

The performance of the newly developed SC CH resonator (see Figure 1.3) was proven within the scope of the Demonstrator project. The tested multi-gap resonator type represents a new R&D milestone in the complexity of SC resonator geometries and introduces a new beam dynamics design as well, namely EQUUS beam dynamics [14] (see Section 3.3). The design aim of this geometric configuration was to optimize the overall linac compactness by increasing the number of gaps per SC cavity, which previously did not exceed four gaps [15]. Cavities with the magnetic $H_{2,1}$ mode [52] were chosen to realize the multi-gap cavities.
Their normal-conducting counterpart, with a different embedded beam dynamics concept, was already proven to provide for efficient acceleration [53] for low to medium beam energies and provides for increased stability through the crossbar stem layout, beneficial to reduce frequency detuning from ambient pressure and Lorentz-force.

The research on SC CH cavities was accomplished in an experimental setup using a horizontal and vertical test cryostat at GSI and IAP. The focus was on the evaluation of all relevant RF parameters and performance in a vertical cryostat at IAP [54], which revealed a real estate gradient of up to 10 MV/m (almost twice the design gradient). Furthermore, a beam test of the first cavity CH0 was performed at GSI, employing the existing HLI Injector, one of the two GSI injectors linacs [52, 55, 56], which delivers a heavy ion beam at a beam energy of 1.4 MeV/u.
This beam test performed in 2017 marked a major milestone for the HELIAC-project and confirmed the EQUUS beam dynamics approach, allowing an acceleration gradient beyond the design criteria [9]. Exceeding the expectations, the tests paved the way for extensive testing of an upgraded setup, the *Advanced Demonstrator* (see Figure 1.4).

1.4.2. Advanced Demonstrator

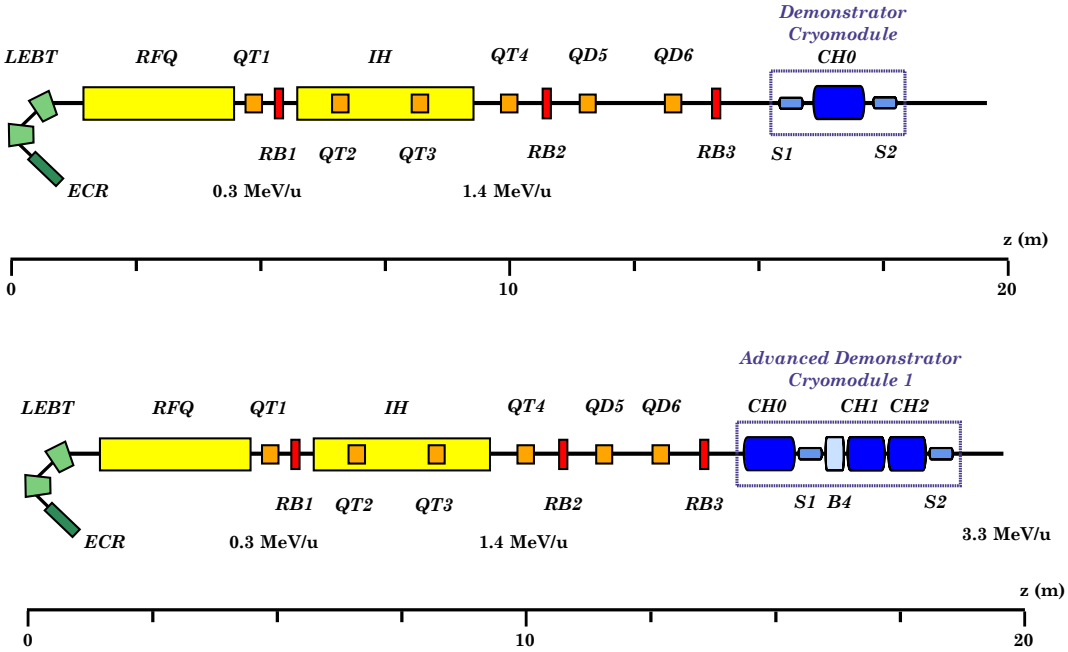

Figure 1.4: Demonstrator (CH0) and Advanced Demonstrator (CH0, CH1, CH2, SC rebuncher) beamlines: the HLI Injector [57] (until 1.4 MeV/u) is temporarily used as injector for the (Advanced) Demonstrator cryomodule.

The next milestone for the HELIAC project could be reached with construction of an extended version of the previously used CW Demonstrator bunker, the so-called *Advanced Demonstrator* (see Figure 1.4 and Table 1.2), providing the key infrastructure for a fully equipped horizontal cryostat with four SC CH cavities and a full scale cryogenic system to supply the HELIAC Advanced Demonstrator with liquid Helium at 4 K.

Multiple commissioning runs towards the final cryostat test[1] have been carried out, allowing for beam tests and preparatory emittance measurements in order to provide for full 6D matching to the acceptance of the Advanced Demonstrator. Dedicated beam diagnostics are already installed to determine the Demonstrator performance, as the **B**unch **S**hape **M**onitor (BSM) of Feschenko-type [58], as well as the **MOB**ile **EMI**ttance Measurement Device (MobEmi) [59], providing together for precise detection on both longitudinal and transverse beam parameters (see Section 5 and Section 7).

[1] scheduled for Q2 2022

Table 1.2: Advanced Demonstrator specifications

Property	Value
Frequency	108.408 MHz (216.816 MHz[1])
Mass-to-charge ratio	1 to 6
Repetition rate	100 % ($\leq$25 %[2])
Output energy W_{out}	1.4 MeV/u to 3.3 MeV/u
No. of SC CH cavities	4

[1]The SC CH cavities operate at the second harmonic frequency.

[2]The repetition rate is limited by the temporarily used injector.

The use of three SC CH (accelerating) cavities, one SC rebuncher and two SC solenoids, allow for an acceleration up to 2.7 MeV/u of heavy ions at a mass-to-charge ratio of up to 6 and 3.3 MeV/u for a mass-to-charge ratio of 3 [11]. First user experiments are foreseen using the Advanced Demonstrator cryomodule. Detailed beam simulations are used to design the project with in-depth insight into the EQUUS resonators beam dynamics and for the best overall performance of the linac [47, 60, 61].

2. Modern Heavy Ion Linacs

A considerable part of this work deals either with the analysis of existing accelerating- and beamline-sections or with the design of future accelerator systems at GSI. Therefore, the major formalism related to the transport and acceleration of heavy ion beams with low β ranging from 0.01 to 0.5 are discussed in this section. In addition, the standard components for modern hadron linear accelerators are presented in this chapter.

2.1. Ion Sources

A heavy ion source and its beam extraction-system typically deliver a low-energy beam, in the regime of a few hundred electronvolts, electrostatically post accelerated and afterwards usually matched into an RFQ accelerator. There are several types of ion sources, determined for the use of a wide variety of (heavy) ion accelerators. GSI operates the following ion sources:

- **E**lectron **C**yclotron **R**esonance **I**on **S**ource (ECRIS)
- Arc Sources
  - **ME**tal **V**apor **V**acuum **A**rc Ion Source (MEVVA)
  - **V**acuum **AR**c **I**on **S**ource (VARIS)
- **P**enning **I**onization **G**auge (PIG)
- Filament Driven
  - **MU**lti **C**usp **I**on **S**ource (MUCIS)
  - **C**old or **HO**t **R**eflex**D**ischarge **I**on **S**ource (CHORDIS)

Although the technical implementation of these sources varies widely, the principle of operation can be summarized as follows: gaseous, liquid, or solid material is introduced into a volume and, through suitable processes such as evaporation or sputtering, provides the particles to be ionized. The ionization energy must be supplied to the material from an energy source (e.g., by an incident electron beam, electromagnetic radiation, electron bombardment, etc.), whereas the specific ionization process depends on the type of ion source. After ionization, the ions are extracted from the plasma by an electrostatic extraction system and, if necessary, post acceleration is employed [62].

A figure of merit for ion sources, operated at each particle accelerator, is the extracted beam current I and the according emittance $\hat{\epsilon}$ (which is a product of

beam size and its energy width, see Section 3.1 on page 26), as these parameters determine the design and the actual performance of the adjacent particle accelerator. A theoretical lower limit of beam emittance delivered by an ion source is given by the beam current I, the Boltzmann constant k_B, the plasma temperature T, the current density J_c, the mass m and the speed of light c [63] (all variables in SI base units):

$$\hat{\epsilon}_{\min} = 2 \cdot 10^6 \sqrt{\frac{I}{\pi J_c} \frac{k_b T}{mc^2}} \quad , [\hat{\epsilon}_{\min}] = \text{mm mrad}. \tag{2.1}$$

The lowest deliverable emittance increases with the beam current, as space charge forces limit the density of the beam, and the intrinsic temperature leads to a non-singular kinetic energy distribution within the beam, increasing the beam emittance as well. However, the beam emittance is governed by the beam transport optics that is adopted as beam extraction-system behind the plasma generator of the ion source, space charge effects are of secondary relevance in practical applications.

The 14.5 GHz CAPRICE ECRIS [64, 65] is the only used high charge state heavy ion source at GSI HLI since 1992, which is also temporarily employed for beam delivery to the Demonstrator and the Advanced Demonstrator.
In an ECRIS ion source, an ionization chamber filled with gas is employed, which is either directly injected into the ionization chamber, or supplied by a dedicated oven technology, which evaporates solid materials. The generated plasma is confined by a magnetic field, which is a superposition of a sextupole field and a magnetic mirror field of two Helmholtz coils. The electrons in the plasma are thus trapped longitudinal by the mirror field and transversely by the magnetic sextupole field forcing the electrons on a circular orbit with an angular frequency of $\omega = \frac{qeB_{\text{ECRIS}}}{m}$. This formula can be simplified for electrons in terms of the operating frequency

$$f = B_{\text{ECRIS}} \cdot 28\,\text{GHz/T}. \tag{2.2}$$

The GSI ECRIS thus works with a $B_{\text{ECRIS}} = 0.5\,\text{T}$ field, whereas the maximum magnetic field from the Helmholtz coils is operated at approx. 1 T. Through the applied RF field of the same frequency, the electrons in the emerging plasma are excited at this resonance frequency. The resonance between the electrons and the radiation excites the electrons energetically, increasing the effect of electron impact ionization and therefore producing more free electrons, which again produce more ions. Finally, the ions are extracted by an electrostatic focusing system, consisting of multiple electrodes, which are negatively charged in total
An ECRIS can deliver singly and multiply charged ions, depending on the (path) length of the confinement in the chamber, and is well suited for CW operation [62].

2.2. Radio-Frequency Quadrupoles

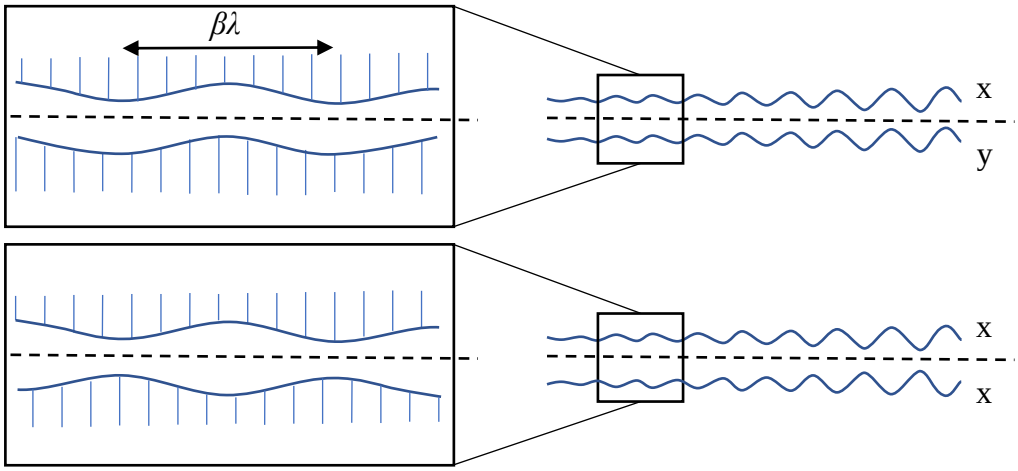

Figure 2.1: Sinusoidal milling in an RFQ for both coupling planes (x-x and x-y). (image source: [66], edited)

For modern ion accelerators, the **R**adio **F**requency **Q**uadrupole (RFQ) provides for beam acceleration at very low beam energy so that a conventional drift-tube linac section is able to accept the beam. The idea of the RFQ accelerator was developed by I.M. Kapchinskiy and V.V. Vladimirsky in 1970 [67] and is widely applied since the 1980s in various accelerator facilities worldwide [68]. Their main purpose is to pre-accelerate the beam in a regime of $\beta = 0.01$ to 0.08 and to form individual ion bunches from a continuous beam longitudinally, while separately focusing the beam in transverse direction. This is achieved with an advanced geometry of the electrodes forming the RF quadrupole, i.e., sinusoidal milling along four vanes or rods in longitudinal direction (see Figure 2.1), which provides simultaneous periodic transverse focusing forces and the initial longitudinal formation (Gentle Bunching) of a bunch, followed by the main acceleration part, while maintaining the 3D focusing.
The sinusoidal geometry along a cell length L_{cell} provides an electric field geometry as follows [69]:

$$E_x = -\frac{XV_0}{a^2} x \frac{kAV_0}{2} I_1(kr) \frac{x}{r} \cos(kz) \sin(\omega t + \phi) \tag{2.3}$$

$$E_y = \frac{XV_0}{a^2} y \frac{kAV_0}{2} I_1(kr) \frac{y}{r} \cos(kz) \sin(\omega t + \phi) \tag{2.4}$$

$$E_z = \frac{kAV_0}{2} I_0(kr) \sin(kz) \sin(\omega t + \phi), \tag{2.5}$$

with the terms $k = 2\pi/L_{\text{cell}}$, the electric potential V_0, minimum aperture radius a, modulation m and maximum aperture radius ma, as well as the radius $r(x, y) =$

$\sqrt{x^2+y^2}$ and modified Bessel function $I_n(x)$. The time dependence is based on the angular RF frequency ω and the RF phase shift ϕ. Furthermore, the dimensionless quantities based on the geometric terms a and ma are the focusing efficiency X and the acceleration efficiency A, are expressed as

$$X = \frac{I_0(ka) + I_0(kma)}{m^2 I_0(ka) + I_0(kma)} \tag{2.6}$$

and

$$A = \frac{m^2 - 1}{m^2 I_0(ka) + I_0(kma)}. \tag{2.7}$$

Those field equations can be used for RFQ design in combination with iterative solving of the equations of motion (see Section 3.6), whilst the magnetic field in the aperture is negligible.
Thus, the invention of RFQs is a significant milestone for ion accelerator technologies, as it allows in particular for space charge dominated heavy ion beam transport and acceleration of the beam.

2.3. H-Mode Cavities

There are two major implementations of Magnetic Mode (H-mode)[1] resonators: **I**nterdigital **H**-mode (IH) and **C**rossbar **H**-mode (CH) cavities. IH resonators are based on the magnetic pillbox mode[2] $H_{1,1,1}$, which has been proposed by R. Wideröe in 1928 [70] and was realized for the first time in 1956 [71].
Due to the demanding engineering issues of the H-mode cavities, being too compact at higher resonance frequency or reaching only low frequencies with low reference particle velocities, they were rarely adopted until the 1980s. In the following years, the challenges were mitigated by improved analytical design approaches and increased computational power.
H-mode cavities are attractive alternatives to Alvarez resonators, as the shunt impedance of cavities is significantly higher, enabling also higher beam acceleration gradients at the same RF power. For the H-mode of an empty pillbox cavity, the dominant electric field oscillates between two points on the shell for a H-mode, whereas for the **E**lectric Mode (E-mode)[3] the electric field is present between the two caps of the pillbox.
The electromagnetic field of the pillbox modes could be described by their mode indices m n p, the Bessel function J_m and its derivative J'_m with their respective roots x_{mn} and x'_{mn}. Furthermore, using the scalars $k_{mn} = x_{mn}/R$, cylinder radius R, angular frequency ω, time t and the imaginary unit i, the E-mode and H-mode can be detailed as follows.

[1] or **T**ransverse **E**lectric Mode (TE-mode)
[2] The indices define the number of junctions of the E/H field there are in ϕ, r and z direction.
[3] or **T**ransverse **M**agnetic Mode (TM-mode)

Magnetic Mode (H-mode) [69]

$$B_z = B_0 J_m(k_{mn} r)\cos(m\Theta)\sin(p\pi z/l)e^{i\omega t} \tag{2.8}$$

$$B_r = \frac{p\pi}{l}\frac{a}{x'_{mn}} B_0 J'_m(k_{mn} r)\cos(m\Theta)\cos(p\pi z/l)e^{i\omega t} \tag{2.9}$$

$$B_\Theta = -\frac{p\pi}{l}\frac{ma^2}{x'^2_{mn} r} B_0 J_m(k_{mn} r)\sin(m\Theta)\cos(p\pi z/l)e^{i\omega t} \tag{2.10}$$

$$E_z = 0 \tag{2.11}$$

$$E_r = i\omega\frac{ma^2}{x'^2_{mn} r} B_0 J_m(k_{mn} r)\sin(m\Theta)\sin(p\pi z/l)e^{i\omega t} \tag{2.12}$$

$$E_\Theta = i\omega\frac{a}{x'_{mn}} B_0 J'_m(k_{mn} r)\cos(m\Theta)\sin(p\pi z/l)e^{i\omega t} \tag{2.13}$$

Electric Mode (E-mode) [69]

$$E_z(r,\theta,z) = E_0 J_m(k_{mn} r)\cos(m\Theta)\cos(p\pi z/l)e^{i\omega t} \tag{2.14}$$

$$E_r(r,\theta,z) = -\frac{p\pi}{l}\frac{R}{x_{mn}} E_0 J'_m(k_{mn} r)\cos(m\Theta)\sin(p\pi z/l)e^{i\omega t} \tag{2.15}$$

$$E_\Theta(r,\theta,z) = -\frac{p\pi}{l}\frac{mR^2}{x^2_{mn} r} E_0 J_m(k_{mn} r)\sin(m\Theta)\sin(p\pi z/l)e^{i\omega t} \tag{2.16}$$

$$B_z(r,\theta,z) = 0 \tag{2.17}$$

$$B_r(r,\theta,z) = -i\omega\frac{mR^2}{x^2_{mn} r c^2} E_0 J_m(k_{mn} r)\sin(m\Theta)\cos(p\pi z/l)e^{i\omega t} \tag{2.18}$$

$$B_\Theta(r,\theta,z) = -i\omega\frac{R}{x_{mn} c^2} E_0 J'_m(k_{mn} r)\cos(m\Theta)\cos(p\pi z/l)e^{i\omega t} \tag{2.19}$$

The H-mode field configuration does not have any longitudinal electric field component, which is essential for particle acceleration (see Figure 2.2). By inserting drift-tubes, which are connected to the inner shell, where the maxima of the electric field are located, a field in longitudinal direction is obtained for H-mode cavities as well. This is realized by alternately mounting the drift-tubes on opposite sides, which charges them alternately (this insertion is called *Interdigital*, see Figure 2.3). Due to the oppositely charged tubes, an electric field in the longitudinal direction is generated.

As the electric field is most dominant along the beam axis due to the geometry, the shunt impedance is improved compared to that of typical TM-mode cavities (e.g., Alvarez, see Figure 2.2), whose fields, in contrast, oscillate between the two end caps and thus fill the entire volume instead of being concentrated at the beam axis. Since the electric field therein has no longitudinal junctions inside the resonator, the expression $H_{1,1,(0)}$ or $H_{1,1}$-mode is also used [72].

For CH resonators, the same principle is applied. This cavity type is operated in a higher mode, the $H_{2,1}$-mode. There are four instead of two electric poles on the

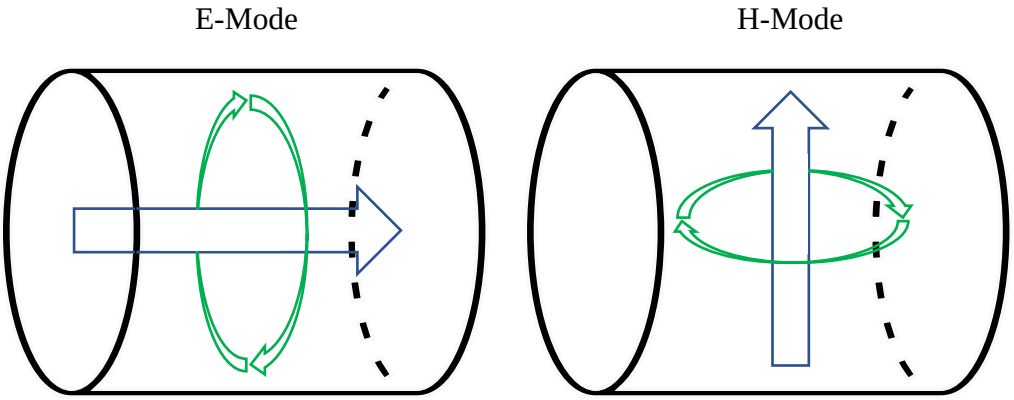

Figure 2.2: Basic resonance modes in a pillbox; the electric field (*blue*) oscillates either between the end caps (*left*) or between the shell (*right*). The magnetic field (*green*) surrounds the electric field circularly, according to Maxwell's equations.

shell, which allows the stems to be placed in a crossed pattern [69]. Those structures offer also a high shunt impedance and are therefore an attractive alternative to usual Alvarez-type accelerators, also because CH cavities can operate at higher beam energies (see Table 2.1).

Table 2.1: Structure types for low β beam acceleration [73, 74]

Type	Usual β	Frequency f (MHz)	Effective Shunt Impedance Z_0 (MΩ/m)	Eigenmode
RFQ	0.002–0.08	≤ 800		TE_{110}/TE_{210}
IH Cavity	0.01–0.25	30–250	300–150	TE_{110}
CH Cavity	0.05–0.5	150–800	150–80	TE_{210}
Alvarez	0.05–0.35	100–500	25–50	TM_{010}

For the specific implementation of an H-mode cavity, the shunt impedance can be estimated using following formula [74]

$$Z_0 = \frac{\mu_0^{3/2}\kappa^{1/2}R^3(\phi/2)^2\omega^{7/2}}{\sqrt{2}\pi^2c^2N_m(\phi/2+2c_1)c_2\bar{\beta}^2}, \tag{2.20}$$

with the electric conductivity κ, inner tank radius R, angular frequency ω, speed of light c, vacuum permeability μ_0, symmetry factor N_m (2 for IH, 4 for CH), effective current path length c_1 (usually 1 to 1.2), loss coefficient c_2 (usually 1.3 to 2) and $\bar{\beta}$, the mean beam velocity in the tank as fraction of speed of light. Furthermore, the

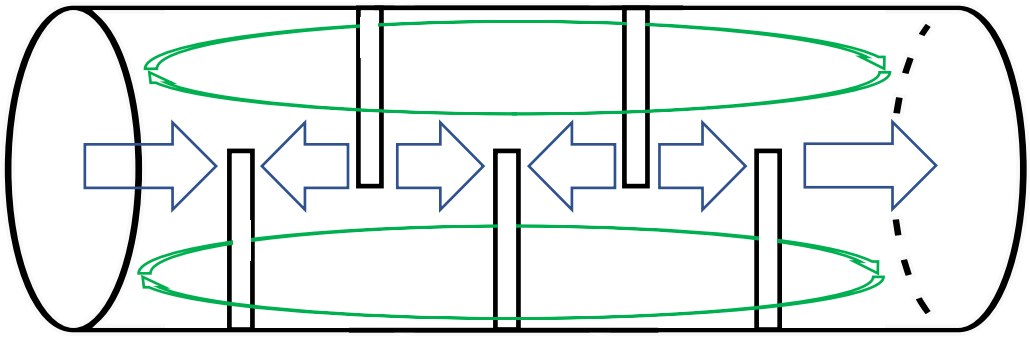

Figure 2.3: Working principle of IH cavities; the magnetic field lines (*green*) are oriented in longitudinal direction, as in a pillbox $H_{1,1,1}$, near the axis the electric field lines (*blue*) point in longitudinal direction as well, due to the insertion of stems.

stems-free angle ϕ in transverse cross-section of the tank is used (if no stems are used, this value amounts to 360°).
The voltage U in each gap n can be estimated by the following formula [72]

$$U_n = U_{\max} \sin\left(\pi \frac{2n-1}{2N}\right). \tag{2.21}$$

However, this is only a rough estimate, as the shape of the girders, which are used to flatten the electric field distribution in the gaps, and any internal magnetic lenses, as well as the capacitance load due to the tube-gap-tube geometry, significantly influence the electric field distribution [74].

Whereas Alvarez-type cavities can be built with internal quadrupole lenses inside the drift-tubes for continuous beam focusing during the acceleration process; inside H-mode cavities different transverse beam focusing schemes could be utilized, as their compact layout impedes the systematic usage of internal coils in each tube. Different methods for transverse focusing have been applied as the employment of quadrupole lenses within dedicated, longer enclosures (different from the standard drift-tube geometry), compact **P**ermanent **M**agnet **Q**uadrupole (PMQ) or APF. The above focusing schemes could also be integrated into Alvarez structures.
The internal quadrupole lenses are usually much bulkier compared to the standard drift-tube length (according to the actual $\beta\lambda$ cell length) and need a dedicated region to be mounted, which interrupts the resonance acceleration pattern and therefore reduces the effective acceleration gradient. The thereby created additional longitudinal drift through the quadrupole requires additional bunching sections,

providing sufficient longitudinal beam focusing.
Permanent magnet quadrupole focusing within H-mode cavities overcomes this problem by inserting the PMQs within the standard drift-tubes and allows stable beam. However, due to the lower adaptability during operation for different ion species, it has found minor application in facilities with a high variation of mass-to-charge ratio from proton to uranium.
Last, but not least, APF can be applied for transverse and longitudinal beam focusing using electric RF fields only (see Section 3.5). APF is an advanced option, as it simplifies the RF engineering and enables eased operation with different mass-to-charge ratios. Beneficially, the phase and amplitude of the cavity must be controlled without additional focusing magnets. Avoiding magnetic lenses also allows the application of the APF focusing scheme within SC RF accelerators.

2.4. Half and Quarter Wave Cavities

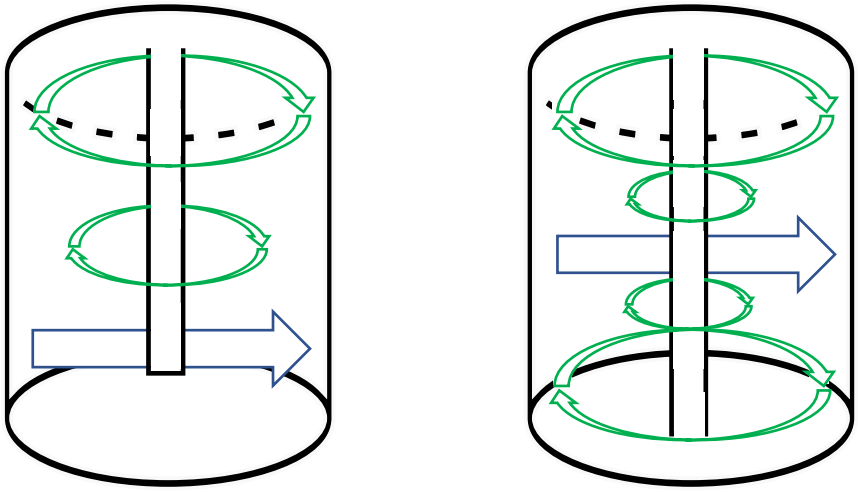

Figure 2.4: Quarter wave resonator (*left*) and half-wave resonator (*right*). Both electric (*blue*) and magnetic (*green*) field components oscillate in longitudinal direction.

Due to their high ohmic losses, occurring from the long current path from the center tube at the stem to the fringe-tube on the shell, **H**alf **W**ave **R**esonators (HWRs) and **Q**uarter **W**ave **R**esonators (QWRs) are rather suited for SC applications. But due to their longitudinal compactness, they are applied at GSI as short rebuncher cavities. HWR/QWR are line resonators with a capacitively heavily loaded end. The stems provide the inductance of the resonator and the acceleration gaps between the stem and the shell provide the main capacity, inducing an electric field on the beam axis. If the stem is connected only to one cap, the magnetic field's amplitude along the height is described by a quarter oscillation (see Figure 2.4), so its height corresponds to

$h = \lambda/4$. If both caps are connected to the stem, the magnetic amplitude is described by a half oscillation, i.e., a half-wave: $h = \lambda/2$. HWRs are suitable for higher β operation. The asymmetric geometry furthermore tends to steer the beam. QWRs, compared to HWRs, are easier to access for maintenance and are twice more effective in terms of power consumption. Both cavity types provide only a few RF gaps, which increases the total accelerator length by adding intertank sections in between the cavities. Beneficially, the separate phase and voltage controls of each resonator ensure very flexible and reliable linac operation.
Due to the low number of gaps in QWR/HWR cavities, the transit time factor T_{TTF} of those (usually two gap) cavities allows for acceptance of very different velocity values β apart from their design velocity β_0. This is expressed by means of a synchronism factor (see Equation (3.48) on page 33).

2.5. Normal Conducting and Superconducting Cavities

The development of **S**uper**C**onducting (SC) RF technologies allows advanced application of SC accelerators. State-of-the-art SC cavities as QWR/HWR cavities, as well as CH cavities, are successfully applied for heavy ion acceleration [43, 75]. There are three basic design criteria determining the potential application of SC cavities (see Table 2.2).

Table 2.2: Design criteria for normal and superconducting accelerators [76].

	Normal-conducting	Superconducting
Beam energy	low	high
Beam power	high	low
Duty cycle	low	high

The small resonance length ($\propto \beta\lambda$) within low beam energy regions impedes the design of SC cavities. High beam power and thus possible beam losses make SC operation sensitive to disturbances, as the heating induced by beam losses leads to breakdowns of superconductivity (quenches) and render the cavities useless until they are cooled again. As the cavities are constantly cooled by a cryogenic system and RF losses play an insignificant role, it is economic to apply them for **C**ontinuous **W**ave (CW) operation, since in SC accelerators by far the largest part of the required primary power is needed for the cryogenic system operation. The **N**ormal **C**onducting (NC) accelerators are limited with the primary power consumption per meter. The RF power required for beam acceleration is for SC and NC-cavities identically, determined only by the beam current. However, if the beam load is high enough, it can undermine the economic advantages of superconducting application and allow for an NC layout. Overall, the advantages and drawbacks of normal- and superconducting operation must be weighed against each other to ensure a reasonable choice [75–77].

2.6. Continuous Wave Operation

As mentioned in the previous section, operation in **C**ontinuous **W**ave (CW) mode imposes constraints on the design of **N**ormal **C**onducting (NC) and SC cavities. NC cavities are limited in their field gradient by power dissipation as excessive heat, since the cavity must be continuously powered. The magnetic field $\vec{H}$ inside the resonator induces currents on the cavity surface, which results in heat and therefore dissipated power P_c [78]

$$P_c = \frac{1}{2} R_s \oint_A |\vec{H}|^2 \, d\vec{A}, \tag{2.22}$$

with the electric surface resistance R_s, which depends on the conductivity σ, the magnetic permeability μ and the RF frequency f for the NC case [78]

$$R_{s,NC} = \sqrt{\frac{\pi \mu f}{\sigma}}. \tag{2.23}$$

For SC cavities R_s depends on the density of NC electrons n_n, elementary charge e, mean free path l, electron mass m_e, Fermi velocity v_F, temperature T, Boltzmann constant k_B, vacuum permeability μ_0, current layer thickness λ_L and angular frequency ω [78]

$$R_{s,SC} = \mu_0^2 \lambda_L^3 \omega^2 \frac{n_n e^2 l}{m_e v_F} e^{-\frac{\Delta T}{k_b T}}. \tag{2.24}$$

Furthermore, the Kilpatrick limit, a criterion for vacuum sparking designed to include RF and direct current [69, 79] has to be considered for this type of application, since CW operation is particularly sensitive to the Kilpatrick limit; it is defined by

$$f(E) = 1.64\,\mathrm{MHz} \frac{E^2}{E_0^2} e^{-8.8 E_0/E} \text{ , using } E_0 = 1\,\mathrm{MV/m}. \tag{2.25}$$

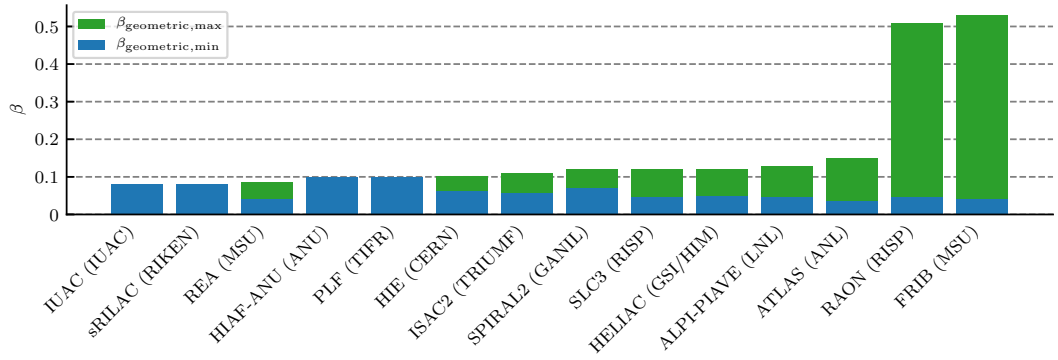

Figure 2.5: Velocity region for different SC accelerator facilities with CW application [75] as fraction of speed of light β.

Due to these restrictions, most CW linacs are designed with superconducting cavities starting at intermediate beam energies of 1 MeV/u to 2 MeV/u (see Figure 2.5). Superconducting cavities are usually limited by the peak surface fields due to superconducting breakdown limits rather than sparking, quenches and field emission, as described by Kilpatrick. Therefore, CW linacs are best suited to deliver high average beam at low peak current.

3. Beam Dynamics

The layout of each particle accelerator bases on proper beam dynamics studies, as well as the solution of numerous design questions and the support of the commissioning process. The design and commissioning of an accelerator cannot be conducted without considering the beam dynamics. The basics of beam dynamics, relevant for the description of linacs and their subsystems, are summarized in the following. The description is strongly related to Maxwell's equations, which are stated (in differential form) as follows:

$$\operatorname{div} \vec{E} = \frac{\rho}{\epsilon_0} \tag{3.1}$$

$$\operatorname{div} \vec{B} = 0 \tag{3.2}$$

$$\operatorname{rot} \vec{E} = -\frac{d\vec{B}}{dt} \tag{3.3}$$

$$\operatorname{rot} \vec{B} = \mu_0 \vec{j} + \mu_o \epsilon_0 \frac{d\vec{E}}{dt}, \tag{3.4}$$

using the electric field $\vec{E}$, the magnetic field $\vec{B}$, the charge density ρ, the current density $\vec{j}$, the vacuum permittivity ϵ_0 and the vacuum permeability μ_0.
Equation (3.1) can be rewritten for free space (in Cartesian coordinates) as follows:

$$\frac{dE}{dx} + \frac{dE}{dy} + \frac{dE}{dz} = 0. \tag{3.5}$$

In this case, a focusing gradient in all directions at the same time is not feasible. Therefore, sophisticated focusing approaches in combination with magnetic fields are used to achieve beam focusing and acceleration.

3.1. Conventions

In the following, the used standard beam dynamics conventions are described. Hence, we define β as the velocity as a fraction of speed of light c_0

$$\beta = \frac{v}{c_0}. \tag{3.6}$$

Thus the relativistic Lorentz factor, relevant for time dilatation, length contraction and relativistic mass is expressed as

$$\gamma = \frac{1}{\sqrt{1-\beta^2}}. \tag{3.7}$$

Another useful and frequently used quantity is the resonance length $\beta\lambda$, which describes how far a particle travels within an RF period T_0 [80]:

$$vT_0 = \beta c_0 T_0 = \frac{\beta c_0}{f_0} = \beta\lambda. \tag{3.8}$$

From this definition, the two standard DTL classes are distinguished, the $\beta\lambda$ and $\beta\lambda/2$ cavities (see Section 2.3). The length between two adjacent RF gap-centers is derived from the resonance length patterns and is thus a fundamental geometric parameter for the design of the drift-tubes in different regimes of particle velocity.

Particle ensemble

A general approach for the description of a particle bunch is to consider the position and velocity of each particle. In order to reduce the number of particles to be described, so-called macro-particles are introduced, carrying n particles, which reduces the memory load for calculations, since calculations with the actual number of particles (usually above trillions of particles) are impractical. Thus, macro-particle coordinates in the 6D-phase space can be expressed by the vector $\vec{x}$

$$\vec{x} = \begin{pmatrix} x \\ v_\mathrm{x} \\ y \\ v_\mathrm{y} \\ z \\ v_\mathrm{z} \\ n \end{pmatrix} \tag{3.9}$$

and a bunch ensemble X in phase space is thus expressed as a set of vectors

$$X = \{\vec{x}_0, \vec{x}_1, .., \vec{x}_n\}. \tag{3.10}$$

By defining a center particle $\vec{x}_0$ and a reference frequency f_0, the longitudinal distance to the reference particle with respect to RF phase is specified as [80]

$$\Delta\phi = -\frac{z - z_0}{\beta_0\lambda} 360^\circ, \tag{3.11}$$

as well as its momentum spread [80]

$$\frac{\Delta p}{p} = \frac{\beta\gamma}{\beta_0\gamma_0}, \tag{3.12}$$

which relates to the energy spread by [80]

$$\frac{\Delta W}{W} = \frac{(\gamma_0 + 1)}{\gamma_0}\frac{\Delta p}{p}. \tag{3.13}$$

Equation (3.13) can be simplified for low velocities ($\gamma \approx 1$) as $\frac{\Delta W}{W} \approx 2\frac{\Delta p}{p}$. The transverse momentum spread is usually given by Equation (3.12) as $p_{x,y}/p_z$ in units of mrad [81]. The choice of the mean particle is usually made either by selecting the center of gravity, a method valid for measured data, or by virtually specifying a reference particle in the input distribution which is feasible in beam dynamics calculations.

Relativity

The already introduced relativistic Equation (3.6) and (3.7) are part of the Lorentz transformation [80], which transforms a coordinate system with constant velocity (indicated with $\hat{}$) into a resting reference frame by stretching the spacetime.

$$\begin{pmatrix} x \\ y \\ z \\ ct \end{pmatrix} = \begin{pmatrix} 1 & 0 & 0 & 0 \\ 0 & 1 & 0 & 0 \\ 0 & 0 & \gamma & -\beta\gamma \\ 0 & 0 & -\beta\gamma & \gamma \end{pmatrix} \cdot \begin{pmatrix} \hat{x} \\ \hat{y} \\ \hat{z} \\ c\hat{t} \end{pmatrix} \tag{3.14}$$

As a result, the interval lengths in space and time differ by the observing system, which is described by the Lorentz contraction

$$\Delta z = \gamma \Delta \hat{z} \tag{3.15}$$

and by time dilatation

$$\Delta t = \gamma \Delta \hat{t}. \tag{3.16}$$

Furthermore, the well-known equivalence of mass and energy is stated as

$$E_{\text{rest}} = m_0 c_0^2, \tag{3.17}$$

which connects the rest mass to its potential energy. With known velocity β, the kinetic energy is

$$W_{\text{kin}} = (\gamma - 1) m_0 c_0^2. \tag{3.18}$$

By using the relativistic momentum

$$p = \gamma m_0 c_0, \tag{3.19}$$

Equation (3.17) can be rewritten in terms of p:

$$E^2 = (pc_0)^2 + (m_0 c_0^2)^2. \tag{3.20}$$

General Theory of Courant and Snyder

The beam transport in accelerators is mainly determined by the interaction of the particles with electromagnetic fields. Thus, the particle transport can be described in general terms by the Lorentz force

$$\vec{F} = q(\vec{E} + \vec{v} \times \vec{B}) \tag{3.21}$$

in combination with relativistic acceleration [63]

$$\vec{a} = \frac{1}{\gamma m}\left(F - \frac{(\vec{F}\vec{v})\vec{v}}{c^2}\right). \tag{3.22}$$

The electromagnetic fields of RF cavities and magnetic lenses are used to focus the beam transversely and longitudinally, to obtain a compact bunch ensemble.
For the description of the beam transport sections the Courant and Snyder parameters, i.e., Twiss parameters, are commonly applied [82]. The general theory of Courant and Snyder has been published in 1958 and lead to the application of alternating gradient focusing, which increased the effectiveness of magnetic beam focusing. For this theory the Hill equation, describing an oscillator along the path s with variable spring constant $K(s)$ constrained to be periodic $K(s) = K(s + L)$, is solved

$$x''(s) + K(s)\, x(s) = 0. \tag{3.23}$$

The above ordinary differential equation is solved with the approach

$$x(s) = \sqrt{\hat{\beta}(s)\epsilon}\sin(\Phi(s)), \tag{3.24}$$

where $\sqrt{\hat{\beta}(s)\epsilon}$ is the maximum amplitude of oscillation along the path and $\sin(\Phi(s))$ determines the actual amplitude of oscillation. By substituting $(x(s))^2$ in the expression of the derivative $(x'(s))^2$ and the choice of $\hat{\alpha}(s) = -\frac{1}{2}\hat{\beta}'(s)$ and $\hat{\gamma}(s) = \frac{1+\hat{\alpha}(s)^2}{\hat{\beta}(s)}$ it can be shown that the particle motion in phase space x and x' is constrained along an ellipse

$$\hat{\gamma}(s)x^2 + 2\hat{\alpha}(s)xx' + \hat{\beta}(s)x'^2 = \hat{\epsilon}, \tag{3.25}$$

where $\hat{\alpha}$, $\hat{\beta}$ and $\hat{\gamma}$ are the Twiss parameters, with the corresponding emittance $\hat{\epsilon}$. The typical unit of $[\hat{\epsilon}] = \text{mm mrad}$, $[\hat{\alpha}] = 1$, $[\hat{\beta}] = \text{m}$, $[\hat{\gamma}] = 1/\text{m}$, $[x] = \text{mm}$ and of $[x'] = \text{mrad}$. The emittance scales the size of the ellipse surface, thus the area A is given by $A = \pi\hat{\epsilon}$. The variable $\hat{\beta}$ scales the square of the ellipse width $x_{\max} = \sqrt{\hat{\beta}\hat{\epsilon}}$ and $\hat{\alpha}$ governs the ellipse inclination (see Figure 3.1). Therefore, $\hat{\gamma}$ is constrained

$$\hat{\beta}\hat{\gamma} - \hat{\alpha}^2 = 1. \tag{3.26}$$

For this reason γ is usually not mentioned when the Twiss parameters are specified. Thus, a particle stays on its ellipsoidal trajectory in phase space and moves on its equipotential line corresponding to the phase advance Φ

$$\Phi(s) = \int \frac{ds}{\hat{\beta}(s)}. \tag{3.27}$$

The particle trajectory is defined by its initial state

$$x = x_0 a + x_0' b \tag{3.28}$$

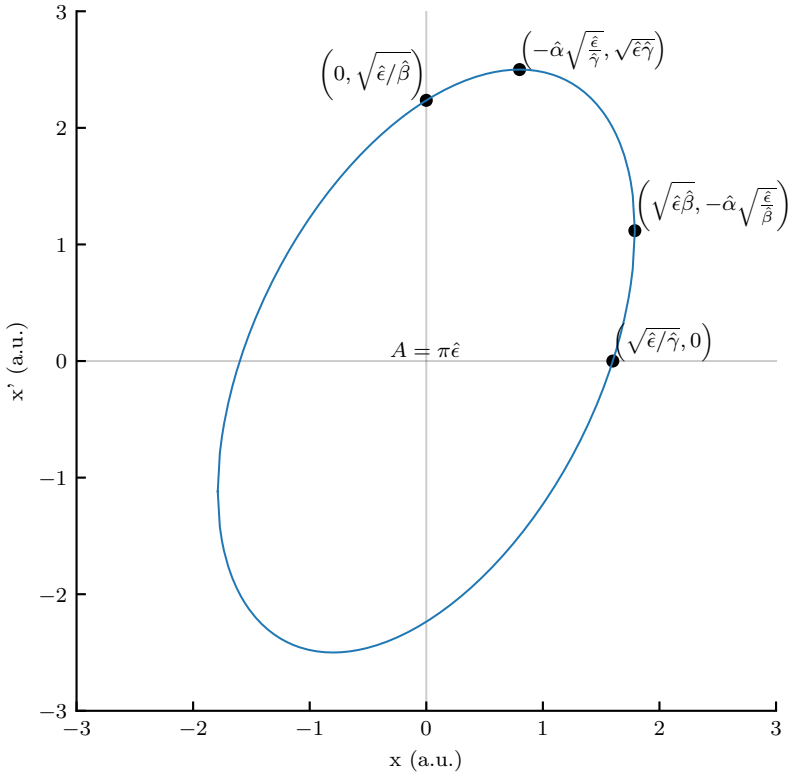

Figure 3.1: Example ellipse ($\hat{\alpha} = -0.5$, $\hat{\beta} = 0.8$, $\hat{\epsilon} = 4$) and extrema/intersections using Twiss parameters.

$$x' = x_0 c + x'_0 d, \tag{3.29}$$

which is represented in matrix form as

$$\begin{pmatrix} x \\ x' \end{pmatrix} = \begin{pmatrix} a & b \\ c & d \end{pmatrix} \cdot \begin{pmatrix} x_0 \\ x'_0 \end{pmatrix}. \tag{3.30}$$

This equation can be rewritten in terms of Twiss parameters as [81]

$$\begin{pmatrix} \hat{\beta} \\ \hat{\alpha} \\ \hat{\gamma} \end{pmatrix} = \begin{pmatrix} a^2 & -2ab & b^2 \\ -ac & ad + bc & -bd \\ c^2 & -2cd & d^2 \end{pmatrix} \cdot \begin{pmatrix} \hat{\beta}_0 \\ \hat{\alpha}_0 \\ \hat{\gamma}_0 \end{pmatrix} \tag{3.31}$$

By solving for the Eigenvectors of this system, called *matched* Twiss parameters, one finds the Eigenvalues and thus the Twiss parameters of the ellipse that satisfy the periodicity condition $\hat{\beta}(s) = \hat{\beta}(s + l)$

$$\begin{pmatrix} x \\ x' \end{pmatrix} = \begin{pmatrix} \cos(\Phi) + \hat{\alpha}\sin(\Phi) & \hat{\beta}\sin(\Phi) \\ -\hat{\gamma}\sin(\Phi) & \cos(\Phi) - \hat{\alpha}\sin(\Phi) \end{pmatrix} \cdot \begin{pmatrix} x_0 \\ x'_0 \end{pmatrix}, \tag{3.32}$$

necessary for the general analysis of periodic channels.
For special reference systems of the phase space, the emittance appears to be shrinking with increased momentum. For example, the transverse phase space in units of mm and mrad implies this effect, because this value is derived from dividing the transverse by the increasing longitudinal velocity: $p_x/p_{0,z}$. In order to compensate this effect and make eventual emittance growth visible, the emittance can be scaled up by the velocity dependent part with the relativistic terms β and γ and is called the normalized emittance $\hat{\epsilon}_n$:

$$\hat{\epsilon}_n = \hat{\epsilon}\beta\gamma \tag{3.33}$$

Root Mean Squared & Effective Twiss Parameters

The **R**oot **M**ean **S**quared (RMS) Twiss parameters are a theoretical approach to compare different particle distribution types and translate them into one another by means of an *equivalent beam*, preserving their energy, ion species and RMS emittance [83, 84], that can be useful to combine theoretical models and actual measurements. The RMS Twiss parameters can be derived for any kind of 2D particle distribution using its average (denoted by $\langle\ \rangle$) positions u and velocities v.

$$\hat{\epsilon}_{\mathrm{RMS}} = \sqrt{\langle u^2\rangle\langle v^2\rangle - \langle uv\rangle^2} \tag{3.34}$$

$$\hat{\beta}_{\mathrm{RMS}} = \frac{\langle u^2\rangle}{\epsilon_{\mathrm{RMS}}} \tag{3.35}$$

$$\hat{\alpha}_{\mathrm{RMS}} = \frac{\langle uv\rangle}{\epsilon_{\mathrm{RMS}}} \tag{3.36}$$

The equations above are a standard approach to calculate emittance growth (whereas the universal calculation of the total emittance[1] is more complex). The RMS beam size is in a fixed relation to the total emittance of theoretical distributions (see Table 3.1). However, for realistic distributions with complex contours, the relationship between RMS and total emittance is weak due to more complex enclosing borders.

Different Types of Artificial Particle Distributions

A variety of (artificial) distribution types can be used as a starting point for the analysis of beam dynamics in beam transport and acceleration systems. For multi-particle tracking simulations, it is to be noted that quantities such as emittance growth and particle loss may depend strongly on the chosen input distribution type. A **K**apchinskiy-**V**ladimirsky (KV) [85] distribution has as homogeneous density-distribution in each phase plane. Losses arising at the fringes may appear bigger compared to a Gaussian distribution of the same effective radius. The generation of such distributions can usually be accomplished by uniform population of an N-dimensional hypersphere. The KV distribution represents a uniformly filled ellipse in the 2D sub-planes, the Waterbag distribution is a 4D uniformly filled sphere. The

[1] The total emittance $\hat{\epsilon}_{100\,\%}$ is defined as the smallest ellipse that fits 100 % of all particles

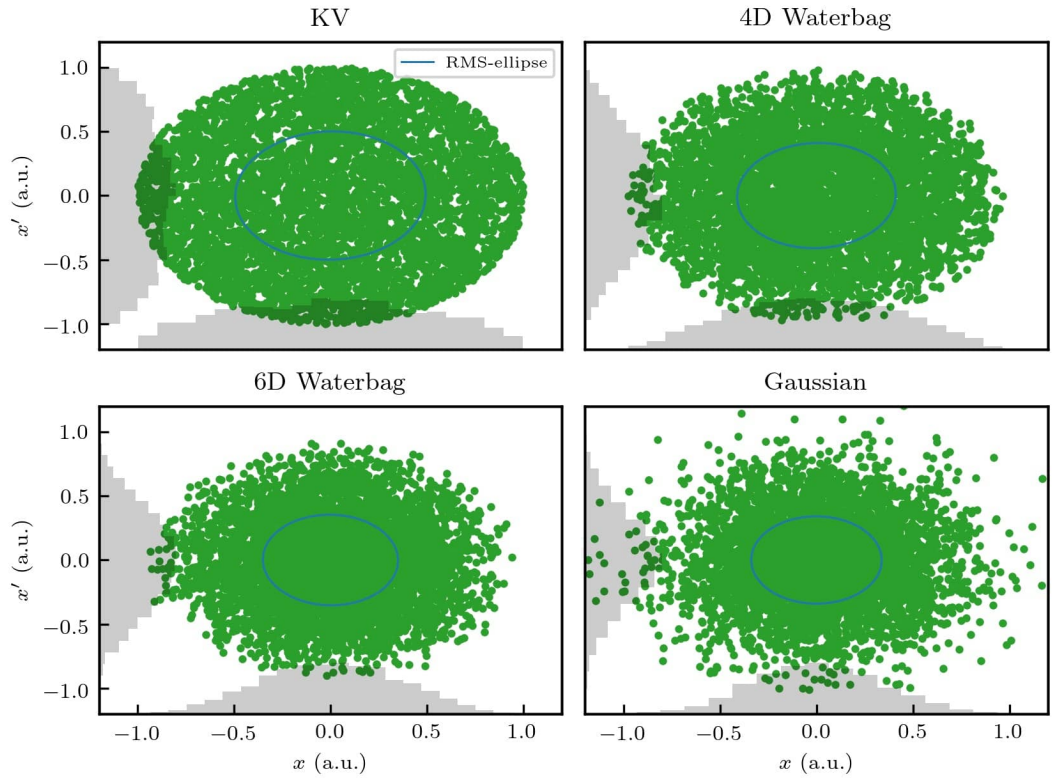

Figure 3.2: 2D cross-section of different particle distribution types.

parabolic (6D Waterbag) distribution can be derived from a 6 dimensional sphere (see Figure 3.2) [69].
Furthermore, the KV distribution [85] can be obtained in 4D phase space by populating the border of a 4D hypersphere with particles:

$$\frac{\hat{\gamma}_x x^2 + 2\hat{\alpha}_x x x' + \hat{\beta}_x x'^2}{\hat{\epsilon}_x} + \frac{\hat{\gamma}_y y^2 + 2\hat{\alpha}_y y y' + \hat{\beta}_y y'^2}{\hat{\epsilon}_y} = 1. \tag{3.37}$$

The 4D Waterbag distribution can be formalized with the following inequation:

$$\frac{\hat{\gamma}_x x^2 + 2\hat{\alpha}_x x x' + \hat{\beta}_x x'^2}{\hat{\epsilon}_x} + \frac{\hat{\gamma}_y y^2 + 2\hat{\alpha}_y y y' + \hat{\beta}_y y'^2}{\hat{\epsilon}_y} \leq 1, \tag{3.38}$$

or alternatively as 6-dimensional hollow hypersphere:

$$\frac{\hat{\gamma}_x x^2 + 2\hat{\alpha}_x x x' + \hat{\beta}_x x'^2}{\hat{\epsilon}_x} + \frac{\hat{\gamma}_y y^2 + 2\hat{\alpha}_y y y' + \hat{\beta}_y y'^2}{\hat{\epsilon}_y} + \frac{\hat{\gamma}_z z^2 + 2\hat{\alpha}_z z z' + \hat{\beta}_z z'^2}{\hat{\epsilon}_z} = 1. \tag{3.39}$$

The 6D Waterbag distribution can be formalized as uniformly filled 6D-hypersphere

with following inequation [86]:

$$\frac{\hat{\gamma}_x x^2 + 2\hat{\alpha}_x x x' + \hat{\beta}_x x'^2}{\hat{\epsilon}_x} + \frac{\hat{\gamma}_y y^2 + 2\hat{\alpha}_y y y' + \hat{\beta}_y y'^2}{\hat{\epsilon}_y} + \frac{\hat{\gamma}_z z^2 + 2\hat{\alpha}_z z z' + \hat{\beta}_z z'^2}{\hat{\epsilon}_z} \leq 1 \quad (3.40)$$

The relation of the above distribution types to their RMS and total emittance is depicted in Table 3.1, whereas the equations above are summarized in Table 3.2.

Table 3.1: Relation between total emittance $\hat{\epsilon}_{100\,\%}$ and RMS emittance $\hat{\epsilon}_{\mathrm{RMS}}$ for common particle distribution types [87].

Type	$\epsilon_{100\,\%}/\epsilon_{\mathrm{RMS}}$
KV	4
Waterbag	6
Parabolic (6D Waterbag)	8
Gaussian	∞
Truncated Gaussian[1]	$n\sigma$

[1]The maximum radius $n\sigma$ is a multiple of the standard deviation σ.

Table 3.2: Overview of operators $\diamond$ for the generation of multidimensional particle distributions using the equation $\sum_{\mathrm{axis}=1}^{\dim/2}(\hat{\gamma}_{\mathrm{axis}} u_{\mathrm{axis}}^2 + 2\hat{\alpha}_{\mathrm{axis}} u_{\mathrm{axis}} v_{\mathrm{axis}} + \hat{\beta}_{\mathrm{axis}} v_{\mathrm{axis}}^2)/\hat{\epsilon}_{\mathrm{axis}} \diamond 1$.

Distribution type	$\diamond$ 2D	$\diamond$ 4D	$\diamond$ 6D	$\diamond$ 8D
KV	$\leq$	$=$		
Waterbag		$\leq$	$=$	
Parabolic			$\leq$	$=$

A Gaussian distribution has an infinite radius in theory. In practice, with a finite count of particles, it has a random maximum radius, depending on the procedure of particle generation. To address this issue, the distribution could be truncated at a fixed radius, typically at 2σ or 3σ. However, with a low number of particles, the other distribution types also suffer from inaccuracy. The higher the dimension, the more particles are necessary to fill the N-dimensional ellipse adequately. A hypersphere with a high number of dimensions could have a too large volume to be filled entirely with a limited number of particles. The then partially filled sphere would not accurately reflect Table 3.1 (for example, if a KV distribution is generated with only 20 particles).

Liouville's Theorem

The Liouville theorem is a fundamental theorem of Hamiltonian mechanics and classical statistics [80]. It states that a N dimensional vector field given by the Hamilton operator $\dot{X} = (\frac{\delta H}{\delta p_i}, -\frac{\delta H}{\delta q_i})$ is free of divergence:

$$(\frac{1}{\delta q_i}, \frac{1}{\delta p_i}) \cdot \dot{X} = \sum_{i=1}^{N} (\frac{\delta H}{\delta q_i \delta p_i} - \frac{\delta H}{\delta p_i \delta q_i}) = 0. \tag{3.41}$$

Therefore, the volume enclosed by individual particle trajectories in phase space is constant. Thus, the emittance of a particle beam cannot be decreased by applying RF fields. Moreover, if an equipotential line is not completely filled with particles, the effectively populated surface can grow during evolution whilst retaining the actual surface area, as illustrated in Figure 3.3 [80].

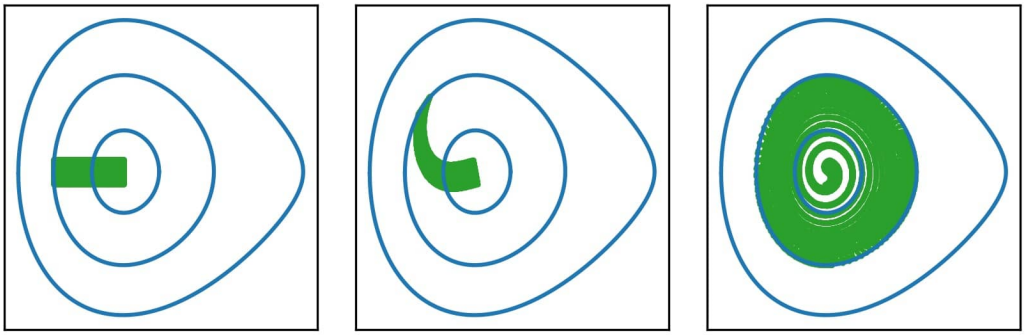

Figure 3.3: Time-evolution of a particle ensemble in the phase space, each particle remains on its closed trajectory; the different velocities effectively distort the initial particle distribution.

3.2. Radio Frequency Acceleration

Drift tubes within an RF resonator (see Figure 3.4) are commonly employed for RF acceleration of an ion bunch with low β (up to 0.5). Electric fields in the gaps between the tubes cause consecutive acceleration of the particle beam. Various RF structures are available for this purpose (see Section 2).
The to be accelerated ensemble of particles passes the RF gaps through its electric field $E(z, r)$ in space and time and obtains kinetic energy from the electric field. The energy gain ΔW depends on the particle charge q, the particle synchronous phase Φ and angular RF frequency ω [63]:

$$\Delta W = q \int_{l_1}^{l_2} E(z, r = 0) \cos(\omega t(z) + \Phi)\, dt. \tag{3.42}$$

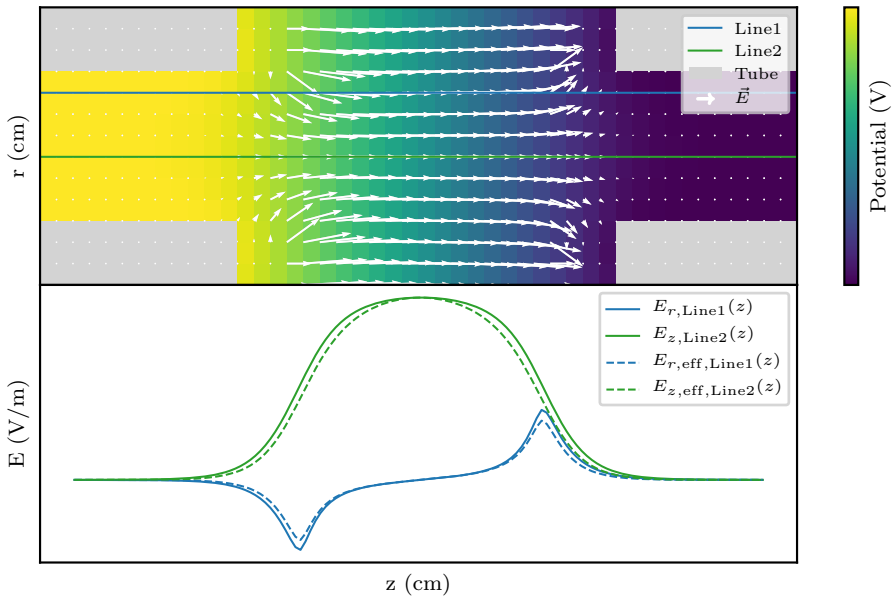

Figure 3.4: (*top*) Electric field distribution in an RF gap. (*bottom*) The longitudinal field component on the axis are marked in green, the off-axis, radial field component are marked in blue. The continuous lines indicate the maximum field, the dashed lines depict the effective field a particle with 0° synchronous phase travels through.

Equation (3.42) can be rewritten using the transit time factor T_{TTF} [63], which puts the maximum electric voltage $U_0 = E_0 L$ in relation to the effective voltage $U_{\mathrm{eff}} = U_0 T_{\mathrm{TTF}}$ to which the particle is exposed, as follows:

$$\Delta W = q E_0 T_{\mathrm{TTF}} L \cos(\Phi). \tag{3.43}$$

The field integral is shifted to the transit time factor T_{TTF}

$$T_{\mathrm{TTF}} = \frac{\int_{l_1}^{l_2} E(z, r=0) \cos(\omega t(z))\, dz}{\int_{l_1}^{l_2} E(z, r=0)\, dz}. \tag{3.44}$$

By assuming the electrical field as rectangular function inside the gap-length g, Equation (3.44) can be further simplified to

$$T_{\mathrm{TTF}} = \frac{\sin(\pi g/(\beta\lambda))}{\pi g/(\beta\lambda)}. \tag{3.45}$$

By assuming a volumetric RF gap field-geometry, the transit time factor T_{TTF} can be expressed in terms of the Bessel and modified Bessel function $I_0(x)$ and $J_0(x)$

$$T_{\mathrm{TTF}}(r) = I_0(Kr) \frac{J_0(2\pi a/\lambda)}{I_0(Ka)} \frac{\sin(\pi g/(\beta\lambda))}{\pi g/(\beta\lambda)}, \tag{3.46}$$

where a is the inner radius of the drift-tube and K relates to the resonance length $K = 2\pi/(\gamma\beta\lambda)$ [69].

Furthermore, the transit time factor can be expressed for several gaps, which decreases the beam energy acceptance of the gap-group, by introducing a synchronism factor T_S [88], altering the transit-time factor $T_{1\text{-gap}}$ and thus indicating the acceleration efficiency (see Figure 3.5)

$$T_{n\text{-gap}} = T_{1\text{-gap}}\, T_S(\beta, \beta_0, N). \tag{3.47}$$

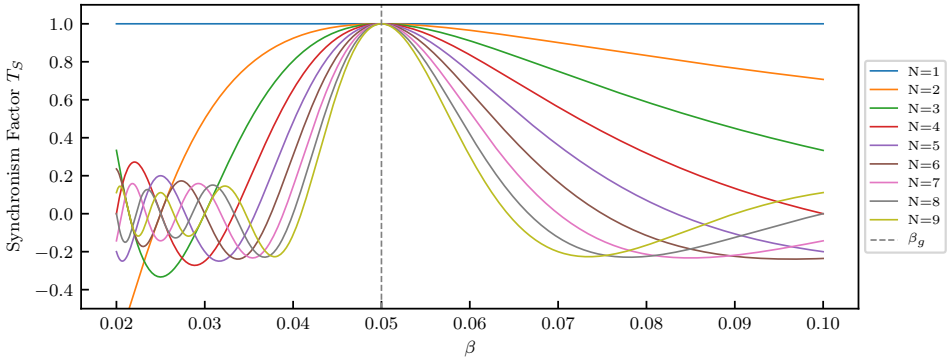

Figure 3.5: Synchronism factor T_s for geometric $\beta_0 = 0.05$ and different number of gaps N (see Equation (3.48) and (3.49))

The synchronism factor T_S therefore depends on the injected particle velocity β, the design velocity β_0 and the number of gaps N [88]

$$T_S(\beta, \beta_0, N) = \frac{(-1)^{(N-1)/2}\cos(N\pi\beta_0/(2\beta))}{N\cos(\pi\beta_0/(2\beta))}\text{, if } N \text{ is odd} \tag{3.48}$$

$$T_S(\beta, \beta_0, N) = \frac{(-1)^{N/2+1}\sin(N\pi\beta_0/(2\beta))}{N\cos(\pi\beta_0/(2\beta))}\text{, if } N \text{ is even.} \tag{3.49}$$

Furthermore, the beam focusing of an RF gap can be described by means of a linear transfer map M_u [63]. By assigning a central particle with phase Φ_{ref} and velocity v_{ref}, the particles in the vicinity are focused proportional to the sinus-function, the longitudinal and transverse focusing can be expressed by small-angle approximation as a matrix multiplication (see Equation (3.30)) in direction $u \in \{x, y, z\}$

$$M_u\vec{x}_u = \begin{pmatrix} 1 & 0 \\ k_u/(\beta\gamma)_f & (\beta\gamma)_i/(\beta\gamma)_f \end{pmatrix} \cdot \begin{pmatrix} u \\ v_u/v_{\text{ref}}. \end{pmatrix} \tag{3.50}$$

The transverse beam focusing depends on

$$k_{x,y} = \frac{-\pi q E_0 T_{\mathrm{TTF}} L \sin(\phi_{\mathrm{ref}})}{m_0 c^2 \beta^2 \gamma^2 \lambda} \tag{3.51}$$

and the longitudinal focusing is twice as strong:

$$k_z = \frac{2\pi q E_0 T_{\mathrm{TTF}} L \sin(\phi_{\mathrm{ref}})}{m_0 c^2 \beta^2 \lambda}. \tag{3.52}$$

This linear approximation can be used for standard beam dynamics calculations, whereas non-linear effects, which appear in beam dynamic concepts such as EQUUS, Combined Zero Degree Structure (**KO**mbinierte **NU**ll Grad **S**truktur, KONUS) or APF, are not considered [81].

Longitudinal Focusing

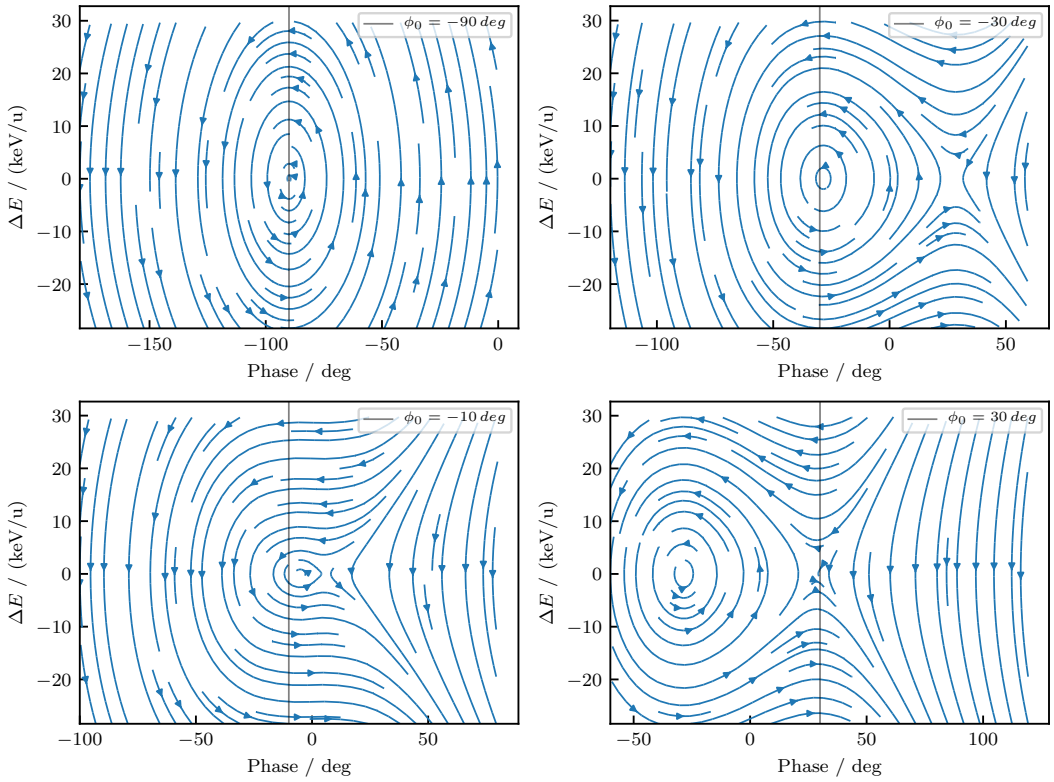

Figure 3.6: Particle motions in the longitudinal phase space for different reference synchronous phases: −90° (*upper left*), −30° (*upper right*), −10° (*lower left*), 30° (*lower right*)

In general, longitudinal focusing is caused by the RF field E_0 and is typically described by the shift of phase $\Delta\phi$ and energy ΔE. The acceleration of a particle depends on

the applied voltage $U_a cos(\phi)$. Comparing the acceleration voltage at a phase ϕ with the acceleration of a reference particle with synchronous phase ϕ_s, the energy shift with respect to the reference particle can be derived from Equation (3.43) [69]:

$$\Delta W_{\text{kin}} = qE_0 T_{\text{TTF}} L(cos(\phi) - cos(\phi_s)). \tag{3.53}$$

The relative phase shift $\Delta\phi$ indicates the longitudinal phase shift according to the reference particle

$$\Delta\phi = -2\pi N \frac{\Delta E}{mc^2\gamma^3\beta_0^2} \begin{cases} \frac{1}{2} & \text{for } \beta\lambda/2 \text{ cell length} \\ 1 & \text{for } \beta\lambda \text{ cell length} \end{cases}. \tag{3.54}$$

These equations can be used to derive and illustrate the particle motions in phase space as shown in Figure 3.6. The boundary of the stable region depends on the synchronous phase ϕ_s, and is horizontally limited in phase by ϕ_r and ϕ_l, resulting in the total acceptance width $\Phi = \phi_r - \phi_l$ [69]:

$$\phi_r = -\phi_s \tag{3.55}$$

$$\tan(\phi_s) = \begin{cases} -\frac{\Phi}{3}, & \text{if } \phi_s \ll 1\,\text{rad} \\ (\sin(\Phi) - \Phi)/(1 - \cos(\Phi)), & \text{else} \end{cases} \tag{3.56}$$

and vertically by the maximum energy $E_{\max}$ of the acceptance

$$W_{\max} = \sqrt{\frac{2qE_0 T_{\text{TTF}} \beta^3\gamma^3\lambda}{\pi mc^2}(\phi_s \cos(\phi_s) - \sin(\phi_s))} \tag{3.57}$$

For a reference synchronous phase of $\phi_s = -30°$, all surrounding particles with a phase between $-60°$ to $30°$ and corresponding energy acceptance (see Equation (3.57)) are captured inside the DTL acceptance. This is advantageous because it provides continuous longitudinal focusing along multiple RF gaps, creating a stable transport region in phase space, where a rotational pattern is visible. This pattern is usually used for two purposes: acceleration and bunching. In an DTL accelerator applying a standard acceleration scheme, a synchronous phase about $-30°$ is commonly applied. The bunch must be injected into the DTL structure with respect to the separatrix, called *matched*. This results in successive acceleration through the RF gaps as the particles rotate around the center in longitudinal phase space.
For longitudinal rebunching, RF cavities with only a few gaps and a synchronous phase of $-90°$ are used. For effective rebunching a divergent bunch, elongated to max. $30°$, has to be injected. Due to the large rotational component in the phase space at this synchronous phase, the bunch is rotated from a divergent to a convergent position and thus focused without energy gain.

Transverse Focusing

Beam transport is limited by the transverse beamline aperture, whereas longitudinal bunch size is limited by the sinusoidal RF time dependence. Quadrupole multiplets

are most commonly used, providing transverse focusing in both transverse planes, while each quadrupole focuses in only one direction. For specific applications (e.g., matching to the acceptance of an RFQ) solenoids, which allow simultaneous focusing in both transverse planes, are employed. Transport in those elements can be described by a matrix multiplication of particle position and velocity with a matrix element describing the focusing properties:

$$M \cdot \vec{x} = \begin{pmatrix} a & b \\ c & d \end{pmatrix} \cdot \begin{pmatrix} x \\ x' \end{pmatrix}. \tag{3.58}$$

For a transport line with multiple elements and drifts the transport equation will consist of all elements i

$$\vec{x}_{\text{out}} = \prod M_i \vec{x}, \tag{3.59}$$

which must satisfy the following condition for stable transport in the absence of space charge effects [63, p.148]:

$$Tr\left(\prod M_i\right) \leq 2. \tag{3.60}$$

Space Charge

Charged particles repel each other by coulomb forces, resulting in an increase of effectively populated volume in phase space. The repelling force applied to each of the particles can be formulated as:

$$\vec{F_i} = \frac{1}{4\pi\epsilon_0} \sum_j^n q_i q_j \frac{r_i - \vec{r}_j}{|\vec{r}_i - \vec{r}_j|^3}. \tag{3.61}$$

This formulation is very general, but challenging for beam dynamics simulations, because every time the space charge has to be calculated, the distances between each particle must be calculated, a problem with $O(n^2)$ time complexity. This leads to performance bottleneck in simulations. In order to overcome this problem, the charged particle cloud can be binned into a grid where additional mathematical formulations are possible to solve the underlying Poisson equation and generate the electrostatic potential with the method of fast Fourier transformation, reducing the problem complexity to $O(n \log(n))$. This effect is important for dense, low β ion beams and various other high current beam applications. The Coulomb force provides for additional defocusing of the beam, to be considered for the design of the focusing system.

Emittance Growth

The initial particle distribution described in Section 3.1 is subject to many influences that lead to an increased effective emittance. There are non-linear forces, phase plane coupling, beam mismatch (especially longitudinal), space charge forces, collisions with stripping foils, and similar collisions that contribute to this effect [63]. Given the variety of causes, beam transport is more than often limited by the increase in emittance. For example, the effect of injecting a longitudinally mismatched bunch to the acceptance of an acceleration structure is shown in Figure 3.3.

3.3. EQUUS – Equidistant Multigap Structure

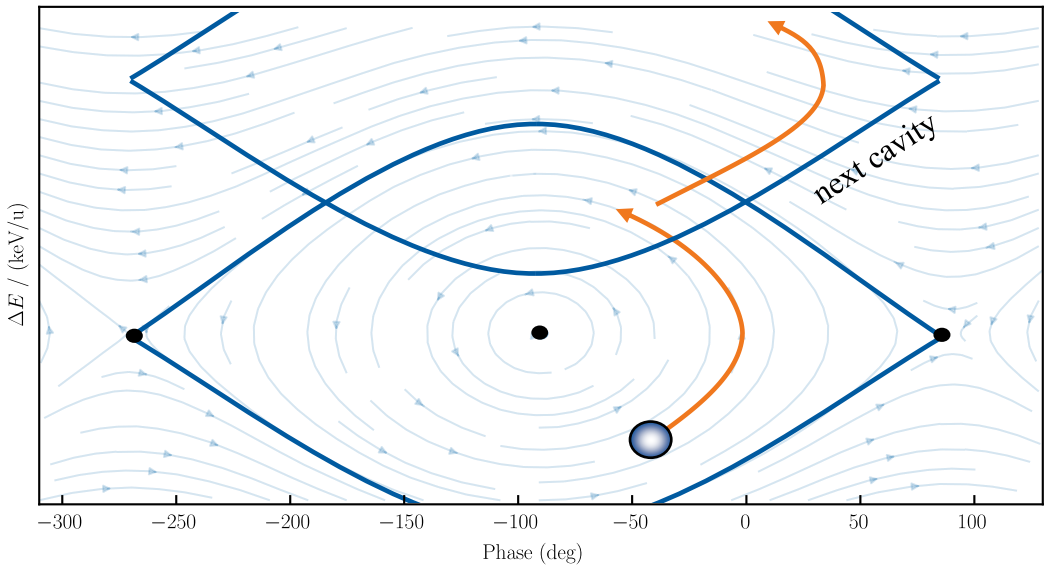

Figure 3.7: Working principle of **EQU**idistant m**U**ltigap **S**tructure (EQUUS) beam dynamics. A bunch is injected off-center into an RF cavity and thereby accelerated. The next cavity with higher reference energy ($\Delta E = 0$) repeats this acceleration scheme.

The EQUUS, developed by S. Minaev and U. Ratzinger [14], is a beam dynamics approach that allows alternating longitudinal and transverse focusing, and a variable output energy which is not available in conventional resonance accelerators.
The longitudinal symmetry resulting from equidistant gaps along the EQUUS structure opens the opportunity for faster beam dynamic calculations and for the reduction of construction costs. In both architectures, EQUUS and KONUS, the key element for planning and understanding beam dynamics is the distinction between a virtual lattice reference particle and the actual bunch, which are two different entities. The cell lengths in EQUUS structures are equidistant, i.e., they are constant. It is well known from conventional beam dynamics that a constant cell length implies zero acceleration of the hypothetical reference particle (with constant synchronous phase of $-90°$). The corresponding synchronous phase of a virtual reference particle is $\pm 90°$. Consequently, a stable phase space region is present around $-90°$ (see Figure 3.7). As the acceptance of a $-90°$ structure is maximal compared to any other synchronous phase, it is possible to inject a bunch (with smaller emittance as the acceptance) at a phase and energy different from the hypothetical reference grid particle. As the new injection point is not the stable point at $\phi = -90°$ and $\Delta E = 0$, the bunch moves in the phase space along the equipotential lines. If there is a significantly long structure, providing several periods of oscillation in phase space, the bunch circulates in the

phase space without energy gain. But as the EQUUS structures are built with short length, only a fraction of oscillation takes place within one structure and the movement in phase space stops at a given point, providing for high acceleration within the acceptance. Re-entering a next EQUUS cavity, also a virtual reference phase of $-90°$, but at a higher reference energy, the previous process repeats. Thus, acceleration is successively achieved. The variable energy is achieved by changing the acceleration voltage of the last cavities below their nominal gradient for focusing, whilst operating the first cavities with their nominal gradient in order to reach the target energy. Another benefit of the synchronous phase pattern is the increased mean acceleration phase. As the bunch phase is changed from gap to gap, also called *phase slip*, multiple phases around $0°$ are used for a more effective acceleration of the bunch. For example, a mean phase of about $-20°$ is the result of this behavior with the recent HELIAC design [11].

3.4. KONUS – Combined Zero Degree Structure

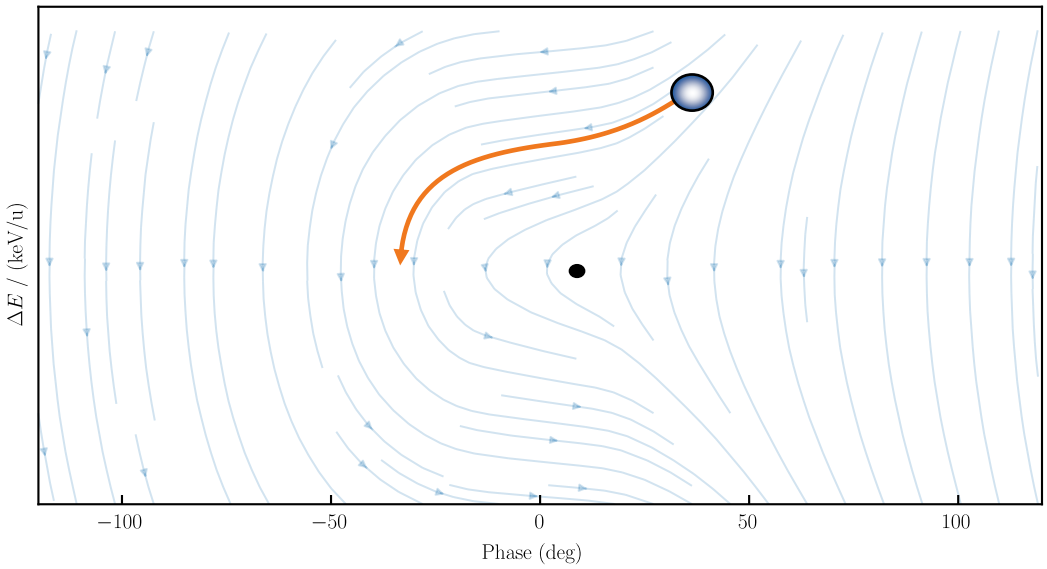

Figure 3.8: KONUS beam dynamics; the beam dynamics in phase space are derived using a grid reference particle of $0°$, The bunch is injected at a higher energy than the grid reference particle ($\Delta E = 0$), and thereby moves in phase space.

The underlying principles of Combined Zero Degree Structure (**KO**mbinierte **NU**ll Grad **S**truktur, KONUS) beam dynamics [52, 56, 89] are very similar to the EQUUS beam dynamics. Whilst EQUUS structures provide for efficient acceleration enabling a variable output energy, KONUS structures aim for high compactness and efficiency

of acceleration. Therefore, most of the KONUS structures are built with internal magnetic quadrupole lenses in order to omit enlarged drift sections, which arise from the use of external lenses. The longitudinal bunching is realized with dedicated embedded RF gaps operated at a negative particle synchronous phase $\geq -90°$. Multiple short acceleration sections are designed with a grid reference particle phase distinct from the actual bunch phases, as for the EQUUS structure. For EQUUS a $-90°$ geometric synchronous phase is chosen and the bunch is injected with $\Delta E < 0$ relative to the design injection energy; in KONUS beam dynamics the geometric synchronous phase is $0°$ and the actual bunch is injected with a higher beam energy $\Delta E > 0$ (see Figure 3.8). As mentioned above, these accelerating sections are necessarily separated by transverse and longitudinal focusing sections. The bunch is accelerated to the final energy using several of these KONUS periods. The KONUS beam dynamics has been successfully implemented to multiple accelerators among others: HLI, HSI, Proton Injector for the GSI FAIR facility and CERN LINAC3 [52].

3.5. APF – Alternating Phase Focusing

Alternating **P**hase **F**ocusing (APF) is a concept for beam dynamics relying on the change of particle synchronous phases during beam acceleration instead of applying a fixed synchronous phase over the entire length of a DTL [49]. Within the APF concept, both positive and negative synchronous phases are applied for beam acceleration, allowing sequential longitudinal and transverse RF beam focusing along the cavity. Generally, the application of quadrupole magnets for additional transverse focusing is influenced by constraints such as available aperture, initial beam emittance, operating frequency, maximum acceleration voltage, beam transmission, and tolerable emittance growth. The embedded transverse RF focusing applied in the APF scheme thus allows for longer quadrupole-free DTL periods, in contrast to traditional beam dynamics approaches.
To obtain a variation of synchronous phases, the length between two adjacent tube-centers has to be adjusted. For a beam transport with constant phase, a cell length of $\beta\lambda/2$ is required, depending on β, the particle velocity as a fraction of the speed of light, and λ, the RF wavelength. For the synchronous phase change between two adjacent gaps $\Delta\phi$, an altered cell length is required [49]

$$L_{\text{cell}} = \frac{\beta\lambda}{2} + \beta\lambda\frac{\Delta\phi}{360°}. \tag{3.62}$$

The APF beam dynamics scheme is a long-known approach in order to achieve successive transverse-longitudinal RF beam focusing, which was suggested in 1953 [90, 91]. However, there is no common agreement on the pattern of synchronous phases and how they should be distributed along multiple gaps. A sinusoidal synchronous phase law was proposed by I. Fainberg in 1956 [92], using the average acceleration field $\bar{E}$, the field factor η, and the amplitude of the synchronous phase oscillation α

$$\phi_i = \alpha\cos\left(\frac{\omega t}{n}\right) \tag{3.63}$$

$$n = \sqrt{\frac{\beta}{A(1-\beta^2)^{3/2}}} \tag{3.64}$$

$$A = \frac{\alpha}{\pi}\frac{e\bar{E}\eta\lambda}{mc^2} \tag{3.65}$$

but also distinct approaches have been proposed in the following years [93–96]:

- Irregular [97]
- Rectangular / step-function [98]
- Semi-sinusoidal [99, 100]

The two beam dynamics schemes KONUS and EQUUS can equally be considered as subclasses of the APF scheme, although they both do not aim to omit magnetic lenses. Recently, a semi-sinusoidal APF channel has been designed and is in routine operation at the **H**eavy **I**on **M**edical **A**ccelerator **C**enter (HIMAC) in Japan [94, 100]. Further application of the APF beam dynamics scheme is planned at different accelerator facilities, as at **J**apan **P**roton **A**ccelerator **R**esearch **C**omplex (J-PARC) in Japan for the Muon Linac [101] or at the Advanced Proton Therapy Facility (APTRON) in China [102].
In contrast to APF beam dynamics, the conventional synchronous phase structure usually uses a fixed synchronous phase, that results in focusing of the beam only in the longitudinal direction along with defocusing of the beam in the transverse direction. The transverse focusing is carried out by applying magnetic lenses. In this approach, the magnetic quadrupoles are placed in the interior of the resonators, which allows for a very space-efficient accelerator arrangement by avoiding any extra drift sections. For Alavarez resonators, the quadrupole lenses are usually mounted in almost every drift-tube; for H-mode resonators several larger quadrupole duplets or triplets can also be installed in enlarged, non-standard drift-tubes. This results in longer resonators that are more complicated to manufacture and maintain, as repairing and retrofitting the lenses inside the resonator is a difficult and time-consuming process. On the other hand, the emerging long tanks are more difficult to fabricate and to maintain, where the repair or replacement of inner-tank lenses is a challenging and time-consuming procedure. Linacs using the APF beam dynamics concept can mitigate these difficulties, since the APF concept generally allows for an arrangement without magnetic lenses (or a small set of external quadrupole lenses). The already built, up to 3.4 m long HIMAC section has been designed without quadrupole lenses, allowing heavy ion acceleration from 400 keV/u to 4 MeV/u with a mass-to-charge ratio of 3. This linac is routinely used as a cyclotron injector dedicated for heavy ion cancer therapy.

3.6. Solvers

Beam dynamics frameworks are applied to analyze and design accelerators. The availability of computing power has enabled development of various software pack-

ages for beam dynamics during past decades, as OPAL [103], TRACK [104], DYNAMION [60], MAD-X [105], LORASR [89], TRACEWIN [106], COSY-INFINITY [107] and DESRFQ [108]. Modern beam dynamics codes aim for 3D-collective and self-consistent calculation. This is achieved by analytic or iterative methods, depending on the purpose of application.

Calculation Methods

As outlined in Section 3, the particle transport can be described mathematically by introducing simplifications, or parameter limitations, for the beam transport elements. These equations can be implemented in computational solvers, enabling an efficient execution time. They either calculate the transport of each particle or, through further mathematical reformulation, the transport is represented by the enclosing ellipse of the particle ensemble. Ellipse transport codes are using symplectic transfer maps M and thus provide for mathematical systems that can be solved efficiently. This is an advanced approach, imposing some restrictions when modeling non-linear beam transport. A prevalent example of such class of code is TRACE3D [81], which is extremely useful for the prototyping of beamlines.

A more general approach to obtaining the trajectory of particles is to solve the relativistic equations of motion (derived from Equation (3.22) on page 26) in electromagnetic fields by formulating the problem as an ordinary differential equation and solving it with iterative methods such as the Runge-Kutta method. This can be achieved with either Hamiltonian or Newtonian mechanics, which solve the same problem by different parameterization. Widely applied is the **R**unge-**K**utta-**4** (RK4) method [109], which iteratively solves the equation $dy/dt = f(t, y)$ through

$$y_{n+1} = y_n + \frac{1}{6}h(k_1 + k_2 + k_3 + k_4) \tag{3.66}$$

$$t_{n+1} = t_n + h, \tag{3.67}$$

subject to the four coefficients

$$k_1 = f(t_n, y_n) \tag{3.68}$$

$$k_2 = f(t_n + h/2, y_n + k_1 h/2) \tag{3.69}$$

$$k_3 = f(t_n + h/2, y_n + k_2 h/2) \tag{3.70}$$

$$k_4 = f(t_n + h, y_n + k_3 h). \tag{3.71}$$

Furthermore, the adaptive Runge-Kutta-45 method is frequently used, in order to select the time step automatically to stay below a required error threshold. The error measure Δy_{n+1} is derived from comparing a time step with two different Runge-Kutta iterations $\Delta y_{n+1} = y_{\mathrm{RK5},n+1} - y_{\mathrm{RK4},n+1}$. If the error is too large, the step size could be reduced until the desired error margin is reached.

4. Tomography

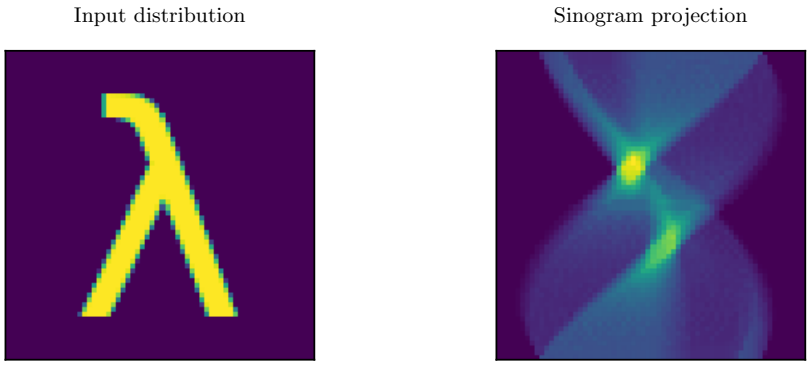

Figure 4.1: Input object (*left*) and its sinogram projection (*right*)

In order to perform a tomographic reconstruction of a $N+1$-dimensional object, a measurement series of N-dimensional data must be available [47]. The set of measurements is required to describe the to be reconstructed object from different directions (see Figure 4.1 and 4.2). As a consequence, the $N+1$-dimensional object can be recovered from the measurement set. In the following, it is assumed that a 2D object $f(u, v)$ is to be calculated from multiple 1D measurements $A_i(u')$. The mathematical methods for calculating $f(u, v)$ have already found broad application, for example in medical diagnostics, where the series of measurements is performed around a rigid body. Consequently, the mapping between measurement and object can be described using a rotation matrix. The measurement series is then processed into a so-called sinogram (see Figure 4.1) and can be used as standard input for various reconstruction algorithms. In accelerator physics, however, the mapping between the object to be measured, i.e., a particle bunch, cannot be described by means of rotation matrices alone. Rather, the mappings are based on shear matrices in the simplest case. Under certain conditions, these shear matrices can also be assigned to rotation angles in order to generate sinograms. However, in case of a non-linear beam transport [110] this is no longer possible. For example, if the bunch is too long for the beam transport through a rebuncher, the small angle approximation cannot be assumed. The employed reconstruction algorithms have to be adapted to a more general input in case of non-linear beam transport. The **M**aximum **EN**tropy **T**echnique (MENT) reconstruction method [111] and the **A**lgebraic **R**econstruction **T**echnique (ART) [112] have already been applied to the non-linear longitudinal phase space reconstruction [111, 113]. A different

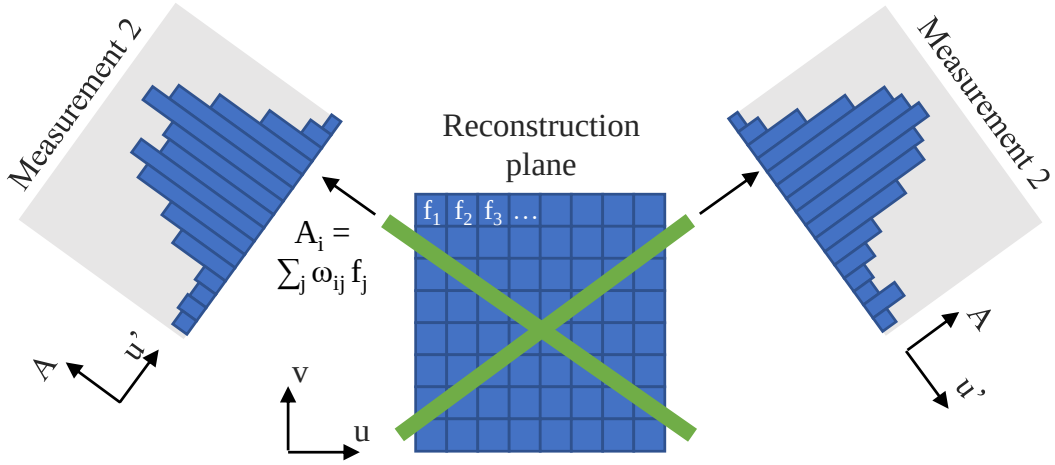

Figure 4.2: Common reconstruction problem; a set of histograms A or projections along different angles θ is known. From this information, the original distribution is recovered.

approach has been investigated for the HELIAC project. Instead of ART or MENT, the **N**on **N**egative **L**east **S**quares (NNLS) method [114] is used for the reconstruction. This method is closely related to the least squares fitting, but only allowing positive numbers as a solution. The application of this algorithm requires the description of the non-linear beam dynamics in terms of a system of linear dependencies.

Beam transport can be modeled by discrete mapping of input points or pixels f_j to measured histogram samples A_i (see Figure 4.2). How much a pixel is constrained by a histogram value is given by the weight coefficient ω_{ij}. With this formulation, the problem can be written as a system of linear equations, linking all measurements to the mappings of the input.

$$A_i = \sum_j^N \omega_{ij} f_j, \tag{4.1}$$

which can be rewritten as

$$\Omega \cdot \vec{f} = \vec{A} \tag{4.2}$$

with the matrix $\Omega_{ij} = \omega_{ij}$ and the count of all pixels N. Generally, this system of linear equations could be solved exactly, but for experimental data due to unavoidable noise effects and further constrains of the experimental setup an exact solution is infeasible. Multiple methods of obtaining an approximate solution exist and are discussed below.

4.1. Radon Transformation and Back-Projection

As one of the first reconstruction methods, the Radon transformation was introduced in 1917 by J. Radon [115]. The reconstruction method resembles the mathematical handling of the object on Figure 4.2 with a straight line L rather than a bar lying across the high dimension distribution. Using the polar coordinates θ and r, the radon transformation $R(f)$ can be expressed as

$$R(f(r,\theta)) = \int_{-\infty}^{\infty} f(rcos(\theta) - tsin(\theta), rsin(\theta) + tcos(\theta))\ dt \tag{4.3}$$

This resembles the integral over a perpendicular line to the radius vector at the point (r,θ). For the reconstruction of the original distribution from multiple projections, the inverse radon transformation, also called back-projection, can be used. As the data is going to be processed digitally, the discrete form of the back-projection is given by

$$f(x,y) = \frac{1}{2\pi} \sum_{i=1}^{N} \Delta\theta g_i(xcos(\theta_i) + ysin(\theta_i)), \tag{4.4}$$

where g_i is given by a $k(t)$ weighted histogram: $g_i(t) = A_i(t) \cdot k(t)$; $\Delta\theta$ is the angular distance between the projections. By applying a weight $k(t)$, this is called **F**iltered **B**ack **P**rojection (FBP) [116].

4.2. Algebraic Reconstruction Technique

The **A**lgebraic **R**econstruction **T**echnique (ART) algorithm is a widely used approach for tomographic reconstruction. The technique was employed in 1970 by Richard Gordon, Robert Bender and Gabor T. Herman in the field of electron microscopy and X-ray photography [112] and was already known as Kaczmarz method in 1937 [117]. ART is used to find an approximate solution to Equation (4.1). The reconstruction is uses Ω sliced into multiple parts $\vec{\omega}_m = (\Omega_{m,1}, \Omega_{m,2}, ..., \Omega_{m,N})$ and iteratively solves for $\vec{f}_m$:

$$\vec{f}_m = \vec{f}_{m-1} - \frac{\vec{f}_{m-1} \cdot \vec{\omega}_m - A_m}{\vec{\omega}_m^2} \vec{\omega}_m, \tag{4.5}$$

using an initial guess $\vec{f}_0$ [112]. The accuracy of the method increases with the number of measurements and is typically used with at least 100 projections. More recent implementations of the method are used to calculate the reconstruction in parallel, which is necessary when processing large amounts of data. This parallel method is well known as **S**imultaneous **A**lgebraic **R**econstruction **T**echnique (SART).

4.3. Maximum Entropy Technique

The **M**aximum **EN**tropy **T**echnique (MENT) algorithm solves the reconstruction problem based on Lagrange multipliers, maximizing the entropy from measurements to reconstruction. The derivation of the iterator is beyond the scope of this work and can be found in [111]. The reconstructed image f(u,v) is expressed as the scalar's product along the k-th observation axis u'_k and along the binning axis v'_k, which is perpendicular to u'_k:

$$f(u,v) = \prod_{k}^{K} h_k(u'_k). \tag{4.6}$$

The k-th histogram can thus be expressed as line integral:

$$A_k(u'_k) = \int f(u,v)\, dv'_k = h_k(u'_k) \int \prod_{k'|k'\neq k}^{K} h_{k'}(u'_{k'})\, dt_k. \tag{4.7}$$

This is re-arranged in order to iteratively solve for partial projections $h_k^i(u'_k)$.

Algorithm 1: Maximum Entropy Technique[1]

Data: A_k, u'_k, v'_k
Initialize $h_k^0(u'_k) = \vec{1}$,
while $\sum_k^K \mid A_k - \int \prod_{k'}^K h_{k'}(u'_{k'})\, dt_k \mid / A_k > 1\%$ **do**
  Update $h_k^{i+1} = \frac{A_k(u'_k)}{\int \prod_{k'|k'\neq k}^K h_{k'}^i(u'_{k'})\, dv'_k}$
end
Calculate reconstruction $f(u,v) = \prod_k^K h_k(u'_k)$
Result: $f(u,v)$

For implementation of vectorized calculations (see Algorithm 4 on page 113), the discretization of the image function $f(u,v)$ can be expressed as 1D vector $\vec{f}$. The algorithm is rewritten by means of discrete mappings using the matrix Ω_k, linking the image space $\vec{f}$ to the k individual measurement spaces $\vec{A}_k$ (see Equation (4.2)).

[1] Maximum Entropy Technique algorithm [111]

4.4. Non Negative Least Squares

The **N**on **N**egative **L**east **S**quares (NNLS) algorithm is a general approach for solving a system of linear equation and was published in 1974 [114]. This solver is implemented in the well-known PYTHON package SCIPY (ScientificPython) [118], highly accessible to a broad research community. The solver is not specifically designed for tomographic reconstruction, providing for the solution of the following minimization problem.

$$\text{minimize} \qquad |\Omega\vec{f} - \vec{A}| \tag{4.8}$$

$$\text{subject to} \qquad \vec{f} \geq 0 \tag{4.9}$$

Nevertheless, it is applicable to the reconstruction problem to minimize the difference between the observations and the reconstructed shape. This solver works with two sets P and R, which are used to handle and remove negative values from the result iteratively on top of the usual Least Squares algorithm. Let the notation for a sub-selection of a vector be $A_S : (A_{i_1}, A_{i_2}, ...A_{i_n} \mid i \in S)$. Thus, the algorithm solves Equation (4.1), but only yields positive entries in the result vector $\vec{f}$ [114].

Algorithm 2: Non Negative Least Squares[2]

Data: Ω, $\vec{A}$, ϵ
$P = \varnothing$
$R = \{r \in \mathbb{N} \mid r \geq 0, r \leq n\}$
$\vec{f} = \vec{0}$
$\vec{w} = \Omega^T(\vec{A} - \Omega\vec{f})$
while $R \neq \varnothing$ *and* $\max(\vec{w}_R) \geq \epsilon$ **do**
  $j = \text{argmax}(w_R)$
  move j from R to P
  $\vec{s}_P = ((\Omega_P)^T\Omega_P)^{-1}(\Omega_P)^T\vec{A}$
  $\vec{s}_R = \vec{0}$
  while $\min(\vec{s}_P) \leq 0$ **do**
    $\alpha = \min(\{\vec{f}_i/(\vec{f}_i - \vec{s}_i) \mid i \in P, \vec{s}_i \leq 0\})$
    $\vec{f} \leftarrow \vec{f} + \alpha(\vec{s} - \vec{f})$
    move j from R to P if $x_j \leq 0$
    $\vec{s}_P = ((\Omega_P)^T\Omega_P)^{-1}(\Omega_P)^T\vec{A}$
    $\vec{s}_R = \vec{0}$
  end
  $\vec{f} \leftarrow \vec{s}$
  $\vec{w} \leftarrow \Omega^T(\vec{A} - \Omega\vec{f})$
end
Result: $\vec{f}$

[2]NNLS algorithm [114]

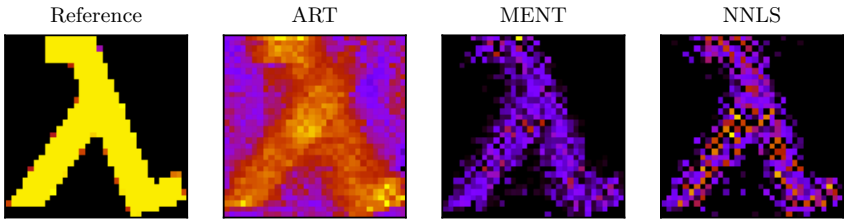

Figure 4.3: Exemplary reconstruction of a lambda-symbol with different reconstruction techniques (ART, MENT, NNLS) and 20 different measurements as input.

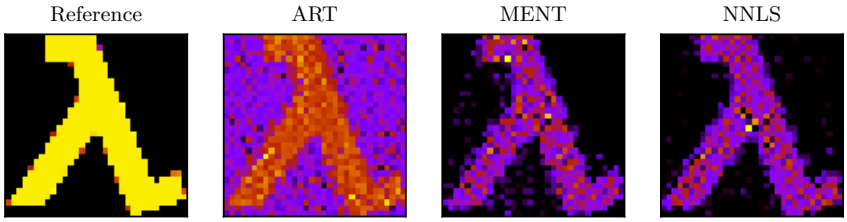

Figure 4.4: Exemplary reconstruction of a lambda-symbol with different reconstruction techniques and 100 different measurements as input.

The example reconstructions depicted in Figure 4.3[1] show that the result of the ART algorithm is poor for a small number of measurements, while the MENT and NNLS algorithms recover the shape well with some artifacts in the amplitudes. For a high number of measurements (see Figure 4.4), the ART algorithm produces fewer artifacts while being very efficient in terms of execution time, since there is only one calculation along the Ω matrix. The NNLS algorithm has been chosen for the solution of the accelerator physics tasks described further on, because of the strong limitation of available measured data. The use of as few measurements as possible is necessary to keep the laboratory data acquisition time as short as possible.

[1]The reconstruction methods were implemented in PYTHON according to the previous section.

5. Injector Optimization – Reconstruction in the Longitudinal Phase Space

5.1. Motivation

For improved accelerator performance, optimal beam matching must be achieved. Standard beam diagnostic equipment, such as phase probe sensors, are not sufficient to measure the longitudinal bunch length with high precision. A Feschenko-type **B**unch **S**hape **M**onitor (BSM) [58, 119] has been installed in 2018 at the Demonstrator beamline, allowing precise measurements of the longitudinal bunch length. A multiple of those accurate measurements can be combined with beam dynamics calculations in order to reconstruct the bunch shape and density-distribution in the longitudinal phase plane. The employed reconstruction method, the reference measurements and possible applications are presented in this chapter, which builds upon the published article *Longitudinal Phase Space Reconstruction for a Heavy Ion Accelerator* [47].

The BSM was installed in the Demonstrator beamline behind the injector linac HLI, comprising one IH and two rebuncher cavities, as well as behind the test cryostat for the SC CH0 acceleration cavity (see Figure 5.1). At this position, it is possible to produce different bunch shapes by changing the rebuncher field strengths (and furthermore by powering CH0, resulting in non-linear beam dynamics effects; see Section 5.3.4). The variability of the bunch shape allows, similar to standard tomography procedures, the reconstruction of the phase portrait from a set of measurements.

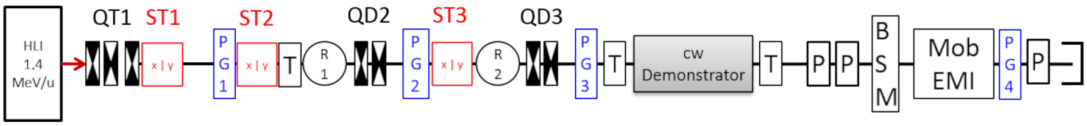

Figure 5.1: Demonstrator beamline; QT: Quadrupole Triplet, QD: Quadrupole Doublet, R: Rebuncher, x—y: Beam Steerer, PG1-4: SEM-Grid, T: Beam Current Transformer, P: Phase Probe, BSM: BSM, EMI: Emittance Meter [9].

Hence, at the chosen BSM position (and by applying the introduced reconstruction method), there are two options to improve the delivered beam quality for the SC CW Demonstrator:

1. Optimization of the HLI-IH amplitude and phase to deliver a high quality beam.
2. Setting the optimal Twiss parameters by using a dedicated rebuncher field strength in order to inject the beam into the CH cavity.

For both purposes, the longitudinal portrait of the bunch has to be recognized.

5.2. Reconstruction Method

To reconstruct the longitudinal phase portrait of the bunch, a series of measurements must be obtained in which the bunch is visible from different directions (see Figure 5.2). For this purpose, two rebunchers are used to provide different longitudinal bunch projections, which are to be measured with the BSM of Feschenko-type.

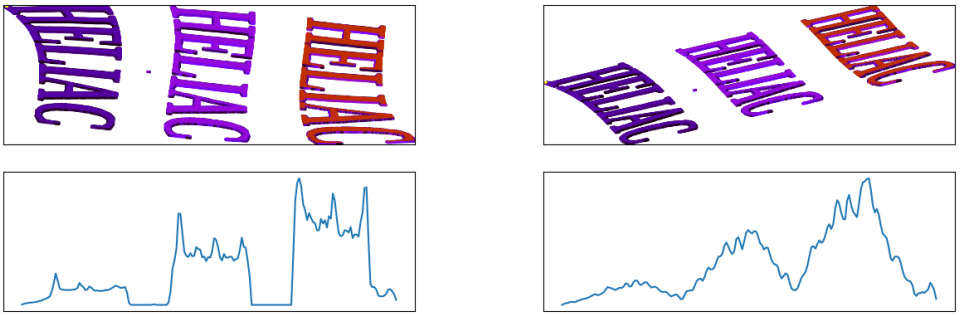

Figure 5.2: Transformed input image (colors indicating density, *top*) and corresponding measured histograms (*bottom*); the histograms are used to reconstruct the original image [47].

5.2.1. Bunch Shape Monitor

The main measuring device is a Feschenko-type BSM. It provides for measurements of the longitudinal bunch-density profile and offers a measurement accuracy of up to 0.5° at an operating frequency of 108.408 MHz, which allows using the measurements as input for the reconstruction in the longitudinal phase space. The BSM is positioned at the end of the line downstream the two rebunchers R1, R2 and the cavity CH0 (see Figure 5.1). The BSM operational principle (see Figure 5.3) is based on a thin metal wire, moved into the beamline, and measuring the secondary electron emission, which is induced by the beam-wire interaction. A high frequency electric field deflects the secondary electrons and translates the longitudinal, temporal secondary electron current signal into a spatial signal. This current is measured with a secondary electron multiplier. A more detailed publication on the Feschenko-type BSM is presented in [58, 119, 120].

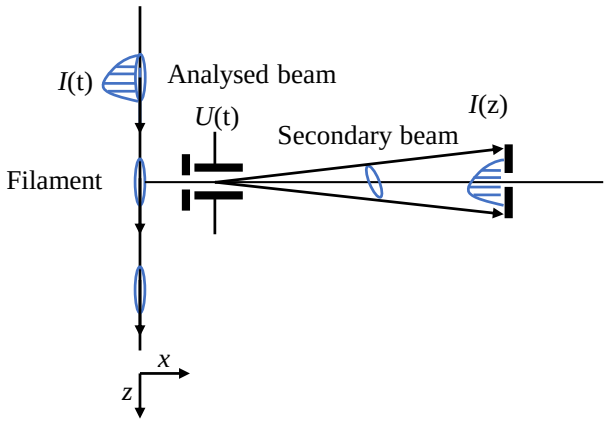

Figure 5.3: Basic principle of the Feschenko-BSM (from [58], edited).

5.2.2. Implementation of the Reconstruction

In order to conduct the reconstruction, the mapping from the input longitudinal phase space at the beginning of the beamline (i.e., end of the HLI) to the longitudinal phase space at the Feschenko-BSM must be known. To calculate the non-linear beam transport, DYNAMION [60], a 6D coupled beam dynamics code for linear accelerators, has been used. This code allows the tracking of individual particles, which is necessary for the creation of the non-linear mapping. Using a grid as input distribution and calculating its trajectories within the beamline allows mapping of two distinct positions in the beamline as a function $\vec{f}_i(\vec{x}_{\mathrm{in}})$ (see Figure 5.4). The transport section can be described in the absence of space charge effects. The required mapping function connects the longitudinal phase space at HLI and the phase space

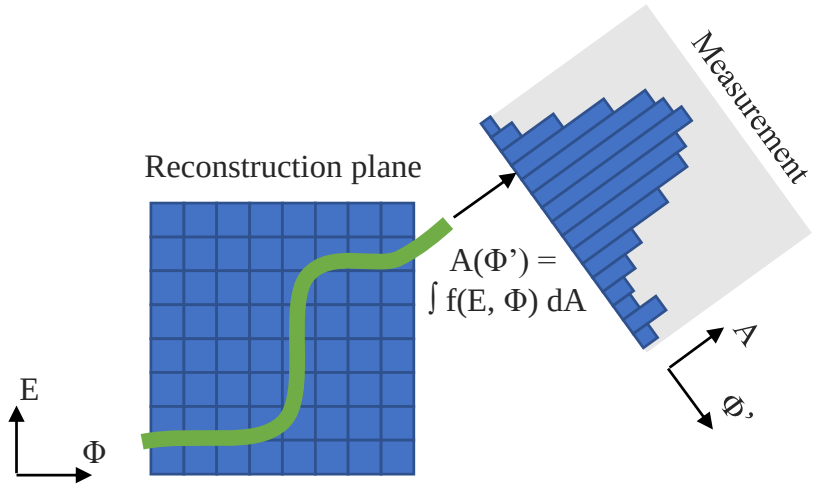

Figure 5.4: The input distribution $\vec{X}_{\text{in}}$ is non-linearly transported through the beamline and projected to $A_i(\phi, \vec{X}_{\text{in}})$, i.e., measured. Different mappings allow measurements of the input distribution from different directions.

at the BSM at the end of the line. Consequently, multiple mappings are produced for the different rebuncher setting i.

A measurement can be formulated as $A_i(\phi, \vec{X}_{\text{in}})$, using a set of input coordinates $\vec{X}_{\text{in}}$. Hence, for any particle output phase ϕ, different combinations of input conditions $\vec{x}_{\text{in},i}$ exist: $\vec{x}_{\text{in},i}(\phi)$ is ambiguous[1]. Therefore, a line at the input plane corresponds to a single phase in the output plane (see Figure 5.4). The orientation and shape of the line is influenced by the field strength of the rebuncher cavity. For each mapping, the intensities can be projected back along their corresponding line in the input plane.
Furthermore, by combining all back-projections, where a bunch signal was measured, an image is obtained, where the bunch is present and where it is not:

$$N_i(\vec{x}_{\text{in}}) = |\{\phi_i(\vec{x}_{\text{in}}) | A(\phi_i(\vec{x}_{in})) \neq 0\}|. \tag{5.1}$$

This fast operation is used to define the area, in which the reconstruction method has to be applied.

The mapping connecting input $\vec{X}_{\text{in}}$ and the measurements $A_i(\phi, \vec{X}_{\text{in}})$ can be represented by a matrix product $\vec{A}_i = B_i \cdot \vec{X}$, a discrete formulation of the mapping, which accounts for the discrete measurements and particle positions. Beyond that, using discretization allows expressing non-linear mappings with B_i, which is necessary because the beam transport through the rebuncher is generally non-linear. Finally,

[1] E.g., a fast particle with a low input phase and a slow particle with a high input phase both can be measured at the same phase in a distant point.

the different mappings for each rebuncher setting and corresponding measurements are combined in the equation $\vec{A} = B \cdot \vec{X}$, whereas the dimensionality of B is defined as the ((*number of measurements* times the *number of points per measurement*) times *number of input grid points*).

The Least Squares (standard) method for solving such a system of linear equations would also allow negative solution values. Negative solution values however correspond to negative particle intensities, which is non-physical as a positively charged beam is employed. Therefore, the additional condition $\vec{X} \geq 0$ is required. This constraint renders the method a **N**on **N**egative **L**east **S**quares problem (see Section 4.4 on page 47):

$$\text{minimize} \quad f(\vec{X}) = |B\vec{X} - \vec{A}| \tag{5.2}$$

$$\text{subject to} \quad \vec{X} \geq 0 \tag{5.3}$$

The mapping from the input ensemble $\vec{X}$ to the measurement space $B\vec{X}$ shall result in minimal difference to the actual measurements $\vec{A}$. Since $\vec{A}$ is known from measurements and B is produced from simulations, the unknown variable is $\vec{X}$, which can be solved, yielding the bunch intensity at each discrete input position.

There are two main pitfalls, which can occur during implementation:

- The measurements are too narrow to cover the whole input distribution. The measurements need to be zero-padded in this case to ensure that each pixel is weighted correctly.
- In contrast, the input distribution may be too narrow to span a whole measurement.

If the measurement is thus too wide and not assigned by a signal in the protruding area, the part of the measurement is omitted. But if the protruding area is filled by a signal, the limits of the input distribution have to be adapted.

5.3. Results

5.3.1. Measurements

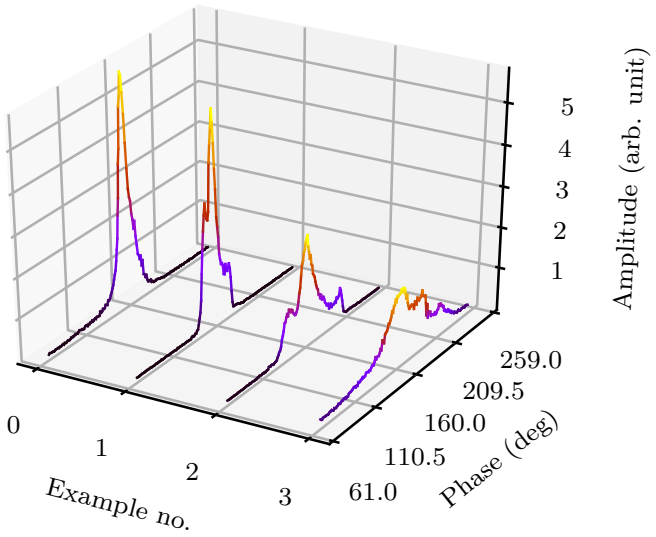

Figure 5.5: Examples of the bunch shape measurements with the BSM for 4 different rebuncher settings (108 MHz), the color corresponds to the respective amplitude [47].

All quadrupole and steerer magnet strengths were optimized for minimum beam loss by aligning the beam to the reference axis. Since the amplitude of the rebuncher is varied, it is particularly important to pass through the rebuncher aperture without beam displacement to prevent beam steering. A wide range of rebuncher parameters were measured with Ar^{9+} beam from the HLI. Finally, about 100 measurements were obtained. About 20 settings were used, in which the first rebuncher served as a debuncher[2]. It is particularly important to measure the setting range for a well-focused beam, as this is the setup, where the orientation of the bunch changes considerably. Exemplary measurement results are depicted in Figure 5.5. The measured beam profiles indicate a non-Gaussian beam profile, which is expected from the non-linear KONUS beam dynamics (see Section 3.4) used in the HLI-IH DTL. For this reason, the reconstruction must be carried out with advanced tomographic methods since the beam could not be represented as an ellipse[3]. After analyzing the measurement data, it has been decided to remove 6 % of the peak amplitude in each measurement in order to reduce background noise. In addition, the measurements were aligned to their common center of weight. In accordance with the algorithm, the beam transmission was assumed to be 100 %. The BSM graphs are presented with the head of the beam

[2]The rebuncher is thus operated at a synchronous phase of +90° instead of −90°.
[3]In case of an ellipsoidal shape, more simple algorithms are available.

on the right and the tail on the left. In the following, the phase planes are shown according to the same convention.

5.3.2. Reconstruction

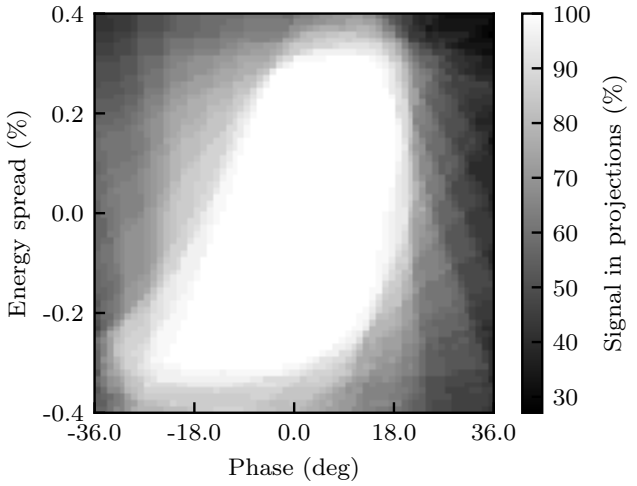

Figure 5.6: Back-projection of the measurements to the phase plane at the input position; areas, where all measurements indicate a signal are marked in *white*, i.e., 100 %. Darker regions indicate a lower probability for bunch existence in those areas [47].

As described in Equation (5.1), by backtracking and overlapping several measurements in the input plane, regions are determined, where the bunch is probably present. This simplification can be used as a shortcut to determine the phase and energy regions, in which the reconstruction algorithm should be applied.
This two-stage procedure of back-projection and subsequent NNLS reconstruction increases the speed of evaluation. In addition, applying two algorithms independently ensures algorithm integrity. For back-projection, not the raw signal is back-transformed, but a binary signal, that only differentiates between bunch presence and non-presence. This allows to distinguish between two regions (see Figure 5.6):
white: all measurements indicate a signal in the region, *black*: almost no measurement indicates a signal in the region. Since the measured data, represented as histograms, is obtained from different directions on the input phase plane, a histogram for almost every region indicating the signal strength, is present. This effect causes the 30 % background signal in Figure 5.6. The RMS emittance for this region is $\hat{\epsilon}_{\mathrm{RMS}} = 18\,\mathrm{keV/u\,deg}$ and is in accordance with the HLI design emittance of $14\,\mathrm{keV/u\,deg}$ [52]. The backtracked emittance is higher than the design value due to the binary signal chosen for backtracking. With the boundary values potentially obtained from the backtracking, the actual reconstruction is carried out with the NNLS procedure to create the precise phase space portrait. For this, the actual measurements are used instead of the binary

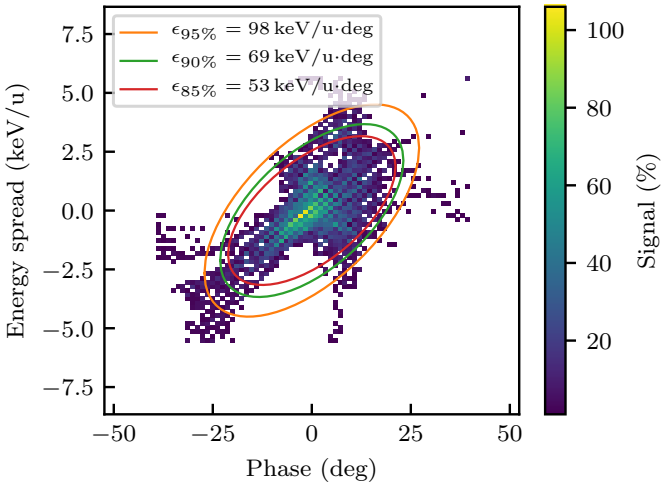

Figure 5.7: Brilliance analysis of the reconstructed distribution: Samples of the fitted ellipses according to a fraction of the density-distribution [47].

ones (which differentiates between bunch presence and non-presence). The reconstruction reveals a complicated bunch structure (see Figure 5.7). The RMS emittance is $\hat{\epsilon}_{\mathrm{RMS}} = 14\,\mathrm{keV/u\,deg}$. In the center of the particle distribution, a small region of high particle density can be seen, surrounded by a halo of low density.
The brilliance analysis of the bunch, which fits the n-percent part of the density-distribution by an ellipse, is shown in Figure 5.8. The small core of the bunch, as well as the beam halo, can be seen from the analysis results. The 90 % to 100 % ellipses are dominated by marginal particles. The analysis results fit well within the HLI design emittance $\hat{\epsilon}_{90\%} = 53\,\mathrm{keV/u\,deg}$ [52].

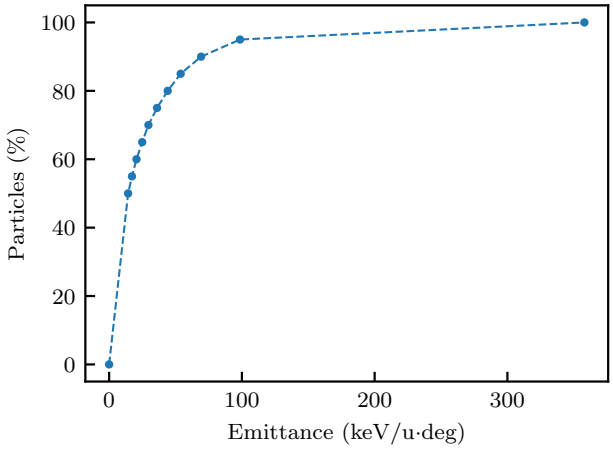

Figure 5.8: Beam brilliance analysis of the reconstructed distribution: Relation of the emittance on the fraction of particles [47].

All results above were obtained using only one BSM. Recently, a second BSM was mounted and put into operation at a different position directly at the exit of the HLI (i.e., at the reconstruction point), allowing for detailed investigation of the reconstruction accuracy by comparing the measurements at the second BSM to the reconstruction results (see Section 5.3.5).

5.3.3. Reconstruction on Reduced Number of Measurements

In order to complete the reconstruction as time-efficient as possible, it is necessary to carry out as few measurements as possible in order to keep accelerator operation as undisturbed as possible. On the one hand, this reduces the time required for the measurement and on the other hand, it also reduces the run-time of the reconstruction algorithm, since the system of equations to be solved has lower dimensionality by using fewer measurements. For the application considered herein, the use of 10 partial measurements represents a sufficient compromise between accuracy and calculation speed (see Figure 5.9).
In order to carry out the reconstruction with few measurements, it is important to choose the amplitudes of the rebuncher carefully, so that the bunch is measured from different directions. An approach to the analysis of the settings is given in *Beam Tomography Research at Daresbury Laboratory* [111]. Profiling the quality of the reconstruction, the coefficient of determination R^2 has been used [121], which is a regression score that normally yields values between 0 and 1, where 1 is the best value. It compares the measurements y_i and the fitted data $\hat{y}_i$ as

$$R^2 = 1 - \frac{\sum(y_i - \hat{y}_i)^2}{\sum(y_i - \bar{y})^2} \tag{5.4}$$

For the regression score given in Figure 5.9, the bunch was only reconstructed using about 10 measurements, but 10 times more measurements are used to calculate the regression score. This method is used for validation, as the consistency of the reconstruction results with the measurements is demonstrated, even if only a smaller subset of measurements is available for reconstruction.

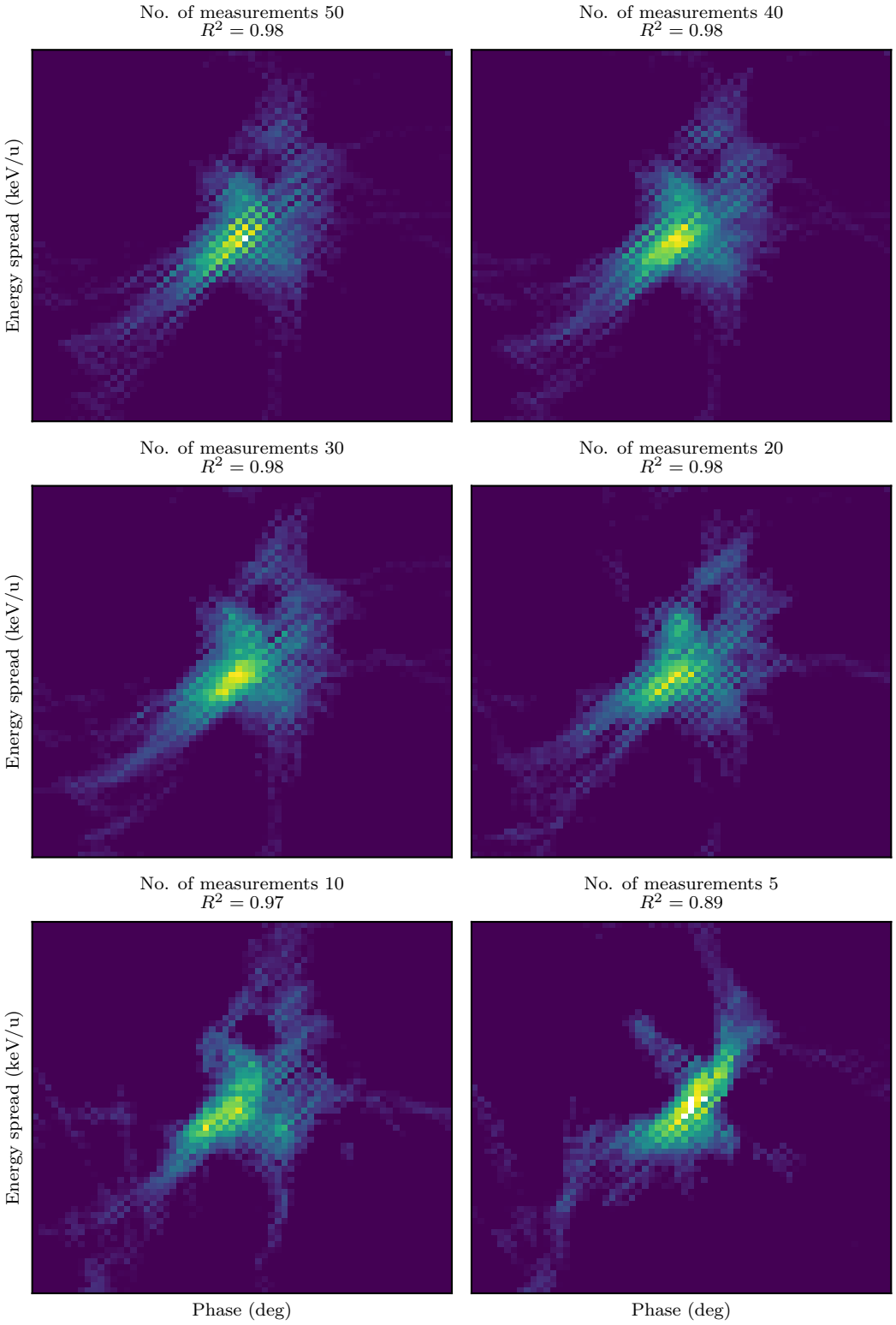

Figure 5.9: Reconstruction results for different measurement numbers as input; the reconstructed beam shape remains equal [47].

5.3.4. Validation – Cavity Phase Scan

For further validation of the reconstructed beam shape, another element with strong influence on the longitudinal beam dynamics has been used, which was not operated before: the cavity CH0. With the EQUUS beam dynamics, this cavity introduces a more complicated beam transport for calculation due to a combination of nonlinearity and acceleration. The measurements behind the cavity can only be reproduced if a realistic beam is used as input and if the beam dynamics are modeled accurately. The acceleration voltage of the cavity was set to a medium gradient of $U_0 = 3.3\,\mathrm{MV}$. In order to focus the beam longitudinally inside CH0, the voltage of the rebuncher was tuned and then fixed for the following measurements. The RF phase of the cavity was varied in full range to perform multiple profile measurements (see Figure 5.10).

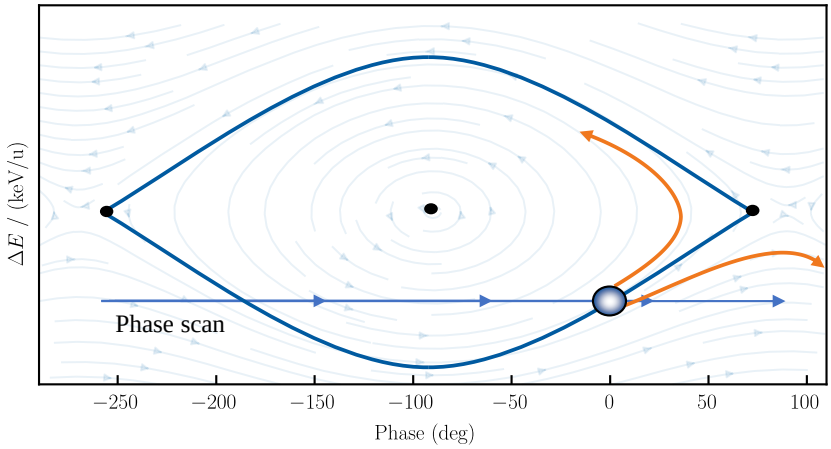

Figure 5.10: A phase scan can be depicted as injection of the bunch at different phases in relation to the cavity acceptance. At some point, the bunch is torn apart because one fraction is inside the separatrix and the other fraction is outside.

Figure 5.11 depicts, that different bunch shapes are produced at the BSM behind CH0 during the phase scan. The measurements range from very peaked shapes to flat shapes. This is confirmed by equivalent simulations. The flat measurements are obtained, when the bunch is injected at the edge of the separatrix. A part of the bunch remains inside the separatrix and is accelerated to a high energy region, whereas the other part is outside the separatrix and stays at a low energy. The bunch is thus torn apart. The simulations are in agreement with the measured data, the coefficient of determination is $R^2 = 0.79$ and therefore lower than the coefficients in the previous section. This is because further measurements were used to calculate R^2, which are independent on the data yielding the reconstructed bunch. Furthermore, beam losses occur in some cavity phase settings, whereas the simulations do not reflect this effect because only longitudinal beam transport is modeled. Omitting the transverse losses and their coupling to the results contributed to a decreased score as well.

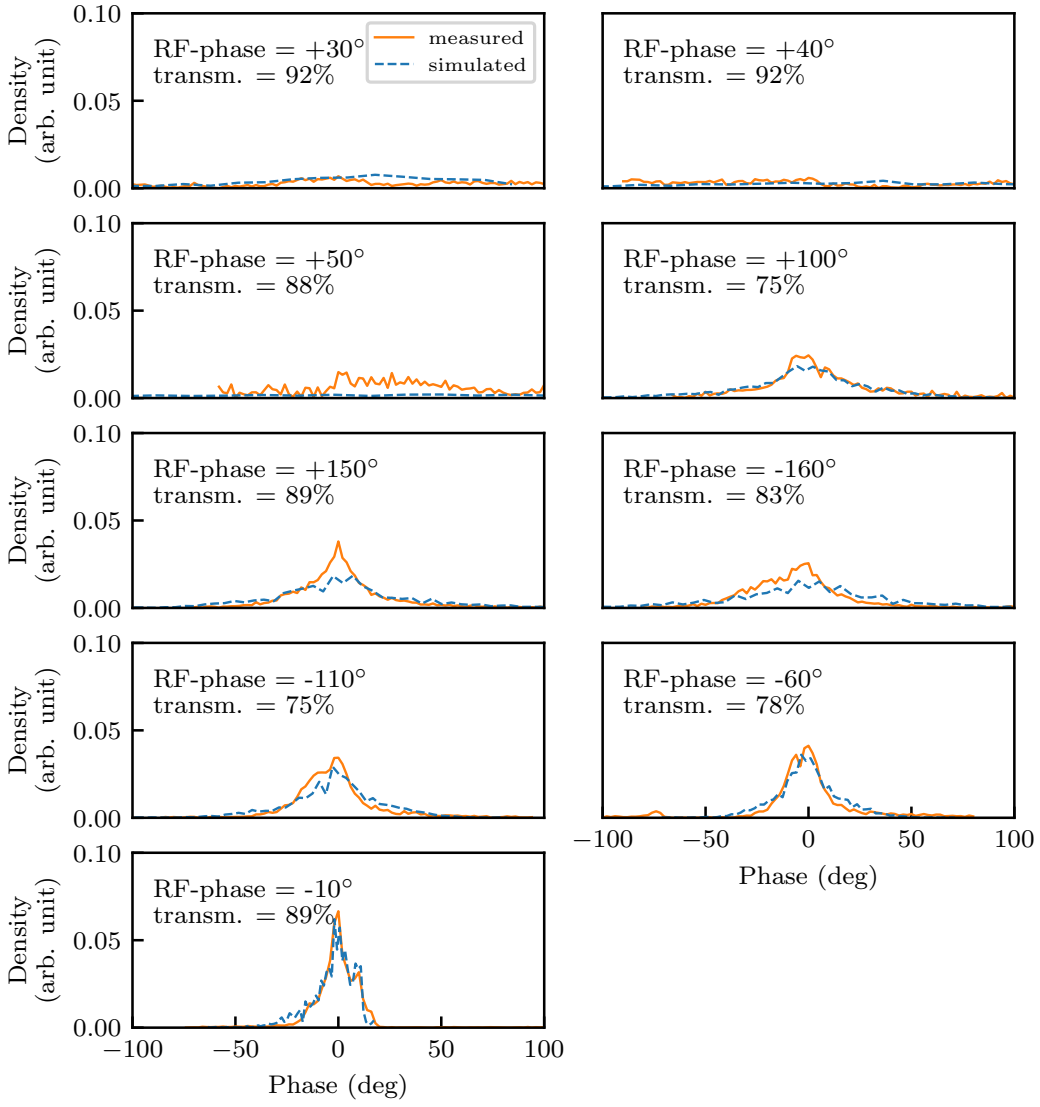

Figure 5.11: Measured longitudinal output beam profile as function of the RF phase of CH0. Additionally, the phase scan is reproduced with DYNAMION simulations using the reconstructed bunch shape as input distribution [47].

5.3.5. Validation Measurements with two Bunch Shape Measurement Devices

An additional Feschenko-BSM was mounted behind the HLI-IH, i.e., the position of the longitudinal phase space reconstruction. It has been an opportunity to compare the reconstructed 2D density of the particle distribution with the 1D measurements directly in-place. The Figures 5.12–5.13 show the results of this extensive measurement campaign. The reconstructed bunch shape is depicted on the left side, the corresponding ellipses enclose 100 %, 90 % and 85 % of the particles and their respective emittance values are noted. On the right side the 1D histogram of the reconstructed bunch (in blue color) and the actual measurements (in orange color) are depicted. Two types of scores are calculated: R^2_{train} and R^2_{test}. The training score is calculated from all measurements used as input for the reconstruction and represents the internal accuracy of the reconstruction algorithm. The test score is calculated to compare the reconstruction and the independent, direct measurement at the reconstruction point with the additional BSM measurement. The test score indicates how well a new measurement is predicted.

In general, the reconstructed bunch shape matches very well to the corresponding measurements (the regression score is about $R^2_{\text{test}} = 0.95$). A minor mismatch between the measurements and the reconstruction is visible in the regions of very low, as well as peaked signal, especially for Figure 5.12(a)–5.13(a). For these measurements, the rebunchers were not conditioned for an operation at low amplitudes, which rendered some measurements infeasible. This was fixed later, resulting in a more accurate reconstruction of the background (Figure 5.13(b)) and a more accurate representation of the 100 %, 90 % and 85 % emittances, which leads to weaker comparability with the previous reconstructions. Nevertheless, the maximum reconstruction accuracy was missed, as a 5 % mismatch in set-point and actual rebuncher voltage was present in one of the rebunchers. The measurement campaigns were nevertheless very successful.

The HLI sensitivity and its impact on beam quality has been demonstrated and documented: for a well-tuned injector setting an emittance of about $\hat{\epsilon}_{90\,\%} = 65\,\text{keV/u}\,\text{deg}$ is calculated, for an intentionally detuned setting the longitudinal emittance increases to 74 keV/u deg, a difference of 13 %. Furthermore, the initial measurements (Figure 5.7) and the measurements carried out one year later (Figure 5.12–5.13) showed fluctuations of machine parameters. The longitudinal focusing of the HLI-buncher (which matches the beam to the HLI-IH) has an influence on the longitudinal bunch emittance by up to an order of magnitude.

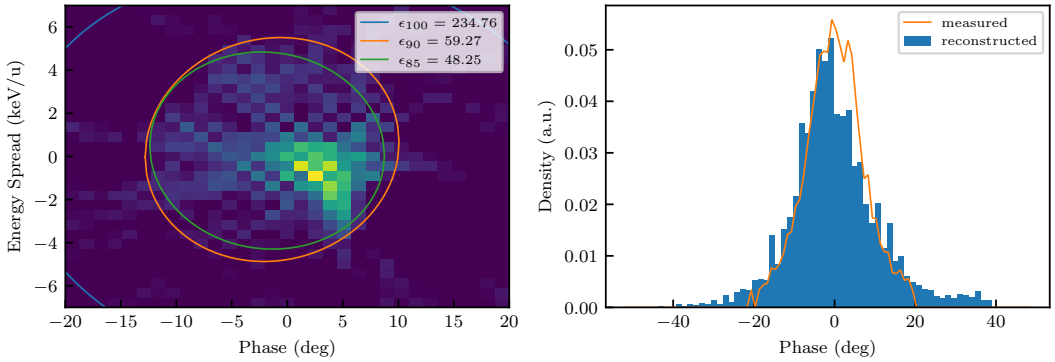

(a) HLI-IH control setting: 4.04 V, 119°, 27.05.2021, $R^2_{\text{train}} = 0.95$, $R^2_{\text{test}} = 0.94$

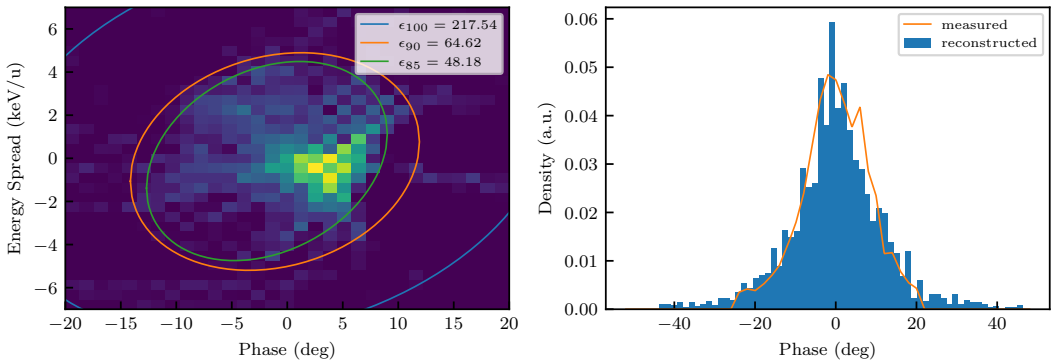

(b) HLI-IH control setting: 4.04 V, 110°, 28.05.2021, $R^2_{\text{train}} = 0.96$, $R^2_{\text{test}} = 0.95$

Figure 5.12: Reconstructed longitudinal particle density-distribution (*left*) and validation of the reconstruction with a dedicated, independent BSM (*right*).

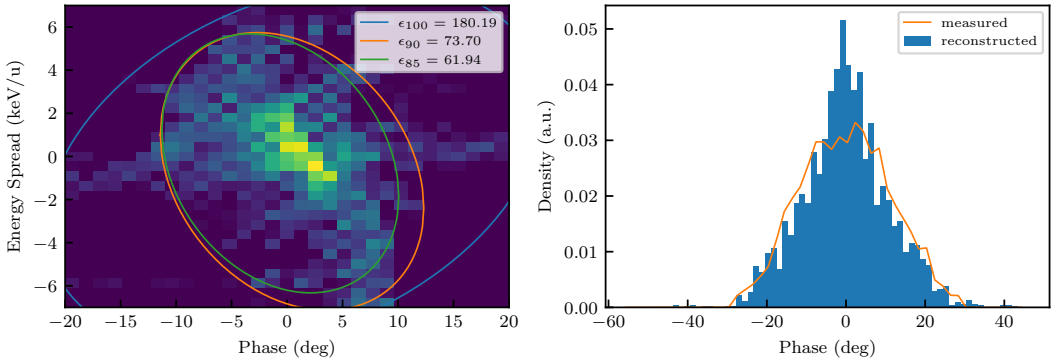

(a) HLI-IH control setting: 4.08 V, 122°, 28.05.2021, $R^2_{\text{train}} = 0.95$, $R^2_{\text{test}} = 0.86$

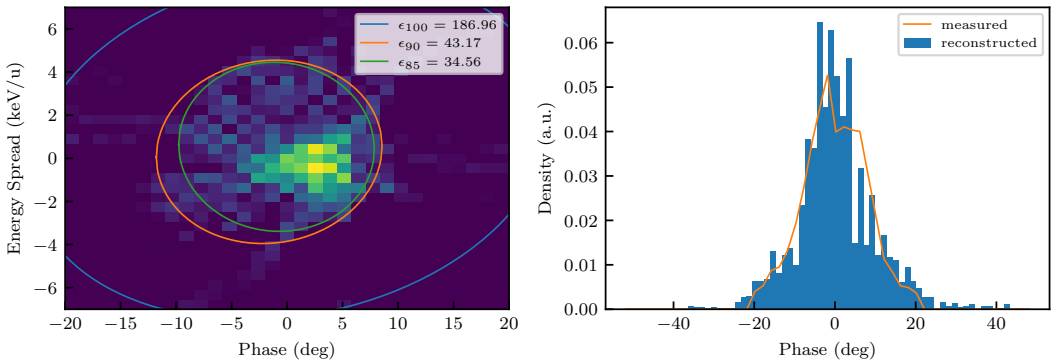

(b) HLI-IH control setting: 4.04 V, 119°, 31.05.2021, $R^2_{\text{train}} = 0.98$, $R^2_{\text{test}} = 0.90$

Figure 5.13: Reconstructed longitudinal particle density-distribution (*left*) and validation of the reconstruction with a dedicated, independent BSM (*right*).

5.3.6. Comparison with MENT Reconstruction

As described in the previous section, it was possible to measure the bunch shape directly at the reconstruction point. This allows a comparison of the beam shape of the reconstructed bunch with the direct measurements and enables a benchmarking of the different reconstruction algorithms. As depicted in Figure 4.3, it can be assumed that the results of the **M**aximum **EN**tropy **T**echnique (MENT) and NNLS (see Section 4.3 and 4.4 on page 46 ff.) reconstruction are quite similar for idealized inputs. In the following, the MENT reconstruction is applied to our actual measurement data from the previous Section 5.3.5.

In Figure 5.14[4] the reconstruction results obtained with the MENT algorithm are depicted. The particle density-distribution appears much smoother as with the NNLS reconstruction and tends to have fewer artifacts in the outer low-density region.

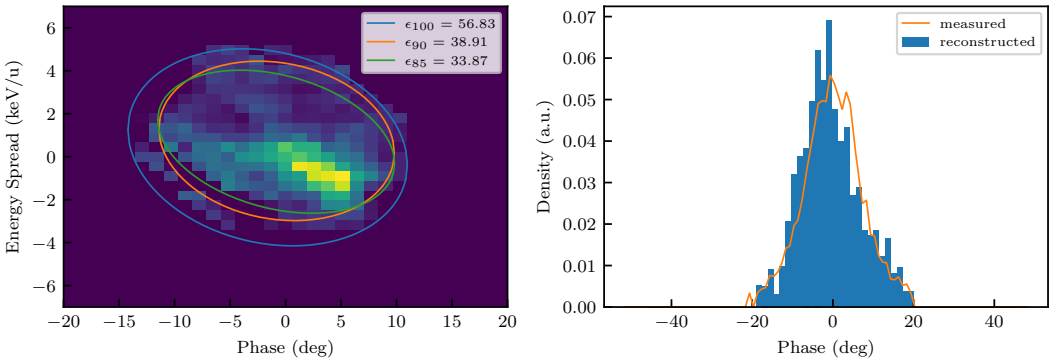

Figure 5.14: Reconstructed longitudinal particle density-distribution (*left*) using MENT algorithm with the same input as for Figure 5.12(b) and validation of the reconstruction with a dedicated, independent BSM (*right*) (HLI-IH control setting: 4.04 V, 110°, 28.05.2021, $R^2_{\text{train}} = 0.96$, $R^2_{\text{test}} = 0.95$).

However, a comparison of the bunch shape with the direct measurement shows, that the reconstruction accuracy is lower than with the NNLS algorithm (about $R^2 = 0.93$ vs. 0.96). This systematic effect is documented for all four reconstruction setups and detailed in Table 5.1.

The trend towards a smoother density-distribution with a slight loss of accuracy may be intentional for some purposes, and the preferred algorithm should be chosen to suit each particular application. For example, the assessment of the

[4] Additional results using MENT reconstruction method can be found in Figure A.1(a)–A.1(c) in Section A.1.2 on page 114.

Table 5.1: Comparison of regression scores of NNLS and MENT algorithm for different measurement series, i.e., different injector settings.

Dataset	$R^2_{\text{train,NNLS}}$	$R^2_{\text{train,MENT}}$	$R^2_{\text{test,NNLS}}$	$R^2_{\text{test,MENT}}$
Figure 5.12(a), Figure 5.14	0.95	0.89	0.94	0.92
Figure 5.12(b), Figure A.1(a)[1]	0.96	0.90	0.95	0.94
Figure 5.13(a), Figure A.1(b)[1]	0.95	0.90	0.86	0.77
Figure 5.13(b), Figure A.1(c)[1]	0.98	0.94	0.90	0.90

[1] see Section A.1.2 on page 114

longitudinal effective emittance is more reliable based on a MENT reconstruction but could also provide for a too low estimation of the total emittance.

5.3.7. Fast Injector Tuning

A dedicated procedure is developed in order to optimize the control parameters of the HLI-IH with assistance of only one Feschenko-BSM located behind the rebuncher, providing fast, low resolution beam profile measurements. For this, two rebuncher settings are used to measure the bunch length with the BSM:

Setting A: The rebuncher (GUCWBB14) is turned off

Setting B: The rebuncher provides for a parallel beam

Setting A is proportional to the energy spread: $\Delta\phi_{\text{BSM,A}} = \Delta\phi_0 + L\Delta W_0 \Rightarrow \Delta\phi_{\text{BSM,A}} \propto \Delta W_0$,
Setting B corresponds to the initial phase spread $\Delta\phi_0$ due to the longitudinally parallel beam transport: $\Delta\phi_{\text{BSM,B}} \propto \Delta\phi_0$.
Then, from both measured beam widths, a pseudo-emittance is calculated $\tilde{\epsilon} = \Delta\phi_{\text{BSM,A}} \cdot \Delta\phi_{\text{BSM,B}}$, which is used as a performance criterion to optimize the HLI-IH. With this criterion, the IH RF phase and amplitude, as well as matching rebunchers can be optimized for a minimum pseudo-emittance, taking the transmission and output energy into account.
This procedure has been benchmarked against another scenario, in which the beam width, which should be profiled with Setting B, was measured directly at the HLI output with the first BSM, eliminating efforts and uncertainties from controlling the rebuncher. Both methods are in sufficient agreement, as shown in Figure 5.15.
Furthermore, in Figure 5.12(b) the HLI-IH voltage and phase, optimized with the presented method, has been used. All other reconstructions indicate, that an optimum in beam quality possibly has been found.

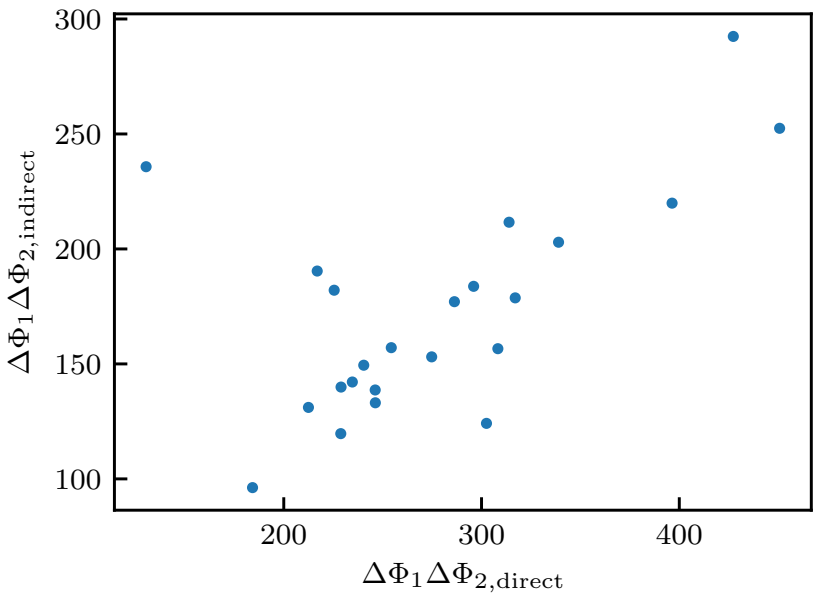

Figure 5.15: Comparison of pseudo-Emittance profiling using direct phase width measurements at the first BSM vs. indirect measurements of the phase width with a parallel beam setting at the second BSM.

5.4. Discussion

Sufficient measurement datasets have been obtained during several beamtimes in order to demonstrate the successful implementation of the reconstruction of the longitudinal bunch portrait. The first measurement campaign already provided high-quality results and first insights on the performance of the reconstruction method. The second campaign further validated the results of the NNLS method and provided more in-depth information about the quality of the HLI beam. An alternative method for on-the-fly injector tuning has been considered as well. Technical limitations, which impact the reconstruction performance, have been identified and resolved. In total, five reconstructions have been accomplished, comprising different number of measurements (from 10 to 100) as an input for the reconstruction. From now on, the beam matching to the superconducting CW Demonstrator and later to the future HELIAC can be addressed very detailed to achieve improved performance of the entire accelerator system.

6. HELIAC Injector Upgrade – Design of an Alternating Phase Focusing DTL Linac

6.1. Motivation

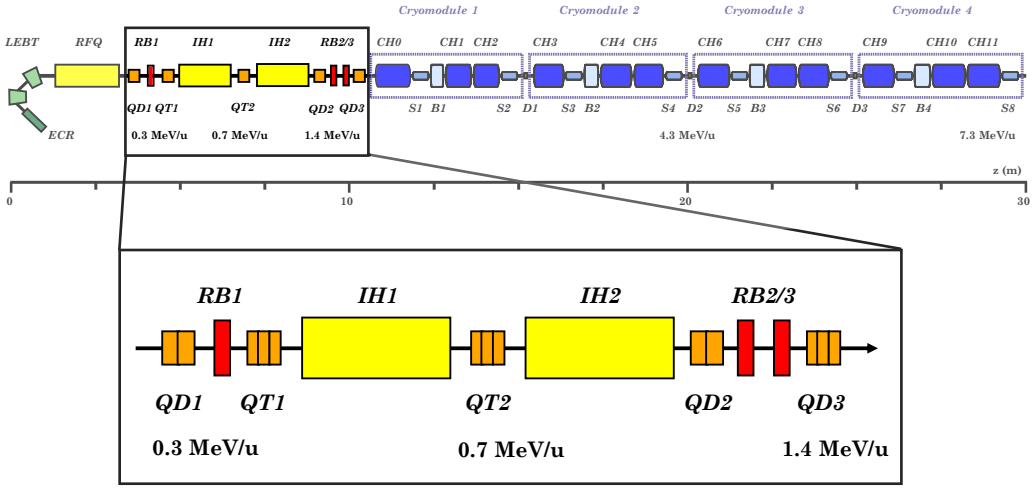

Figure 6.1: HELIAC beamline (see Section 1.4 on page 5) and the under design **N**ormal **C**onducting (NC) Injector linac as enlarged view. QD: Quadrupole Doublet, RB: Rebuncher, QT: Quadrupole Triplet, IH: APF IH Cavity

Initially, it was planned to upgrade the existing High Charge State Injector (**H**och**L**adungs**I**njektor, HLI) for CW capability to deliver beam to the SC HELIAC. The current construction strategy to build the HELIAC, however, allowed for a new design of the normal-conducting HELIAC injector section.
It is foreseen to provide for an entirely new beamline as new injector at GSI (see Figure 6.1). Since it is foreseen to use the GSI **S**tripper-**H**all (SH) SH1 and SH2 to setup this injector, new geometrical constraints have to be considered. This section expands on the paper *An Alternating Phase Focusing Injector for Heavy Ion Acceleration* [49].

As mentioned above, it was previously considered employing a CW capable version of the HLI injector [10] for the HELIAC. The HLI-IH cavity, employed in the injector, features an embedded beam dynamics concept to allow for a very compact accelerator layout, namely Combined Zero Degree Structure (**KO**mbinierte **NU**ll Grad **S**truktur, KONUS) (see Section 3.4 on page 38) [56]. During the HLI-IH operation using the embedded KONUS beam dynamics concept, the beam quality was found to be extremely sensitive to tank phase/voltage changes due to the high cavity compactness. However, redesigning the three KONUS sections inside the IH into three separate tanks for eased operation would unacceptably increase the total length of the linac section. A KONUS design with only two separate tanks could be difficult to realize because of transversally defocusing beam properties. Therefore, it was decided to construct two separate tanks with a different beam dynamics concept. As an alternative, an **A**lternating **P**hase **F**ocusing (APF) structure (see Section 3.5 on page 40) has been proposed to be applied in the HELIAC injector. Two independently powered and controlled IH DTL resonators were designed for the new HELIAC injector linac layout employing APF beam dynamics. The emerging intertank section has been configured with a quadrupole triplet and beam steerers, as well as additional beam diagnostic devices, in order to enable beam focusing and correction of the beam position as standard operation. This allows for eased beam commissioning and flexible and reliable future routine operation [47, 58, 122–124]. The modular design of the beamline components also improves maintenance, tuning, and reliable operation of the injector.

6.2. A New HELIAC Injector Linac

For the application of the APF cavities as HELIAC injector linac, the adjacent beamlines (see Table 6.1) are engineered to enable a space-efficient layout, as well as a precisely matched beam to the subsequent SC linac section. The frontend, comprising **E**lectron **C**yclotron **R**esonance **I**on **S**ource (ECRIS), **L**ow **E**nergy **B**eam **T**ransport (LEBT) and RFQ, delivers heavy ion beam to the APF section [125], as detailed in Table 6.2. The bunch orientation is horizontally convergent and vertically divergent ($x-x'$, $y-y'$) at a width of ± 2 mm and an angle of ± 20 mrad; longitudinally a canonical orientation on the phase plane is anticipated with an energy spread of ± 4 keV/u (about 1 %) and a beam length of $\pm 15°$. The NC APF DTL is split into five sections.

Table 6.1: APF injector sections

Element	Energy range (keV/u)
Medium **E**nergy **B**eam **T**ransport (MEBT)	300
IH Cavity-1	300–700
Intertank	700
IH Cavity-2	700–1400
Matching line to SC HELIAC	1400

Table 6.2: Design input beam parameters [125].

Property	Value
W_{kin}	300 keV/u
I_{beam}	$\leq$1 mA
Mass-to-charge ratio	6
Frequency	108.408 MHz
Horizontal Twiss parameters	
$\hat{\alpha}_x$	-1.228
$\hat{\beta}_x$	0.16 mm/mrad
$\hat{\epsilon}_x$	31.8 mm mrad
$\hat{\epsilon}_{x,\text{normalized}}$	0.81 mm mrad
Vertical Twiss parameters	
$\hat{\alpha}_y$	$+2.33$
$\hat{\beta}_y$	0.27 mm/mrad
$\hat{\epsilon}_y$	31.8 mm mrad
$\hat{\epsilon}_{y,\text{normalized}}$	0.81 mm mrad
Longitudinal Twiss parameters	
$\hat{\alpha}_z$	0
$\hat{\beta}_z$	4.46 deg/(keV/u)
$\hat{\epsilon}_z$	62 deg keV/u

The MEBT (behind the RFQ) is used as the matching section for APF Cavity-1. A first quadrupole doublet QD1 focuses the beam transversely, which initially diverges horizontally and converges vertically from the RFQ. The subsequent rebuncher RB1 provides for longitudinal matching to Cavity-1 at full particle transmission. The following quadrupole triplet QT1 completes the full 6D matching. Cavity-1 provides for beam acceleration from 300 keV/u to 700 keV/u. A quadrupole triplet QT2 located in the intertank section between the two APF cavities provides the required beam focusing to a transverse size of about 5 mm. In order to offer a compact layout, the intertank design does not include an additional rebuncher[1]. The energy gain of Cavity-2 is sufficient to provide for the design beam energy of 1400 keV/u. The following matching line is designed with two quadrupole duplets QD2/QD3 and two rebuncher cavities RB2/RB3. This section ensures full 6D beam matching to the superconducting HELIAC accelerator.

For the general installation of the HELIAC at the GSI facility, a space-saving design of the injector section is necessary. Thus, the beam transport sections (MEBT, intertank,

[1]The operation of an additional rebuncher in the intertank is not envisaged, as it would require an additional quadrupole triplet, which would increase the overall length to an impractical level.

matching section) must be compact and easy to operate. In particular, the limiting factors are the available rebuncher voltage and quadrupole field gradients, as a too narrow beam would not be sufficiently focused. Therefore, drift sections are inevitable to allow the bunch to spatially expand and thus enable for sufficient beam focusing in all directions.

6.3. APF Channel Design Methods

The synchronous phase (i.e., the RF phase when the reference particle is in the center of a gap) in each RF gap has to be adequately inferred when configuring the APF beam dynamics synchronous phase pattern for a DTL. From the perspective of beam dynamics, the primary objective involves finding the arrangement of the synchronous phases in order to attain the best beam energy gain together with a maximum transmission of the beam and a minimal beam emittance growth. The actual geometric layout of a DTL for an arbitrary arrangement of synchronous phases has to be calculated from Equation (3.62) on page 39.
Since the APF concept incorporates subsequent longitudinal and transverse non-linear RF beam focusing, it becomes crucial to employ a beam dynamics software, which is capable to account for the 6D-coupled equation of the particle's positions and velocities. Rapid simulations of the electromagnetic fields and the particle beam dynamics are required for each (of the numerous) cavity geometries. It has been decided to use the versatile DYNAMION [60] software package. One of the main strengths of this software is the derivation of the 3D electric RF fields of different DTLs with initially specified gap-voltages and a detailed geometric layout (including roundings and the inner/outer tube radius).
The choice of this software for beam dynamics offers a close cooperation with the RF designers, who provide for a realistic implementation of the cavity model in electromagnetic simulations (commonly employing CST-STUDIO SUITE [126]), from which the required realistic gap-voltage amplitudes $\vec{U}$ are calculated using a 3D electromagnetic eigenmode solver. The field amplitudes depend non-linearly on the cavity geometry and consequently on the synchronous phase pattern. Moreover, these advanced electromagnetic calculations allow the post-processing of key cavity characteristics for the whole DTL[2]. In an advanced calculation level and for final confirmation of the beam dynamics, it is possible to import the 3D electric field map from CST to DYNAMION as well.

As a rapid code for detailed reliable simulations is available to find the optimum synchronous phases ϕ_i in all RF gaps $\vec{\phi}$, a Monte-Carlo method is used as a global optimization procedure. For this purpose, $\vec{\phi}$ is optimized, whilst the search region is shrunk manually, until the objective function $f(\vec{\phi})$ (see Equation (6.2)) is minimal.

[2] e.g., power dissipation, peak fields, resonance frequency, etc.

To provide the emittance growth with the utmost sensitivity, the size of the smallest enclosing ellipse surrounding 100 % of the particle ensemble $\hat{\epsilon}_{100\%}$ is used to calculate the total emittance growth, denoted as ξ:

$$\xi = \frac{\hat{\epsilon}_{100\%,\mathrm{out}}}{\hat{\epsilon}_{100\%,\mathrm{in}}}. \tag{6.1}$$

The objective function takes the emittance growth ξ_z and $\xi_{x,y}$ in all three main phase planes into account, as well as the mean final kinetic output energy W_{out} of the cavity to be designed. To account for asymmetric input beams in both transverse phase planes and to limit the emittance growth evenly, only the maximum emittance growth of the two planes is considered $\xi_{x,y} = \max(\xi_x, \xi_y)$. Thus, the objective function is composed of three terms assessing the output energy and the increase in longitudinal and transverse emittance:

$$f(\vec{\phi}) = \left(\frac{\xi_{x,y} - 1}{t_{x,y}}\right)^2 + \left(\frac{\xi_z - 1}{t_z}\right)^2 + \frac{W_{\mathrm{target}} - W_{\mathrm{out}}}{t_{\mathrm{E}}}. \tag{6.2}$$

The term of the power function related to beam energy is on purpose left unsquared in order to differentiate lower and higher beam energies from the target energy W_{target}. This way, in case the increase in beam emittance remains moderate, a higher final energy is preferred by the objective function.
Originally, the peak transverse beam size within a cavity was considered as an objective measure. However, since the emittance growth ξ is connected closely to the beam width, the width is thus indirectly considered. The beam size itself is omitted as an objective in favor of a less complex performance function. Still, a virtual aperture could be introduced when executing the software, in order to ignore all simulations with virtual losses. It has been decided to give preference to a smaller longitudinal emittance growth over transverse emittance. In general, a too high beam width from a high beam emittance could be readily scraped transversely, whereas it would require a more sophisticated dispersion section to eliminate particles from the longitudinal halo.
Hence, the longitudinal tolerance parameter is selected as $t_z = 0.5\,\%$ and the transverse tolerance is selected twice as high: $t_{x,y} = 1\,\%$. The output beam, energy tolerance is chosen as $t_{\mathrm{E}} = 50\,\mathrm{keV/u}$, whereas the desired output energy W_{target} varies for different cavities.

The objective function takes into account the requirements for the linac beam dynamics, i.e., limiting the emittance growth and a maximum energy gain of the beam, and indirectly the transverse and longitudinal focusing of the beam. The Monte-Carlo search region for $\vec{\phi}$ in each gap is limited by $\vec{\phi}_{\mathrm{min}}$ and $\vec{\phi}_{\mathrm{max}}$, which are manually reduced iteratively, allowing accurate control of the convergence at each level of design. Along with convergence of the synchronous phases (which impacts the drift tube geometric layout), the voltage pattern $\vec{U}$ has been updated in line with the latest design of the CST model.

A dedicated software was developed[3], that speeds up the global optimization procedure of the cavities phase layout by taking advantage of a concurrent multicore execution of the beam dynamics package DYNAMION. Thus, the adoption of a Monte-Carlo approach enables preforming parallel computations since individual simulations can be run independently of another. The application furthermore manages and displays progress and status of those multiple simulations and enables parallel execution[4], post-processing and logging. In addition, each simulation and the corresponding post-processes can be stored for subsequent in-depth studies.

In summary, the design method comprises the following tasks:

Algorithm 3: General APF optimization procedure

Data: Voltage $\vec{U}$ in each gap[5], search boundaries $\vec{\phi}_{\text{min}}$ and $\vec{\phi}_{\text{max}}$, target objective function f_{target}

Initialize $f_{\text{tmp}} = \infty$

while $f_{\text{target}} < f_{tmp}$ **do**

- Generation of random array of phases $\vec{\phi}$ subject to $\vec{\phi}_{\text{min}} < \vec{\phi} < \vec{\phi}_{\text{max}}$
- Generation of cavity geometry to yield above phases using Equation (3.62)
- Calculation of electrical field shape (scaled by $\vec{U}$)
- Calculation of beam dynamics
- Calculation of performance factor $f_{\text{tmp}} = f(\vec{\phi})$ (see Equation (6.2))

$f_{\text{min}} = f_{\text{tmp}}$

Result: Optimal synchronous phases $\vec{\phi}$, corresponding objective value f_{min}

Algorithm 3 provides the best possible cavity design with respect to the objective function $f(\vec{\phi})$ (see Equation (6.2)) and is supposed to yield low overall emittance growth ξ. Furthermore, only such geometries that reached the full transmission are included for any further evaluation.

[3] S. Lauber, internal GSI report 2021

[4] The hardware currently used allows for 64 threads per machine.

[5] e.g., based on a realistic model from CST

6.4. Reference Beam Dynamics

6.4.1. APF Cavity-1

Cavity-1 is the foremost crucial section of the overall beam channel configuration in terms of the objective function $f(\vec{\phi})$. Within this cavity, the particle bunches are accelerated from an input beam energy of 300 keV/u with an accelerating gradient of 3 MV/m to a final energy of 1.4 MeV/u. Within this region of beam energy, the bunches are very sensitive to non-linear field components, which usually leads to an increased beam emittance. The design of Cavity-1 was carried out with special diligence to find a layout with low emittance growth, especially in the longitudinal phase plane. The final geometrical and beam dynamics properties of the cavity are depicted in Table 6.3 and 6.4.

Table 6.3: Cavity-1 design parameters

Tank frequency f	108.408 MHz
Acceleration gradient E_0	3.0 MV/m
Input energy	300.0 keV/u
Output energy	700 keV/u
Length (inner wall to wall)	1.3 m
Number of gaps	29
Aperture radius r_a	9 mm

Table 6.4: Beam parameters at Cavity-1

Twiss matching parameters	Input	Output
$\hat{\alpha}_{x,y}$	0.89	−2.1
$\hat{\beta}_{x,y}$	0.55 mm/mrad	1.6 mm/mrad
$\hat{\alpha}_z$	−0.03	−0.7
$\hat{\beta}_z$	4.63 deg/(keV/u)	2.4 deg/(keV/u)
Emittance growth	$\xi_{100\%}$	$\xi_{90\%}$
horizontal/vertical (normalized)[1]	5.0 %	3.5 %
longitudinal	8.0 %	1.3 %

[1]The input emittances and beam transport is identical in both planes.

After first draft design studies, it was decided to adopt a transition beam energy from Cavity-1 to Cavity-2 of 700 keV/u. This yields a beam acceleration of 400 keV/u for Cavity-1 and 700 keV/u in Cavity-2. A higher transition energy would require a higher acceleration within Cavity-1 and decrease the beam quality, whereas a lower

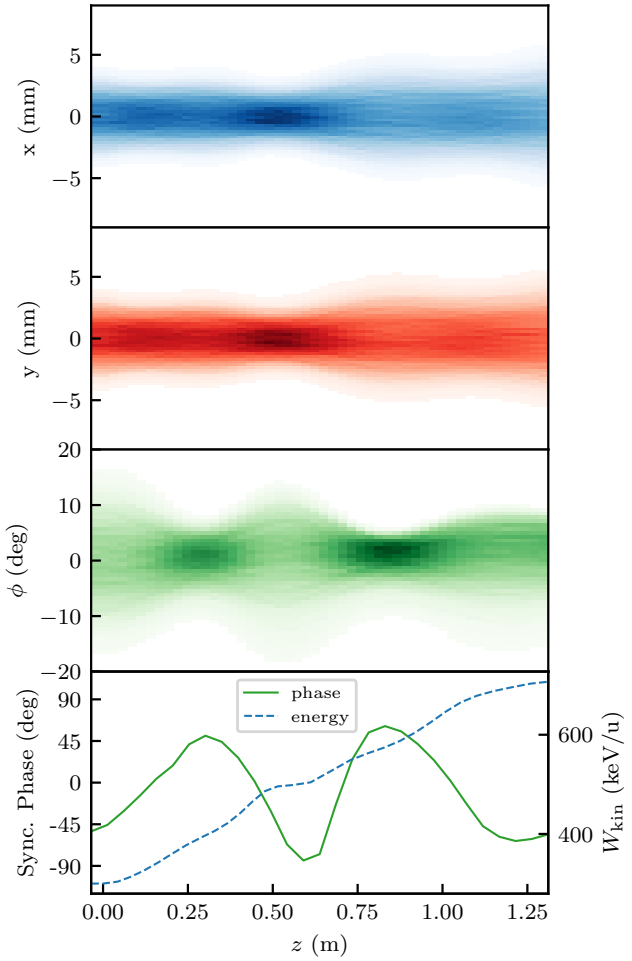

Figure 6.2: Density-coded particle trajectories along the first tank Cavity-1 in the three main phase planes, as well as the corresponding synchronous phase and mean beam energy.

transition energy leads to an impracticable length of Cavity-2 in order to achieve the necessary acceleration within this cavity.

To meet the target phases in each gap, the length between two gap centers has to be varied, i.e., the cell-length. The cell-length can be changed by both, the gap- and the tube-length. The gap-lengths were frozen in the early design phase to keep the surface field of the tubes below the Kilpatrick criterion of 2.5 and to minimize their thermal load. Accordingly, only the tube-lengths are allowed to be modified to change the cell-lengths and thereby the synchronous phases.

In addition, a lower limit of about 17 mm has been set for the tube-lengths in order to prevent tube lengths that are too short. Short tubes do not shield the field components properly from the stems and could introduce a distortion of the electric field. Also,

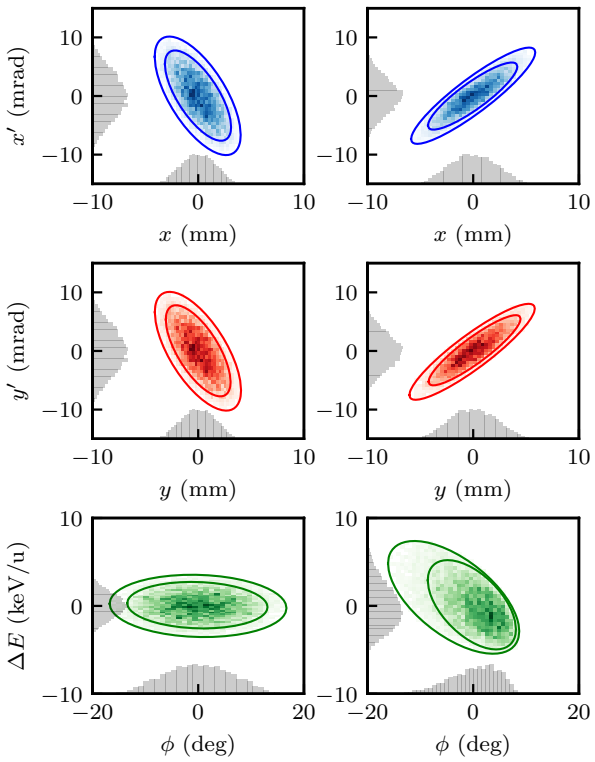

Figure 6.3: Design particle distribution for Cavity-1: input (*left*) and output (*right*); the smallest ellipses enclose 90 % and 100 % of all particles, the color depths encode the particle density.

the thermal load at too short tubes is insufficiently high, and their fabrication is more complicated.

After application of the optimization algorithm for Cavity-1, a semi-sinusoidal phase pattern is obtained (see Figure 6.2), which is a frequently mentioned synchronous phase pattern for APF accelerators [95, 99, 100].

A beam spot of below two-thirds of the cavity aperture is obtained, taking into account the maximum beam spot along the cavity. For the optimization of Cavity-1 usual Twiss parameters have been used as input. Thus, a transverse beam spot size of about ±4 mm (±10 mrad) and a bunch length of about ±16° (±4 keV/u) are used as matching parameter for Cavity-1 (see Figure 6.3). A 6D-Waterbag distribution (see Section 3.1 on page 28) filled with 10 k macro particles is assumed as input distribution. The transverse beam orientation at the cavity exit were unconstrained during design, as the beam is subsequently matched to the second cavity with a quadrupole triplet in the intertank section.

A small bunch length is necessary as input for Cavity-2 for efficient acceleration. But as there is no rebuncher in the intertank, the longitudinal output of Cavity-1

is constrained to deliver the smallest possible bunch length to Cavity-2. Thus, the fringe gaps of Cavity-1 are utilized for longitudinal beam matching to yield a ±20° wide beam by employing a synchronous phase of about 50° in the last gaps of Cavity-1. This is possible because, compared to the first gaps, the last gaps do not inflict effects on the beam dynamics, which are accumulated until the exit of Cavity-1. The last gaps only affect output beam orientation. Also, the beam dynamics layout of Cavity-2 is less challenging in terms of minimizing emittance growth due to a higher kinetic energy and corresponding beam rigidity, thus there is a margin to select the output beam parameters of Cavity-1.
The results of the beam dynamics calculation have been validated by using two independently developed software packages (DYNAMION and an in-house developed code[6]). The particle traces are consistent with high accuracy (about 1 % relative difference) between both solvers. Advanced particle tracking simulation were performed with the most realistic electromagnetic field available, imported from the actual cavity geometry (considering the geometry of tubes, stems, etc.) calculated by CST. It could be shown, that steering effects from the stem's dipole component of the stems, described in Section 6.4.4, is below 1 mrad.
The longitudinal total emittance growth within Cavity-1 is $\xi_z = 8\,\%$ and the transverse normalized total emittance growth is $\xi_{x,y} = 5\,\%$ (see Figure 6.3). The increase of total emittance, especially in the longitudinal component, occurs mostly as a halo due to non-linear 6D coupling of the evolution of particles velocity and coordinates by the acceleration field. Considering only 90 % of the particle ensemble, the growth of effective emittance is transversely 3.5 % and longitudinally 1.5 %.

6.4.2. Intertank section

The intertank section links Cavity-1 and Cavity-2. The quadrupole triplet, which is located in the intertank section, refocuses the beam transversely with a focal point at the center of Cavity-2. This concentrates the design of Cavity-2 on acceleration, with transverse focusing only as a secondary priority. Furthermore, beam diagnostics and beam steerers will ease operation of the second cavity.
In order to start the design of Cavity-2, its input Twiss parameters must be fixed. As there is no rebuncher in the intertank, the longitudinal beam matching is affected only by the intertank length. Therefore, this length is to be set in advance to start with Cavity-2 design.
The 1.5 m long intertank section is designed with minimum equipment: a quadrupole triplet, two beam steerers, two **B**eam **P**osition **M**onitors (BPMs) and a standard vacuum section valve (see Figure 6.4).

[6] S. Lauber, internal GSI report 2021

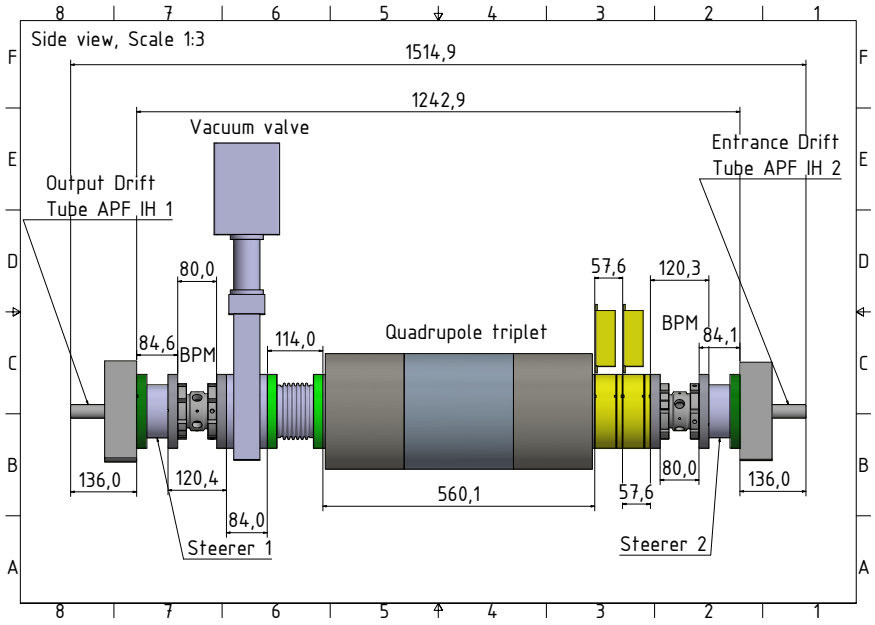

Figure 6.4: CAD drawing of the intertank section between Cavity-1 and Cavity-2 (all lengths in mm).

Preliminary efforts towards a single cavity layout for acceleration from 300 keV/u to 1.4 MeV/u without intertank have been made (see Section A.2.1 on page 116) but were discarded due to multiple reasons:

- The manufacturing, copper-plating and mounting of one long tank.
- Accumulation of phase errors in a first cavity could be mitigated by a second cavity, but not within one tank.
- A lower tolerance to synchronous phase deviations due to manufacturing errors and misalignment.
- Degradation of beam quality due to steering dipole components of the stems.
- Missing beam instrumentation for commissioning and routine operation.
- Necessity for a sufficient high-power amplifier.

For these reasons, it has been decided to employ two independent cavities, offering for two separate power supplies and phase controls. The accumulation of synchronous phase deviations (due to manufacturing errors) is partially suppressed, as the second phase control mitigates the phase deviations at the entrance of the second cavity.
While the beamline has to be operated with different ion species and mass-to-charge ratios, the beam parameters delivered by the frontend system are variable. Thus, the beam steerers and quadrupole magnets provide for the necessary adaptability with variable beam parameters allowing consistent beam matching to the cavity acceptance and for a robust setup for routine CW operation.

6.4.3. APF Cavity-2

While the average beam energy in Cavity-2 and consequently the beam rigidity (0.9 T m) is twice as high as in Cavity-1, the layout of the second cavity is mainly focused on the highest possible acceleration gradient, as the bunch shape is less deformable and consequently the beam dynamics layout is resistant to effective emittance growth. The principal design values are depicted in Table 6.5. With rising beam energy, the cell-length increases as well. Moreover, due to the dedicated APF feature of synchronous phase variation, occasionally even disproportional long cell- and tube-lengths could be the result. The optimization was constrained to generate only cell-lengths below 80 mm to avoid undesired heating effects and synchronous phase instabilities. The edges of the tubes are located too far from the stem in long cells, preventing effective heat transport. Also, the time to pass a tube scales with the phase mismatch in the adjacent gap, when the reference energy is not exactly achieved, and thus too long gaps are not favorable. As a consequence, the synchronous phase pattern in Cavity-2 (see Figure 6.5) varies significantly from those of Cavity-1.

Table 6.5: Cavity-2 design parameters

Tank frequency f	108.408 MHz
Acceleration gradient E_0	3.1 MV/m
Input energy	700 keV/u
Output energy	1.4 MeV/u
Length (inner wall to wall)	1.8 m
Number of gaps	27
Aperture radius r_a	9 mm

Table 6.6: Beam parameters at Cavity-2

Twiss parameters	Input	Output
$\hat{\alpha}_{x,y}$	1.7	−1.4
$\hat{\beta}_{x,y}$	1.2 mm/mrad	3.2 mm/mrad
$\hat{\alpha}_z$	1.31	2.1
$\hat{\beta}_z$	4.27 deg/(keV/u)	1.6 deg/(keV/u)
Emittance growth	$\xi_{100\%}$	$\xi_{90\%}$
horizontal/vertical (normalized)	2.7 %	0.0 %
longitudinal	1.9 %	0.0 %

[1]The input emittances and beam transport is identical in both planes.

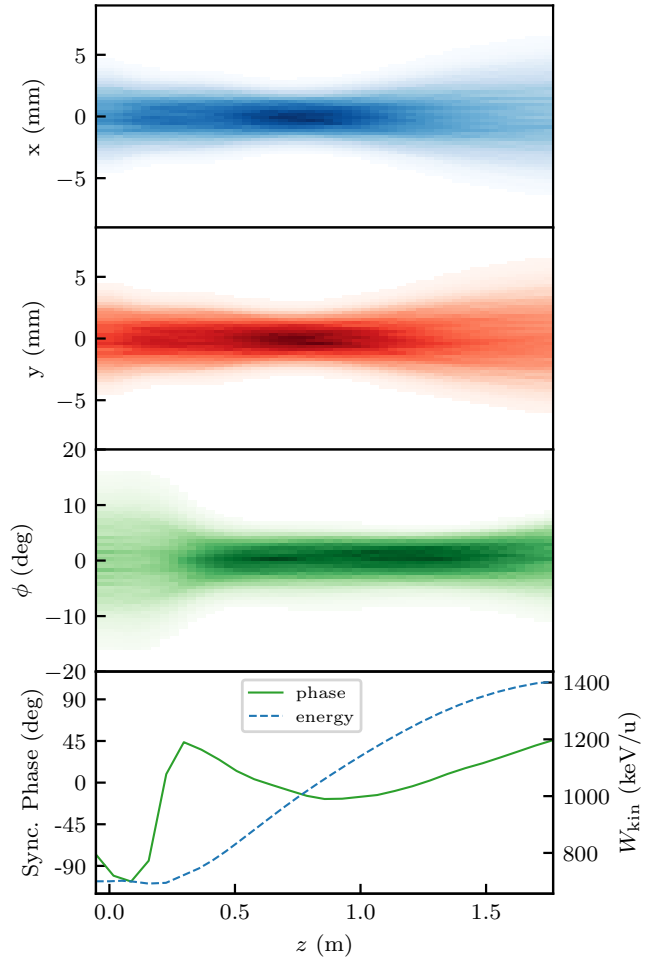

Figure 6.5: Density-coded particle trajectories along the first tank Cavity-1 in the three main phase planes, as well as the corresponding synchronous phase and mean beam energy.

The phases around −90° within the first 0.5 m of Cavity-2 refocus the longitudinally divergent beam and form a narrow bunch length below 10°.

A well visible rapid phase-jump from negative to positive phases is obtained, which accounts for the longitudinal diverging input bunch orientation (whereas the longitudinal input to Cavity-1 is in canonical orientation, see Table 6.6). The beam is refocused to a low phase width of below 10°. The jump to positive phases defocuses the beam slightly in order to make the beam longitudinally almost parallel.

After the rapid phase-jump, the beam is efficiently accelerated employing phases around 0°, while at any time the transverse beam size is below two-third of the aperture. The synchronous phases follow a parabolic pattern (potentially part of a semi-sinusoidal pattern) around 0°, in order to provide for the required energy

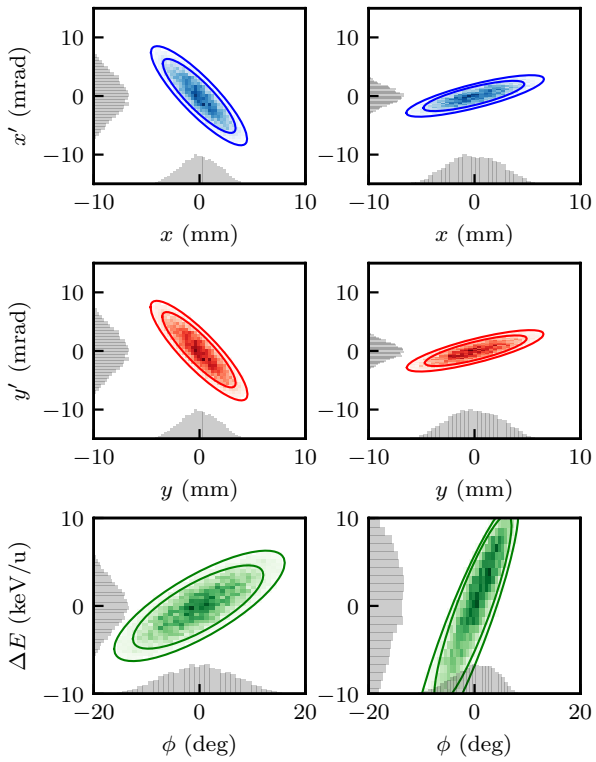

Figure 6.6: Design particle distribution for Cavity-2: input (*left*) and output (*right*); the smallest ellipses enclose 90 % and 100 % of all particles, the color depths encode the particle density.

gain of 700 keV/u. The last gaps apply positive synchronous phases up to the end of the cavity, providing for the necessary transverse focusing and also longitudinal defocusing, which is especially essential to allow for a position of the following rebuncher as close as possible to the cavity exit, resulting in a compact matching line. Most efficient rebunching is achieved by obtaining a bunch length of 30° at the rebuncher cavity.

An unexpected empirical finding from the optimization of Cavity-2 is the occurrence of a synchronous phase of −110° in the second gap. This is exceptional, as phases below −90° inflict deceleration of the particle ensemble. However, the overall change of energy in the second gap is low compared to the gaps in the center of the cavity due to the low effective voltage ($U_{\mathrm{eff}} = T_{\mathrm{TTF}} \cdot 130\,\mathrm{kV} \cdot \cos(-110°)$ vs. $T_{\mathrm{TTF}} \cdot 270\,\mathrm{kV} \cdot \cos(0°)$), thus the effect of deceleration is not significant. Multiple iterations with a limited search space to standard ±90° have resulted in an insufficient emittance growth compared to the presented results.

The occurrence of a synchronous phase of $-110°$ can be explained by taking into account its neighboring gap of $-70°$ synchronous phase. The energy gain ΔW in a given gap is proportional to $\cos(\phi_i)$. Two gaps may yield an energy gain of

$$\Delta W \propto \cos(\phi_i) + \cos(\phi_{i+1}). \tag{6.3}$$

By expressing both phases ($-110°$ and $-70°$) as $-90° + \Lambda$ and $-90° - \Lambda$, using $\Lambda = 20°$ and considering particles in the vicinity $\delta\phi$, Equation (6.3) is rewritten as

$$\Delta W \propto \cos(-90° + \delta\phi - \Lambda) + \cos(-90° + \delta\phi + \Lambda). \tag{6.4}$$

$$\Delta W \propto \sin(\delta\phi - \Lambda) + \sin(\delta\phi + \Lambda). \tag{6.5}$$

By applying the addition theorem $\sin(\alpha + \beta) + \sin(\alpha - \beta) = 2\sin(\alpha)\cos(\beta)$, Equation (6.5) can be expressed as

$$\Delta W \propto 2 \cdot \sin(\delta\phi) \cdot \cos(\Lambda). \tag{6.6}$$

Thus, particle coordinates in the vicinity $\delta\phi$ will be transformed almost linearly in accordance with $\sin(\delta\phi) \approx \delta\phi$ with a less effective focusing gradient of $\cos(\Lambda = 20°) \approx 94\,\%$ of an ideal, linear lens operated at $-90°$.
With this method, the overall linear focusing strength of the first gaps are adjusted. The strength cannot be changed by the gap-voltages, as they are fixed by the overall geometric layout. Thus, the bunch is moderately focused and well suited for further transport through the cavity. Furthermore, a smoother transition from negative to positive phases is achieved (compared to a $-90°$, $-90°$, $10°$ layout). This is also favored for the cavity design, because thereby too long tube-lengths are prevented during transition to positive phases.

The longitudinal emittance growth is mainly driven by a fraction of particles being stretched away from the center of the bunch, resulting in a beam halo. Generally, a complicated shape of the particle ensemble has been anticipated. But the mostly elliptical shape of particle distribution eases the beam matching to the SC section of HELIAC, since the effective longitudinal emittance is low.

6.4.4. Beam steering

The alternating arrangement of the stems (extending from the girders and holding the tubes, see Figure 2.3 on page 17) on both sides of the IH cavity shell girder leads to an asymmetry of the cavity geometry, which induces a dipole component from the stems in the RF electric gap field and eventually deflects the beam from the reference axis of the DTL cavity. Therefore, both cavities are examined for possible beam steering effects. In order to provide for a realistic beam dynamics cavity design, the 3D electromagnetic RF field was ported from CST to DYNAMION.
Particle tracking simulations have been carried out to investigate the influence of the electric dipole components from the stems on the reference particle. The resulting

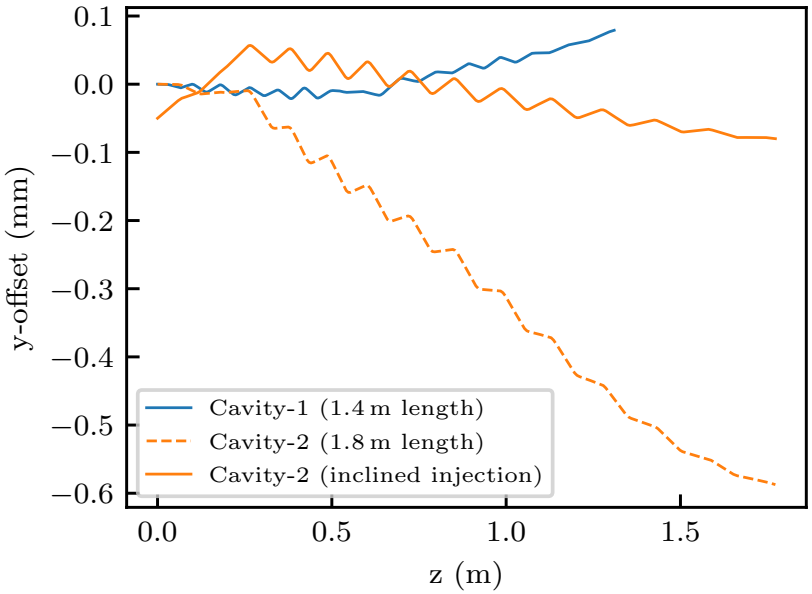

Figure 6.7: Impact of dipole component of the stems on the reference particle in Cavity-1 and Cavity-2.

particle trajectories are depicted in Figure 6.7. The overall dipole component in Cavity-1 causes a sufficiently low displacement of the reference particle of 0.1 mm and 0.16 mrad at the exit of the cavity. The particle tracking in Cavity-2 yields a larger displacement of 0.6 mm and −0.15 mrad, which can be mitigated by injecting an inclined beam (0.05 mm offset and 0.45 mrad angle) by using the intertank beam steerers. By providing for an inclined injection, the beam displacement remains below 0.1 mm with an angle 0.06 mrad.
Thus, considering the dipole component of the stems, the design using independent cavities and the intertank demonstrates already the advantage for reliable routine linac operation.

6.4.5. End-to-End Simulations

The final injector linac layout for the HELIAC and the results of corresponding end-to-end beam dynamics particle tracking simulations are presented in Figure 6.8 The Twiss input parameters for the entire designed accelerating focusing channel are depicted in Table 6.2. Following the RFQ output, the MEBT provides for beam matching to Cavity-1 acceptance within 1.8 m section length. The Matching Line, linking Cavity-2 with the SC HELIAC, is 3.5 m long and provides for flexible matching as well, by use of two rebuncher cavities, one quadrupole triplet and one quadrupole doublet.
In the MEBT, an inevitable source of beam emittance growth is the rebuncher RB1, which slightly deforms the bunch shape. Furthermore, Cavity-1 induces additional deformation of the longitudinal emittance, while for the design of Cavity-2 an elliptic

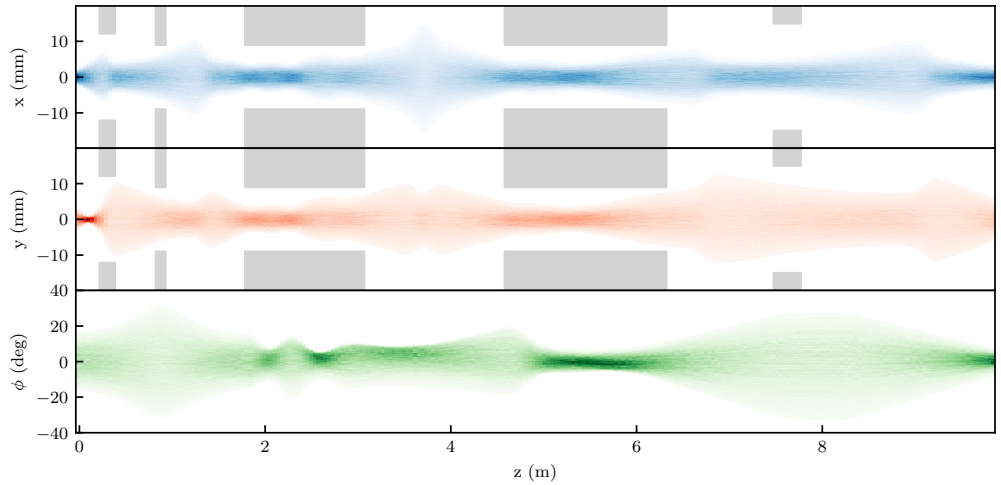

Figure 6.8: End to end simulation of the whole channel from RFQ output to SC CH input. The particle density is encoded as intensity of color. The matching sections to the IH ($z \leq 1.8\,\mathrm{m}$) and to the SC CH ($z \geq 6.2\,\mathrm{m}$) are included.

bunch shape has been assumed originally. Finally, these effects have additional impact on the overall emittance growth. Nevertheless, as Cavity-2 is relatively robust to such changes, full beam transmission and a high beam brilliance are delivered as output (see Table 6.7). The transport line following to Cavity-2 is used for beam matching to the SC HELIAC section.
The simulation results of the above-mentioned end-to-end simulation yield 100 % particle transmission, as intended and obtained during the prior design stages. Along the whole section the total emittance growth $\xi_{100\%}$ is sufficiently low with about 20 % increase of the total emittance in all three phase planes (see Table 6.7). The effective emittance growth considering 90 % of the particles is $\xi_{90\%} \leq 5\,\%$.
The total length (4.5 m) comprising both cavities and intertank section is about 25 % longer compared to the HLI KONUS-IH linac. It must be taken into account, that the APF linac provides for additional dedicated beam transport- and diagnostics equipment in the intertank section, essential for commissioning and routine CW operation of the entire HELIAC.

6.4.6. Beam Dynamics Error Studies

The influence of uncertainty factors that occur during manufacturing, installation, and operation of the two cavities was investigated.
In Table 6.8 the quantities of interest are depicted. The tube-center is subject to variation because the tubes are installed with finite accuracy in the tank and thus influence the neighboring gap-lengths. Due to manufacturing, the tubes are going to be produced with limited accuracy, inflicting deviations from the designed tube-length and consequently the neighboring gap-lengths are influenced. Furthermore,

Table 6.7: IH-APF final beam dynamics design parameters

Beam transmission	100 %	
Input beam energy $W_{\text{kin, in}}$	300 keV/u	
Output beam energy $W_{\text{kin, out}}$	1.4 MeV/u	
Mean beam spot radius	4 mm	
Max beam spot radius	7 mm	
Aperture radius	9 mm	
Aperture rounding	2 mm	
Emittance growth	$\xi_{100\%}$	$\xi_{90\%}$
x, y (normalized)	23.0 %	5.0 %
z	17.0 %	3.0 %

Table 6.8: Error assumptions for perturbation analysis

Variable	Standard deviation σ
Tube center	±200 µm
Tube length	±100 µm
Gap voltage	±2.0 %
Cavity voltage	±0.2 %
Cavity phase	±0.2°

the alignment of the tubes and the limited precision of the CST eigenmode calculations impacts the accuracy of the gap-voltage. The coupling behavior of the cavity geometry to the gap-voltages could be reproduced using eigenmode calculations, but it is time-consuming to be sufficiently calculated along with thousands of beam dynamics simulations. Thus, the quantities are investigated independently [94]. Lastly, the influence of the RF phase and amplitude errors on the beam dynamics has been investigated. Both are subject to deviations and might be coupled as well, but the coupling behavior of the future RF supply is currently unknown. Thus, both quantities are considered independently as well.

For the following analysis, the uncertainty values are introduced to each simulation run by randomly sampling a deviation from a Gaussian distribution with standard deviation σ, with each gap and tube being altered by its own random deviation.

In Figure 6.9 the influence of each uncertainty quantity on the total beam emittance is depicted. Finally, an analysis, combining the different sources of uncertainty into one simulation run, is presented. Each histogram is generated from about 4000 simulation runs to provide for reasonable statistics.

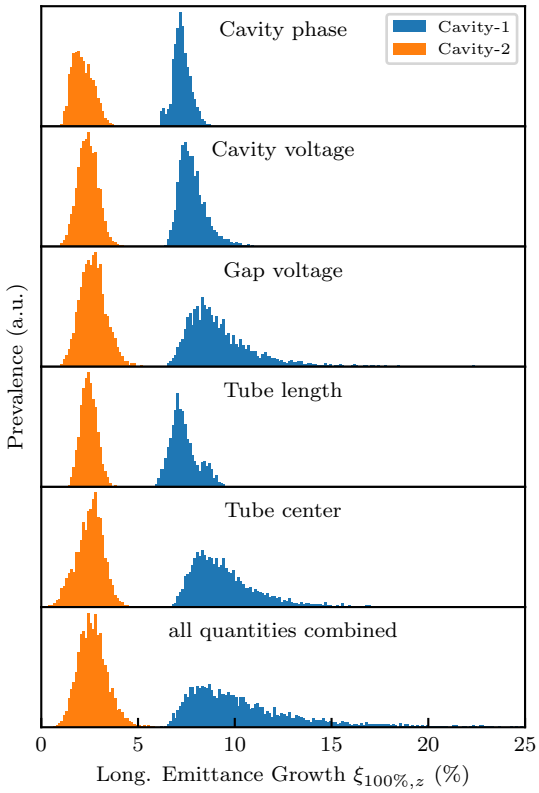

Figure 6.9: Perturbation influence on total longitudinal emittance growth $\xi_{100\%}$ ($\approx$ 4000 simulations per histogram).

For Cavity-1, the impact of the cavity-phase and voltage, as well as of the tube-length, is low. Nine from ten of those simulation runs yield an emittance growth ξ_z below 9 %. The median and the corresponding median standard deviation are $\xi_z = 7.0 \pm 0.4$ % for the three quantities mentioned above.

The gap-voltage and tube-center uncertainty analysis reveals a higher impact on total emittance growth. Nine from ten simulations results in $\xi_z \leq 12$ % and the median is $\xi_z = 9 \pm 1$ %, which is 2 % higher than for the previous group of uncertainty quantities.

For the combined simulation runs, where the different deviations are introduced simultaneously, nine from ten simulations yield $\xi_z \leq 15$ % with a median of $\xi_z = 10 \pm 2$ %.

All simulations runs for Cavity-2 result in an emittance growth below 5 %, demonstrating again the robust layout of this cavity.

Thus, the key quantities influencing beam quality are identified and will be considered during manufacturing of the cavities. The specification of the tubes requires an accuracy of at least 100 millimeters, and special care is taken during tube assembly to minimize deviation from the nominal voltage. Furthermore, the effective emittance growth $\xi_{90\%}$ is negligibly low (about 1 %) for all above-mentioned uncertainty quantities, hence a sufficiently high beam quality is expected.

6.4.7. RF & Thermal Cavity Layout

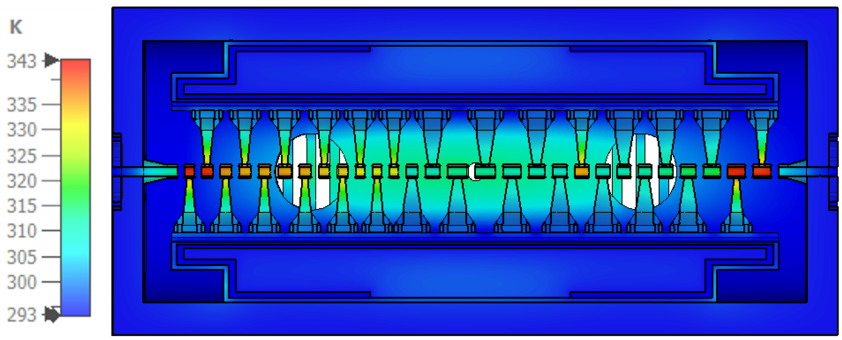

Figure 6.10: Surface temperature inside Cavity-1 [127]

The overall design of the cavity geometry, considering thermal and further RF properties, has been prepared by M. Basten. A detailed overview is published in [127]. However, the constraints from the RF and thermal cavity development have to be accounted for during beam dynamics design and vice versa.
As mentioned in previous chapters, the tube and gap-lengths influence the heat distribution along the cavity (see Figure 6.10), but also directly influence beam transport and quality. Thus, the tube and gap-lengths were carefully selected within boundaries suitable to be sufficiently cooled by the embedded cooling system of the cavity. When the edges of long tubes are too far from the stem, they cannot be sufficiently cooled, and tubes too short yield an adverse ratio of heat per unit length.
As already presented, changes of the voltage per gap can induce emittance growth. Thus, the tuning concept of the cavity has been carefully designed to mitigate this effect by using an additional tuner. A dedicated analysis of the tuner dimensions and positions has been carried out. During routine tuner operation, the voltage deviation is predicted to remain below 2 %.

Table 6.9: RF parameters of Cavity-1 and Cavity-2 [49, 127]

Property	Cavity-1	Cavity-2
Design frequency	108.408 MHz	108.408 MHz
Number of gaps	29	27
Effective length L_{eff}	1.31 m	1.75 m
Length (physical length)	1.5 m	2.0 m
Electric peak field E_{Peak}	2.5 Kilpatrick	2.5 Kilpatrick
Length (inner wall-to-wall)	1.405 m	1.852 m
RF power (100 % duty cycle)	20 kW	35 kW
Quality factor Q_0	19000	23000
Shunt impedance Z_0	690 MΩ/m	500 MΩ/m
Effective shunt impedance Z_{eff}	530 MΩ/m	400 MΩ/m
Max. temperature	$\approx$ 360 K	$\approx$ 360 K
Accelerating gradient	3.0 MV/m	3.1 MV/m
Effective accelerating gradient	2.614 MV/m	2.810 MV/m
Drift-tube aperture radius r_a	9 mm	9 mm
Drift-tube outer radius	18 mm	18 mm
Drift-tube rounding	2 mm	2 mm

6.5. Discussion

A CW heavy ion linear accelerator with two separately powered IH resonators, linked by an intertank section featuring a quadrupole triplet, has been developed by applying the APF beam dynamics scheme. This scheme avoids the need for magnetic quadrupoles inside a cavity. The newly proposed acceleration/focusing scheme was elaborated by design and optimization of the synchronous phase pattern, and correspondingly the cavity geometry parameters, using the Monte-Carlo method. Hence, a dedicated phase pattern for beam matching and acceleration with two cavities has been investigated, allowing compact matching sections adjacent to the cavities. The total beam emittance growth within the cavities is adequately small (less than 5 %) in all three main phase planes. Moreover, the cavities are found to cause negligible beam displacement (below 500 µm and 0.2 mrad). The RF properties were concurrently simulated, and the cavity geometry was additionally designed to mitigate thermal load. The advanced APF section design, comprising two cavities, eases commission, maintenance, operation, and possible future upgrades. The APF DTL cavities will be used as DTL section for the room temperature CW heavy ion injector linac for the HELIAC.

7. Instrumentation & Commissioning

7.1. Motivation

The first cryomodule of the HELIAC is going to be commissioned as part of the Advanced Demonstrator project (see Figure 1.4 on page 8) in 2022. The cryomodule will be equipped with four SC short CH cavities, a cold BPM and two SC solenoids. In preparation of the beamline for this project milestone, the positions of the quadrupoles were changed to improve beam matching. It is foreseen to utilize a pencil beam in order to recommission the beamline and to further investigate the cryomodule, among others to monitor and mitigate beam displacement effects generated by individual resonators and to provide for beam-based alignment of dedicated cryomodule components. In order to provide for a pencil beam, a collimation system is required (see Figure 7.1), that reduces the beam spot and the beam divergence so that the beam diameter along the cryomodule is as compact as possible, whilst remaining detectable with beam profile grids. An advanced collimation system has been designed and commissioned in the context of this thesis. Results of the successful measurement campaign are presented in this chapter. This section expands on the paper *A Dynamic Collimation and Alignment System for the Helmholtz Linear Accelerator* [48].

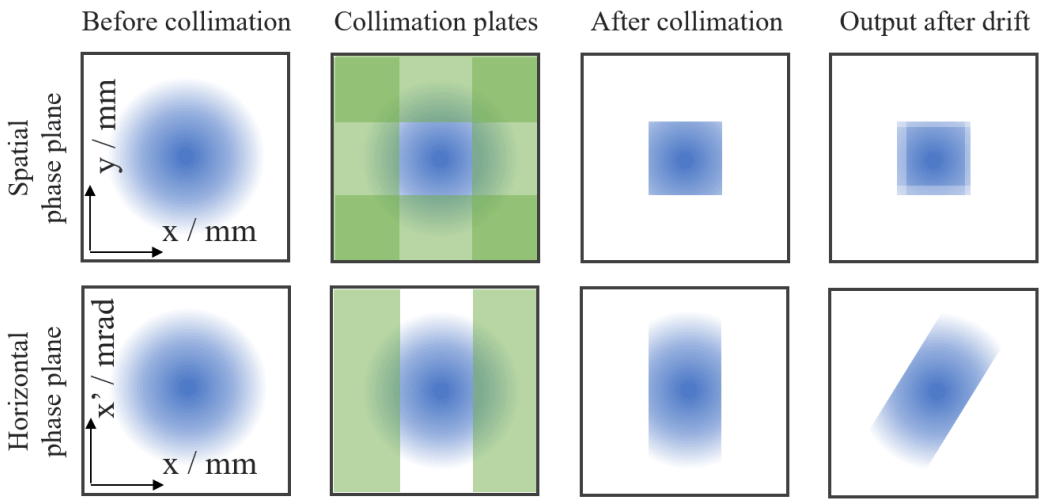

Figure 7.1: Beam cutting applying collimation slits in horizontal and vertical direction, depicted in the spatial plane (*top*) and horizontal phase plane (*bottom*).

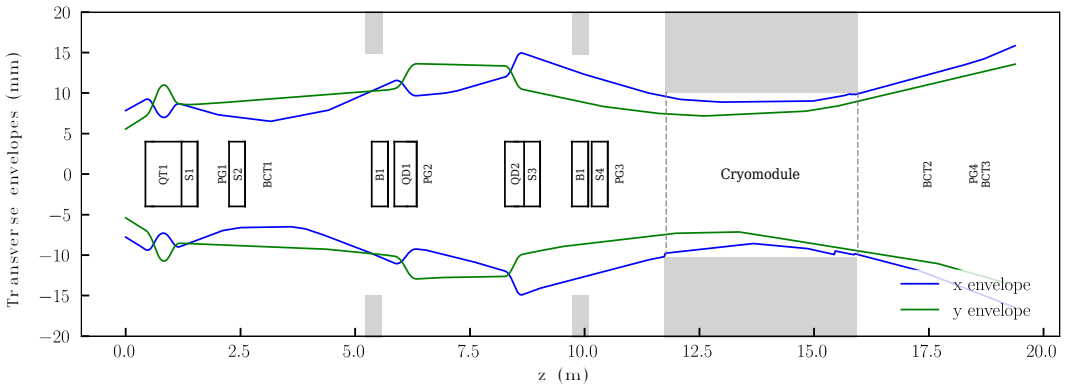

Figure 7.2: Design envelopes of a 1.4 MeV/u Ar^{8+} beam (see Table 7.1) HLI to the beam diagnostic test bench behind *Advanced Demonstrator*, optimized for minimum particle loss; relevant beamline components and beam diagnostics: Quadrupole Triplet (QT), Steerer (S), Profile Grid (PG), Beam Current Transformer (BCT), Quadrupole Doublet (QD), Rebuncher (RB). The gray blocks indicate the aperture of the external rebunchers and the cavities inside the cryomodule. The axis limits are scaled to the aperture of the quadrupoles [48].

In preparation of the full CM1 commissioning planned for 2022, a cold test of the cryomodule with heavy ion beam has been carried out. The CM1 cryostat features four hollow shells as dummy cavities, which are to be substituted by the actual SC CH cavities in the next step. The tests take place at the revised Demonstrator test cave; beam is delivered by the HLI via the identical matching beamline. For the upgrade, several elements of the beamline have been relocated and the new cryomodule, with more space for the four cavities, has been installed (see Figure 7.2). Therefore, the alignment of all elements has been verified, which is common practice for NC accelerators. For the beam quality monitoring, several beam diagnostic tools are available [47, 58, 122–124, 128–131].

The superconducting RF resonators mounted in the interior of the cryomodule, though, are inaccessible for standard alignment procedures. The cavities may alter both orientation and position when cooling from room temperature to the operating temperature of 4 K. Due to the engineering design features of the cryostat, the resonators are still alignable externally after they have cooled down by readjusting their mounting strings. To study the displacement of the devices inside the cryomodule (especially whilst beam commissioning), it is proposed to scan the aperture step by step using beam steerers, employing a symmetric, parallel beam with low transverse emittance, i.e., pencil-like. The measured effective aperture, as a result of the raster scan, could be used to profile the misalignment and guide the alignment team. As a huge beam spot, present without collimation, would distort and smear the raster image, the application of a collimation system is sufficient for advanced machine in-

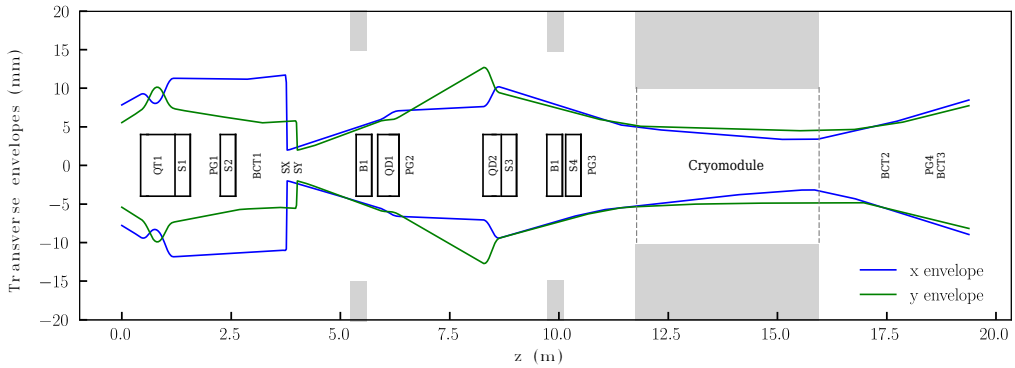

Figure 7.3: Design envelopes with collimation of a 1.4 MeV/u Ar^{8+} beam (see Table 7.1) from the injector HLI to the end of the *Advanced Demonstrator*. Relevant beamline components: Quadrupole Triplet (QT), Steerer (S), Profile Grid (PG), Beam Current Transformer (BCT), Horizontal-Vertical Slit (SX/SY), Quadrupole Doublet (QD), Rebuncher (RB). The gray blocks indicate the aperture of the external rebunchers and the cavities inside the cryomodule. The axis limits are scaled to the aperture of the quadrupoles [48].

spections, additional beam tuning, and reliable routine operation. Therefore, it is widely applied in various accelerator facilities worldwide [132–139].
The pencil-like beam is shaped at the HELIAC *Advanced Demonstrator* with a collimation system to minimize the beam width along the entire cryomodule (see Figure 7.3). Two grounded slits, aligned horizontally and vertically, were designed to scrape a part of the transverse distributed spatial particles and to provide a narrow beam spot with low divergence downstream of the slits. Due to a lack of mounting space, a second pair of slits, which is typically integrated for overall cutting of the beam halo, has been omitted. Since only two instead of four stepper motors have to control, the system is more compact and particularly user-friendly. The quadrupole settings and the corresponding geometric dimensions of the slits were found beforehand by dedicated beam dynamics simulations (see Section 7.2).
The collimation system is carried out to monitor the alignment of the cavities with a low duty cycle and a short-pulsed beam (delivered by HLI), resulting in a low beam current (50 µA pulse with 0.025 % duty-factor). The application of this system with high beam power is not foreseen, thus cooling of the plates can be omitted. Anyway, the engineering design of the collimation system must ensure that the thermal effects resulting from beam loss do not cause significant damage to the plates (see Section 7.3). Finally, reference emittance and transmission measurements of the pencil-like beam as well as measurements of the effective aperture using the collimated beam are presented, proving the versatile design (see Section 7.4).

7.2. Collimator Design & Reference Beam Dynamics

Since the cavity apertures inside the cryomodule should be probed with a symmetrical beam with low transverse emittance (about 1.5 mm mrad), the beam size must be minimized to provide the smallest possible diameter along the entire cryomodule. To provide for such a beam, slits are milled on two separate plates, which are aligned vertically and horizontally. The plates are installed behind the first quadrupole triplet, allowing for an adjustable beam spot at the plates.
For the design of the collimation system, beam dynamics simulations have been performed employing the multi-particle code DYNAMION [60], which allows for investigation of individual particle trajectories. The beam dynamics software was wrapped into a host interface to allow for a Nelder-Mead optimization [140] of the slit grid system in order to find the most beneficial design.
The input particle distribution has been specified by means of emittance measurements, which were carried out in a previous campaign [141]. The horizontal and vertical emittance delivered by HLI differs significantly by up to a factor of two (see Table 7.1).

Table 7.1: Design specifications and input parameters for beam dynamics simulations [48, 141].

Parameter	Value
Frequency f_0	108.408 MHz
Mass-to-charge ratio	6
Beam current I_{beam}	50 µA
Beam duty-factor	0.01 % to 25 %
Input beam energy W_{kin}	1.4 MeV/u
Particle distribution type	4D-Waterbag
Horizontal Twiss parameters	
α_x	−1.2
β_x	3.0 mm/mrad
ϵ_x	18.8 mm mrad
Vertical Twiss parameters	
α_y	−1.6
β_y	2.5 mm/mrad
ϵ_y	11.4 mm mrad

Due to a low beam current, less than 50 µA, space charge effects are negligible for this setup. In fact, even for the HELIAC design CW beam current of 1 mA it has been shown, that space charge effects have a minor effect on the beam behavior [11]. A 4D waterbag distribution is used to adequately account the transverse emittance measurements. The low coupling between longitudinal and transverse beam dynamics

in 6D phase space allows setting the longitudinal phase length and energy spread to zero.
A quadrupole triplet, two quadrupole doublets, a pair of collimation slits and the aperture limitations of the cryomodule are introduced for the particle trajectory calculations (see Figure 7.3). The slit width and all seven quadrupole gradients were determined.

In order to find the optimal slit configuration and the associated quadrupole gradients, a custom optimization software was written to find a layout with minimum transverse beam size and divergence within the entire cryomodule and at the final profile grid PG4 behind the cryomodule (see Figure 7.3) by choosing the quadrupole gradients. For layout optimization, the Nelder-Mead algorithm is applied, which in general minimizes a function $f(\vec{g})$.

In order to address the requirements to the system, a dedicated objective function is developed, which covers the following conditions:

- A narrow beam along the whole cryomodule (see Equation (7.2)).
- An overall medium beam size to stay inside the linear region of the quadrupoles and as a safety margin (see Equation (7.3)).
- Almost full beam transmission (only intentional losses at the slits are allowed, see Equation (7.4)).
- A beam with even spot size in the horizontal and vertical plane.

To meet the above requirements, the following steps are performed, gradually adjusting the quadrupole gradients using the Nelder-Mead algorithm.

1. Set quadrupole gradients $\vec{g}$ according to Nelder-Mead algorithm
2. Simulate beam dynamics and yield trajectories $\vec{x}(\vec{g})$ and $\vec{y}(\vec{g})$ until slit position
3. Sweep slit width and set width to set desired transmission
4. Calculate evolution of truncated particle ensemble until end of the beamline
5. Calculate objective function f (see Equation (7.1))
6. Report f to Nelder-Mead algorithm and repeat steps from 1. until convergence

This procedure yields the optimal combination of quadrupole gradients, characterized by $f(\vec{g})$, and the corresponding slit width. An objective function $f(\vec{g})$ (see Equation (7.1)) is defined, which depends on the quadrupole gradients $\vec{g}$ and the resulting horizontal $\vec{x}(\vec{g})$ and vertical $\vec{y}(\vec{g})$ particle trajectories. This function is subject of optimization and consists of the following three sub-objectives, which generally depend on the one-dimensional particle trajectory $\vec{u}$ as a placeholder for $\vec{x}$ and $\vec{y}$. They are

designed to provide a value of 0, if the sub-objective is met, and a value ≤ 1 if the sub-objective is missed within a tolerance range t_i. Values above the tolerance result in a quadratic penalty. The objective function is given by:

$$\begin{aligned} f(\vec{g}) =& f_1(\vec{x}_{\text{cry}}) + f_1(\vec{y}_{\text{cry}}) \\ &+ |f_1(\vec{x}_{\text{cry}}) - f_1(\vec{y}_{\text{cry}})| \\ &+ f_2(\vec{x}) + f_2(\vec{y}) \\ &+ f_3(\vec{x}) \end{aligned} \tag{7.1}$$

$$f_1(\vec{u}(\vec{g})) = \left(\frac{\max(\vec{u})}{t_1}\right)^2 \tag{7.2}$$

$$f_2(\vec{u}(\vec{g})) = \left(\frac{\max(\vec{u}) - u_{\text{target}}}{t_2}\right)^2 \tag{7.3}$$

$$f_3(\vec{u}(\vec{g})) = \left(\frac{\text{transmission}(\vec{u}) - t_{\text{target}}}{t_3}\right)^2, \tag{7.4}$$

whereas x_{cry} and y_{cry} are the trajectories inside the cryomodule, i.e., a sub-selection of $\vec{x}$ and $\vec{y}$.

The objective function f_1 is implemented to reduce the transverse beam envelope within the cryomodule to its minimum using a tolerance parameter of $t_1 = 2\,\text{mm}$.
The second term of the objective function $|f_1(\vec{x}_{\text{cry}}) - f_1(\vec{y}_{\text{cry}})|$ has as objective a symmetric transverse beam envelope, and thereby enforces a round beam inside the cryomodule.
The objective function f_2 reduces the beam size within the entire beamline to keep the beam within the linear part of the quadrupole field and has a target value $u_{\text{target}} = 7\,\text{mm}$ with a tolerance of $t_2 = 1\,\text{mm}$. This is a rather arbitrary parameter choice. However, during the initial use of the algorithm, it was found that these targets achieve an improved balance between f_3 and the other target values. An alternative would be an increased target size with a lower tolerance, e.g., $u_{\text{target}} = 12\,\text{mm}$, $t_2 = 0.3\,\text{mm}$. This in turn would have changed the quadratic behavior of the objective function and hence led to a different convergence behavior in combination with the other objective functions.
The objective function f_3 takes the particle transmission into account and addresses any unintended losses in addition to the intended losses at the collimator. Potentially, additional losses could occur at the minimum aperture half-width of 10 mm along the cryomodule, as shown in Figure 7.2, or the beam could be defocused to interfere with the quadrupole aperture. The transmission must be considered in particular in order to avoid the optimization algorithm from inadvertently scraping a part of the beam at a different position than at the collimation plates, which would yield a smaller beam size, as foreseen by the other objective functions.

To ensure a beam current measurement precision of 10 %, a lower beam current limit of 10 µA was chosen, since the measurement accuracy is ±1 µA. Accounting for the design beam current of 50 µA, a transmission through the slits of $t_{\text{target}} = 20\,\%$ is intended with a tolerance of $t_3 = 2\,\%$.

For taking the maximum quadrupole gradients $g_{\max}$ into account, another sub-objective f_4 might be included. Choices could have been

$$f_4(\vec{g}) = \begin{cases} \infty, & \text{if } \vec{g}_i \geq g_{\max} \\ 0, & \text{otherwise} \end{cases} \tag{7.5}$$

providing for a hard constraint, but is not differentiable. Another choice was

$$f_4(\vec{g}) = \exp\left(\frac{\vec{g}_i - g_{\max}}{t_4}\right), \tag{7.6}$$

which is differentiable and introduces a very high penalty if $g_{\max}$ is exceeded. The specific behavior and tolerance could be tuned by means of t_4. But the algorithm did converge to realistic gradients, thus has been decided to omit f_4 as a term of the objective function.

At each beam dynamics simulation run, the slit-width is automatically and dynamically adjusted. Since the slit width is thus indirectly defined from quadrupole gradients, the parameter search space is reduced and enables an efficient run-time of the software. For this process, the ensemble of particles is tracked forward to the slit. Then a slit width sweep is automatically preformed, and the width selected so that the targeted losses emerge at the slit. The cut and transmitted particle ensemble is then calculated to the end of the beamline. Finally, the objective function is executed as post-process.
Thus, the best list of quadrupole gradients with respect to $f(\vec{g})$ implicitly yields the appropriate slit width. As depicted in Figure 7.4, the optimization algorithm converges relatively fast within some few hundreds of steps. In general, the particular pattern of convergence varies considerably according to the initial parameters of the minimization and the specific configuration of the beamline, as well as the parametrization of the objective function.

Using the initial Twiss parameters known from the previous measurements (see Table 7.1), two different quadrupole settings, with and without collimation, are elaborated (see Table 7.2).
Without collimation, the quadrupole parameters are tuned for the lowest beam loss. Thus, the targeted transmission t_{target} is temporally constrained to 100 % (instead of 20 % with collimation). The primary origin of particle loss is the narrow aperture of 10 mm within the cryomodule (see Figure 7.2). For the future Advanced Demonstrator, two SC solenoid magnets are going to provide for a loss-free focusing scheme.

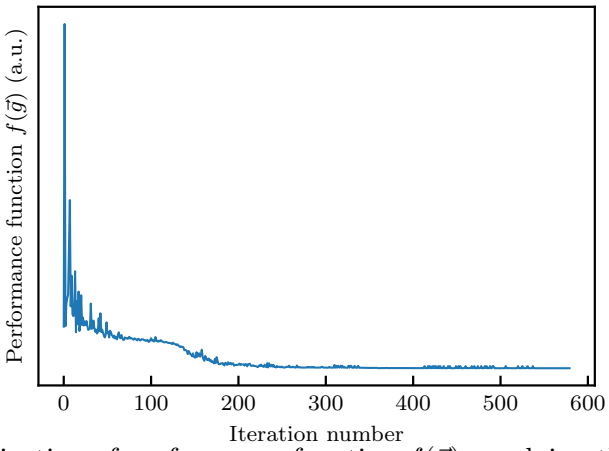

Figure 7.4: Minimization of performance function $f(\vec{g})$, applying the Nelder-Mead algorithm [48].

Table 7.2: Quadrupole design gradients [48].

Quadrupole	Gradient (T/m) without collimation	Gradient (T/m) 2 mm slit half-width
QT11	9.7	7.2
QT12	-8.6	-8.4
QT13	7.8	8.3
QD11	4.4	-1.6
QD12	-4.1	2.5
QD21	-6.1	-9.5
QD22	6.7	8.9

No solenoids were operated during the beam-based alignment process, as it could result in significant distortion of the pencil-like beam, including unwanted steering or emittance increase.
With the collimation system included in the beamline, the minimization of the objective function $f(\vec{g})$ results in quadrupole gradients as in Table 7.2 and a slit half-width of 1.93 mm. For practical reasons, a primary slit half-width of 2 mm is defined.
With the 2 mm slit half-width and the associated quadrupole gradients, the beam transmission is set to 20 %, delivering a narrow horizontal and vertical beam envelope within the cryomodule. In addition, a narrow bunch diameter at the profile grid PG4 at the end of the beamline is obtained (see Figure 7.3). For this layout with collimation, no additional beam losses occurred, apart from the intended losses at the slits.

Since a variety of ions ($A/Z \leq 8.5$) are available for acceleration at HLI, different beam parameters must be taken into account, particularly due to the ion

source being in different states of operation, such as varying beam intensities or different shape and size of beam emittances. In order to counteract these uncertainties, two additional slits with a half-width of 1.5 mm and 2.5 mm are milled on a common plate (see Figure 7.5(a)). A backup option with only two slits per plate for use with very high beam emittances was designed as well (see Figure 7.5(b)).

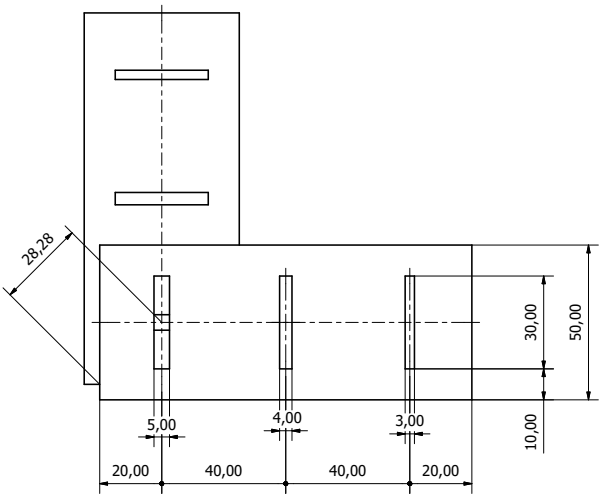

(a) Three slit plate layout

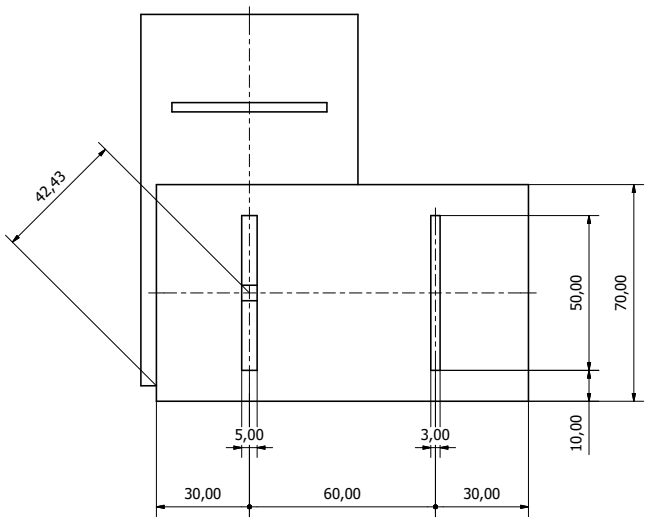

(b) Two slit plate layout

Figure 7.5: Layout of collimation plates (2 mm plate-depth): three slit (a) and two slit (b) layout option [48].

Table 7.3: Calculated beam transmission for different slit combinations [48].

Slit half-width		horizontal		
		2.5 mm	2.0 mm	1.5 mm
vertical	2.5 mm	29.0 %	24.3 %	19.1 %
	2.0 mm	23.4 %	19.7 %	15.6 %
	1.5 mm	17.7 %	14.9 %	11.7 %

Table 7.4: Simulated emittances ϵ_x/ϵ_y (mm mrad); the corresponding transmission is depicted in Table 7.3 widths [48].

Slit half-width		horizontal		
		2.5 mm	2.0 mm	1.5 mm
vertical	2.5 mm	6.3 / 7.4	5.2 / 7.4	3.8 / 7.4
	2.0 mm	6.2 / 6.1	5.0 / 6.2	3.8 / 6.1
	1.5 mm	6.1 / 4.5	5.1 / 4.4	3.9 / 4.4

In order to allow a broader variation of the beam parameters, the additionally embedded slits could be selected for operation by moving the plate to the corresponding position (see Table 7.3 and 7.4). By altering the slit widths, the required intensity for measurements could be achieved independently of the quadrupole gradients in simulations and during experimental machine investigations (see Table 7.3). Since the slit size could be selected separately horizontally and vertically, this also results in different emittances ϵ_x and ϵ_y. Thus, a similar output emittance behind the collimation system can be obtained (see Table 7.4) even for different input emittances, simplifying subsequent analysis of the scanning of the apertures. The adjustable beam transmission is particularly beneficial to limit the beam diameter further when the beam current exceeds the design current (derived from the beam current measurement accuracy to obtain 10 % transmission accuracy) of 10 µA obtaining an even more pencil like beam. An insufficient low beam current is compensated by using increased slit widths, resulting in higher particle transmission.

The plate layout with three slits thus allows a high flexibility to counteract possible deviations (to larger values) from the design beam emittance. Nevertheless, if the beam is too wide, there is a risk that particles will pass the collimation system through several slits at the same time or bypass the plate. Although simulations with an 8-fold design emittance did not indicate this undesired effect, the risk is addressed with a second plate design, which features two slits on one plate, instead of three (see Figure 7.5(b)). Thus, the distance between two neighboring slits and to the plate

border is larger. A beam with an unexpectedly large diameter should be sufficiently scraped.
As the size of the designed slits is in the order of a few mm for both plate designs, beam scattering at the slits is negligible.
The operation of the collimation system is not intended for routine CW operation, but for low duty-factor and low pulse-length beam. Since damage to the plates by the beam is thus avoided and since beam transformers upstream and downstream of the collimation system are available for beam transmission measurement, the incident beam current is not planned to be measured directly on the plates.

7.3. Thermal Load

In order to evaluate the thermal load for the collimation system, the usual operating modes of the HLI Injector are considered. Two different operation modes are typically used at the HLI: 25 % and decreased to below 0.025 % duty cycle. The low duty cycle operation mode is specially employed to protect the profile grids, which could otherwise be damaged, and is sufficient to be applied for beam-based alignment of the cavities in the cryostat. Therefore, the collimation system is not intended to be exposed at full beam power. The maximum beam power, dissipated at the collimation system, P_{loss} is

$$P_{\text{loss}} = W_{\text{kin}} \cdot \frac{I_{\text{beam-loss}}}{Q \cdot e}, \tag{7.7}$$

where W_{kin} is the kinetic energy of a particle, $I_{\text{beam-loss}}$ is the beam current, Q is the charge state, and e is the elementary charge [69]. For a commonly delivered 1.4 MeV/u Ar^{6+} ion beam and a beam current of 50 µA, a beam power of about 115 mW is obtained for a duty factor of 0.025 %. A beam power of 115 W could be obtained with the high duty factor 25 %.
Two different methods are used to study the thermal behavior of the plates: CST [126] simulations (see Figure 7.6) and analytical calculations.

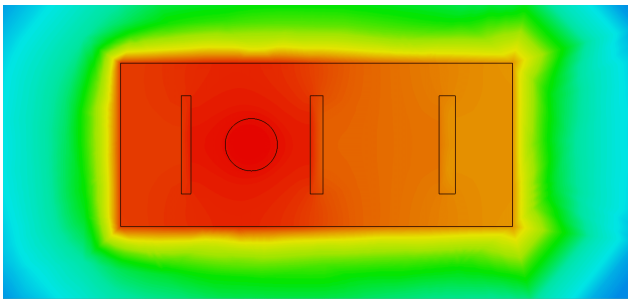

Figure 7.6: Temperature distribution on the plate for $P_{\text{loss}} \approx 115$ mW. Colors indicate temperatures from 290 K to 300 K [48].

The analytical calculation considers a plate without slits, heated uniformly by the incident beam, and surrounded by vacuum. According to the Bethe-Bloch formula,

the penetration depth of the ions is predicted to be less than 10 µm. Therefore, all losses are assumed to be located at the surface. Only blackbody radiation has been assumed for cooling of the plates. The heat Q of the stainless steel block increases accordingly

$$\frac{\delta Q}{\delta t} = P_{\text{loss}} - \epsilon \sigma A T^4, \tag{7.8}$$

with the emissivity ϵ, the Stefan-Boltzmann constant σ, the surface area A, and temperature T.
For the proposed application of the collimation system with a beam duty-factor of 0.025 %, the plates are being heated by about 10 K, which allows application of the plates for long-term use. The saturation temperature is governed by the emissivity ϵ, ranging from $\epsilon_{\text{polished}} = 0.075$ to $\epsilon_{\text{rolled}} = 0.85$ by the fabrication parameters. The lowest emissivity is selected as the worst-case scenario. The implementation of the collimation system is not intended for CW operation, as the plates could be damaged at a ΔT of for instance 900 K to 1500 K, depending on the emissivity.

7.4. Commissioning

Beam commissioning of the transport line, with the assembled collimation system (see Figure 7.7), was performed at a beam current of approximately 50 µA $^{40}Ar^{+8}$. The quadrupole gradients could be scaled according to the mass-to-charge ratio in the absence of noticeable space charge effects, as usual in standard operation.
The quadrupole and steerer gradients have been adjusted to achieve almost full transmission (94 %) through the beamline confirming simulation results.

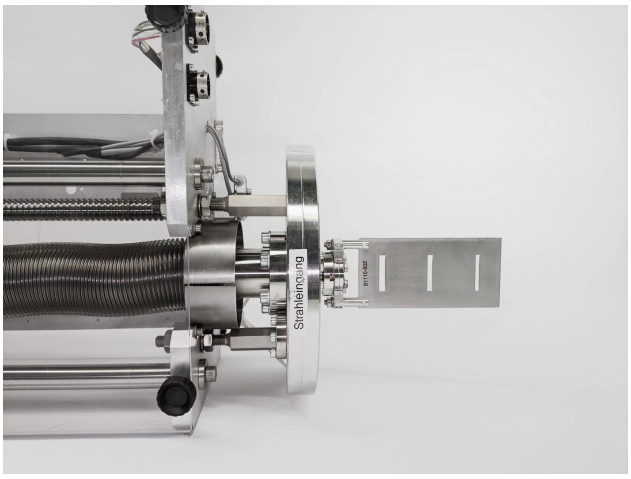

Figure 7.7: 3-slit plate mounted on a separate stepper motor, installed at the Advanced Demonstrator beamline [48].

The losses occurred at two dummy diaphragms, with an aperture radius of 11 mm, which were inserted into the beamline to replicate the aperture limits of the Advanced Demonstrator cold string. A misalignment has been artificially established by an on purpose vertically displaced diaphragm.
At the end of the beamline, transverse emittance measurements were performed (see Figure 7.8) using the emittance measurement system, operating according to the slit grid principle MobEmi [59] at a dedicated beam diagnostics test stand. From previous experience, a measurement accuracy of 5 % could be assumed. A macroparticle distribution, derived from emittance measurements, was backtracked to the start position of the beamline (see Table 7.5) to compare it with the design particle distribution (see Table 7.1).
The observed emittance shape and size are highly consistent with the design emittance (below 8 % relative difference). The measured backtracked beam spot at the start position of the transport line, however, deviates by 30 % from the corresponding reference design. At the time when the reference measurements were performed [141] (on which the initial specifications are based), the ion source and injector were in a different state of operation compared to the present measurement campaign. Anyway, the different beam spot size was compensated upstream of the collimation system by the first quadrupole triplet. However, the actual density distribution is inhomogeneous and showed a more dense central pattern compared to the assumed 4D-Waterbag distribution.

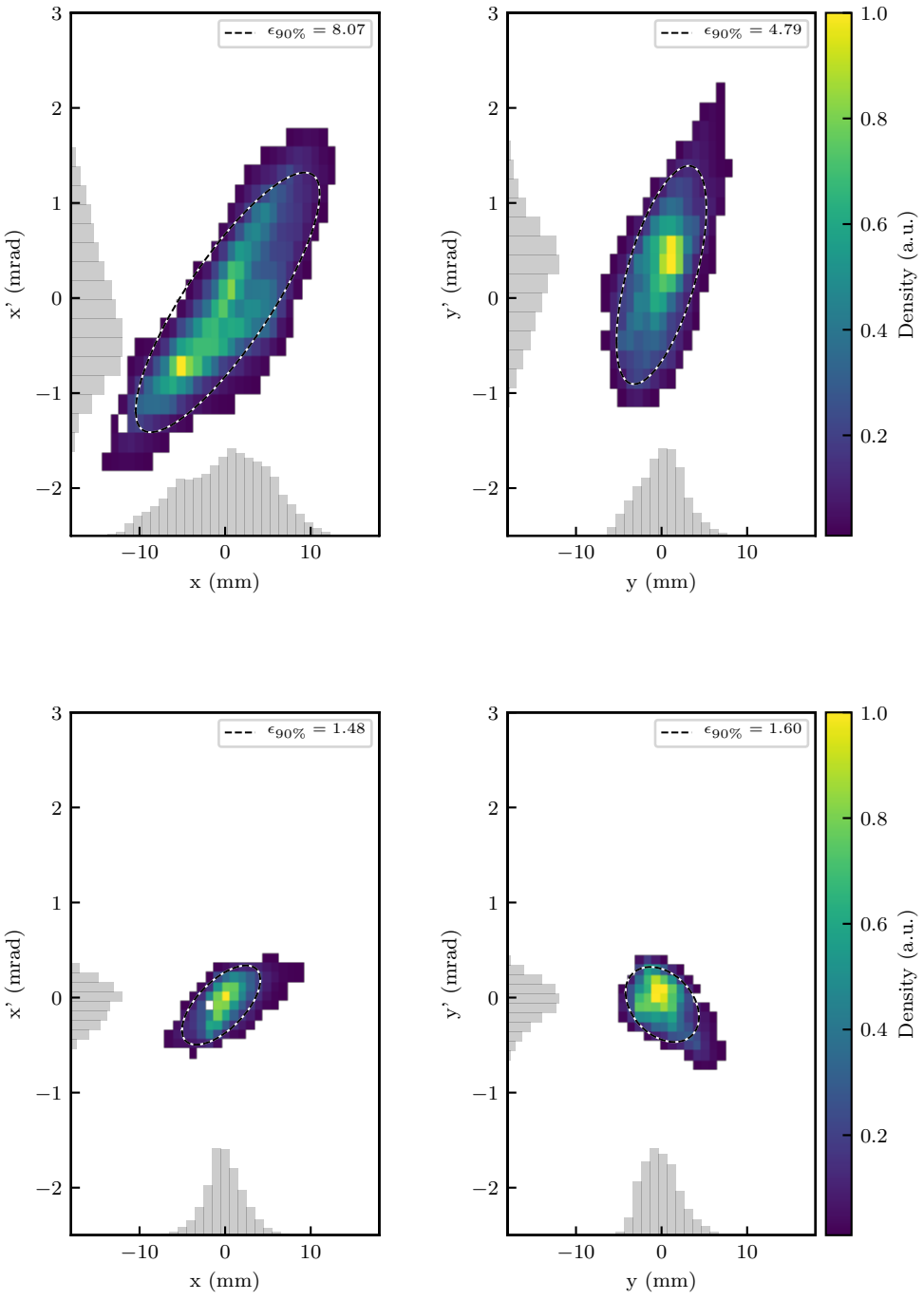

Figure 7.8: Transverse beam emittance measurements (1 mm and 0.2 mrad resolution) at the end of the transport line without (*top*) and with inserted collimation slits (*bottom*). The ellipses enclose 90 % of the particles with a minimum area [48].

Table 7.5: HLI output beam parameters backtracked from measurements [48].

Parameter	Value
Ion species	$^{40}Ar^{+8}$
Mass-to-charge ratio	5
Beam current I_{mean}	50 µA
Beam energy W_{kin}	1.4 MeV/u
Twiss parameters	
α_x	−1.1
β_x	1.4 mm/mrad
ϵ_x	17.3 mm mrad
α_y	−1.5
β_y	1.4 mm/mrad
ϵ_y	11.5 mm mrad

The collimation properties with exchangeable slit size have been investigated intensively: the plates comprising three slits were mounted horizontally and vertically on two separate stepper motors to investigate different slit combinations. The results are in first order as predicted by the previous simulations. Overall, caused by different beam density distributions, about 40 % higher transmission through the slits could be achieved (see Table 7.6), leading to an improved measurement accuracy of the beam current. The measured transverse emittance was lower than the predicted values (see Figure 7.9), allowing measurement with an even smaller beam envelope along the cryostat.

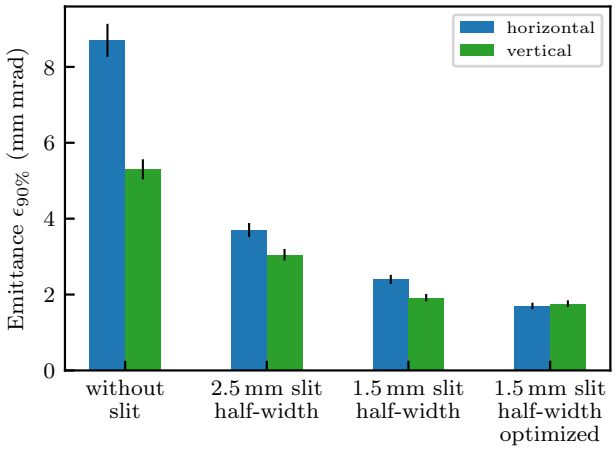

Figure 7.9: Comparison of transverse beam emittance with varied level of collimation by means of different slit widths [48].

Moreover, the beam is symmetrized by final adjustments to the gradients at the quadrupole triplet before the collimation system, which is referred to as the optimized

setting. Although the initial emittances differ considerably, the emittance and beam width in the horizontal and vertical direction after the collimation system are equal in this case, which is an important feature of the system. The measured emittance is a factor of two lower (with the setting optimized) than foreseen by simulations. Because the actual brilliance of the beam, a narrow beam is anticipated for the future beam-based investigations.

Table 7.6: Measured beam transmission for combinations of different slit half-widths [48].

Slit half-width		horizontal		
		2.5 mm	2.0 mm	1.5 mm
vertical	2.5 mm	39.0 %	31.5 %	22.4 %
	2.0 mm	34.0 %	27.0 %	19.0 %
	1.5 mm	28.0 %	23.3 %	16.0 %

Scanning of the effective aperture along the whole cryomodule is possible with the pencil-like beam, especially with the optimized setting. For aperture scanning, the beam center is displaced transversely from the main axis with two steerer pairs (see Figure 7.10).

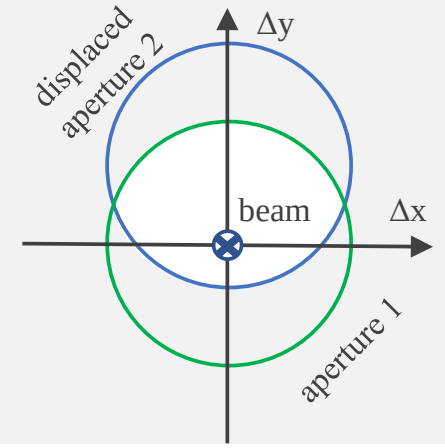

Figure 7.10: Geometric sketch of transverse beam offset and Intersection of two apertures [48].

The beam offset was monitored to be constant with two separate beam profile grids PG3/PG4 upstream and downstream of the cryomodule. The beam current in dependence on the offset was measured with a beam current transformer behind the cryomodule. Thus, the effective aperture is scanned, and its diameter can be derived from the difference between the two facing beam offsets, each showing half of the maximum transmission. This specific transmission means that the beam is moved to the edge of the cryomodules aperture, and thus half of the beam is lost at the aperture.

In order to simulate misalignment, one of the diaphragms was intentionally shifted vertically during assembly. As a consequence of this misalignment, a smaller effective aperture is to be expected, which is determined by the intersection of the two round diaphragms with a radius of 11 mm, as illustrated in Figure 7.10.
The two superimposed diaphragms have a biconvex shape, which substantially reduces the effective aperture in both directions (in reference to the ideal axis), although the diaphragm is shifted only in one direction. Two separate aperture scans were performed along the horizontal x and vertical y axes. The results of these series of measurements are shown in Figure 7.11.

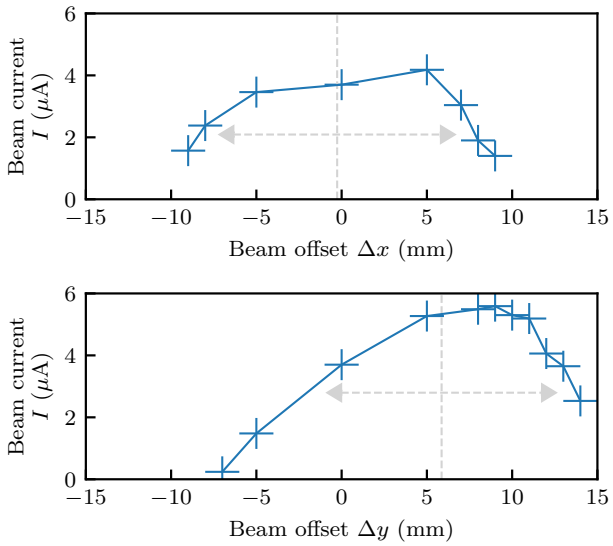

Figure 7.11: Horizontal and vertical aperture-scan (with error bars) with a pencil-like beam [48] applied at the dummy equipped cryomodule.

The blurred image at the left edge of the vertical scan is due to one diaphragm being distant from the beam focus. The second diaphragm is closer to the beam focus and its image is thus sharper. A prominent misalignment is found to occur with $y_{\text{center}} = 5.8 \pm 2\,\text{mm}$ vertically and an insignificant one is found horizontally $x_{\text{center}} = 0 \pm 2\,\text{mm}$, reducing the effective vertical aperture radius from 11 mm to $r_y = 8.1 \pm 2\,\text{mm}$ and the horizontal one to $r_x = 8.5 \pm 2\,\text{mm}$. Since the reference beam axis does not match the center of the effective aperture vertically, a smaller effective aperture is obtained for $I(\Delta x)|_{y=0\,\text{mm}}$ compared to a scan outside the beam axis $I(\Delta x)|_{y=6\,\text{mm}}$.
The scanning accuracy is limited by the 1 mm spacing of the individual wires in the profile grid. Potentially, the accuracy could be further enhanced below one millimeter by employing beam position monitors rather than beam profile grids. Hence, such a scanning method is found to be well applicable, for the dummy cavities and as well as for the original RF cavities for the upcoming commissioning of the entire HELIAC.

7.5. Discussion

A new collimation system for the heavy ion CW SC 1.4 MeV/u HELIAC Advanced Demonstrator has been designed, fabricated and successfully commissioned. It provides for a narrow transverse beam of low divergence (pencil-like), with an emittance of about 2 mm mrad. This corresponds to a cut of 90 % of the initial beam emittance. The process of beam-based alignment has been demonstrated employing test diaphragms. It is foreseen to be used for the alignment of the superconducting cavities inside the HELIAC cryomodules. Due to the advanced technical design of the cryomodule, the realignment of the cavities in the cold state is possible applying a probe beam. The presented beam collimation system is a powerful tool to allow for sophisticated machine investigations with a pencil-like beam, and therefore could be potentially of interest for further superconducting accelerator applications.

8. Summary & Outlook

8.1. Summary

The superconducting heavy ion linear accelerator **HE**lmholtz **LI**near **AC**celerator (HELIAC) is going to be built for the research and discovery of Super Heavy Elements at GSI in Darmstadt in close collaboration with HIM and IAP and formerly with the **K**urchatov **I**nstitute - **I**nstitute for **T**heoretical and **E**xperimental **P**hysics (KI-ITEP) and **M**oscow **E**ngineering **Ph**ysics **I**nstitute (MEPhI). Due to the application of **S**uper**C**onducting (SC) components in **C**ontinuous **W**ave (CW) operation, HELIAC has extremely high beam transmission requirements, which must be achieved by sufficient beam acceleration and matching to the SC section. This thesis is mainly concerned conserving the beam quality along the beamline for the injection in the SC HELIAC section, applying a dedicated design of the **N**ormal **C**onducting (NC) injector linac and by advanced measurement and optimization efforts for the beam transport system:

- A novel reconstruction algorithm was developed to calculate the parameters of the longitudinal particle density-distribution, suitable for general machine and beam transport optimization.
- A new beam collimation system has been designed and put into operation, which will be used for beam-based alignment of the hardly accessible elements inside the cryostat by means of a pencil beam.
- A normal-conducting injector DTL with an embedded advanced APF beam dynamics scheme has been developed.

In order to match the beam effectively to the HELIAC, the beam emittance and its Twiss parameters should be known in the transverse and longitudinal phase planes. For precise transverse bunch shape measurements, various devices are already employed for routine operation at GSI and other leading research centers. For longitudinal beam emittance characterization, no standard diagnostics device is available so far. Nevertheless, a sophisticated algorithm was developed to reconstruct the image of the particle density-distribution on the longitudinal phase plane. The implementation and practical application of the algorithm enables improved beam matching to the SC HELIAC, and the optimization of both the currently employed High Charge State Injector (HLI) and the dedicated future HELIAC injector.
The longitudinal beam portrait is reconstructed from multiple different measurements of the phase-density profile with a Feschenko-type **B**unch **S**hape **M**onitor

(BSM). The set of experimental data was used as input for the **N**on **N**egative **L**east **S**quares (NNLS) algorithm in combination with a beam transport model using the multi-particle code DYNAMION.
During several beam campaigns at the Demonstrator beamline two rebunchers have been employed to alter the beam transport, in order to measure different mappings of the bunch shape at the BSM.
Furthermore, independent longitudinal bunch shape measurements were carried out behind the already commissioned first HELIAC cavity CH0 with nonlinear beam dynamics to further verify the reconstructed longitudinal bunch portrait. The verification was realized by a sufficient prediction of the measured bunch shape, which was made possible by an accurate representation of the input bunch and a precise non-linear acceleration model. Additionally, the reconstruction results were successfully validated by simultaneously operating a second BSM at the position of the reconstruction point. The predicted bunch density-distribution is in sufficient agreement with the directly measured bunch shape, confirming impressively the reconstruction method.
Hence, a versatile tool with a high level of detail to study the matching of the beam to the SC CW Advanced Demonstrator and to the HELIAC is now available to aim for high performance of the entire system.

Moreover, the machine performance and beam quality could be improved by a dedicated alignment procedure of the hardly accessible SC cavities mounted inside cryostats. A dedicated beam collimation system for beam-based alignment of the HELIAC Advanced Demonstrator by means of a pencil beam has been designed, fabricated, and successfully commissioned. The result of beam-based alignment has been demonstrated with test diaphragms, emulating misaligned elements inside a cryomodule. The collimation system provides for a transversely 2 mm thin beam of 1 mrad divergence, with an emittance of about 2 mm mrad, which provides for a beam current of 10 µA that can be reliably monitored with the already installed beam instrumentation. Therefore, the presented beam collimation system, being a powerful tool for sophisticated machine investigations with a pencil beam, could be of major interest, especially for SC accelerator systems employing hardly accessible elements inside cryomodules. It is foreseen to employ the pencil beam for alignment of the sixteen SC cavities inside the four HELIAC cryomodules.

An APF scheme was elaborated for the dedicated HELIAC normal conducting CW injector linac, employing two separately powered IH-cavities. This design approach allows for effective acceleration whilst preserving the beam quality delivered by the ion source.
In general, the principle of APF beam dynamics allows for long multi-gap cavities without transversely focusing magnetic lenses inside the cavities. The newly proposed accelerating/focusing scheme was developed by means of global optimization of a DTL-cavity geometry. The design is based on a 3 MV/m acceleration gradient for heavy ions of a mass-to-charge ratio of 6.

A dedicated synchronous phase law for beam acceleration and focusing was developed for the two accelerating cavities. In particular, the first cavity has been designed for robust beam transport and for embedded beam matching to the second cavity. Furthermore, dedicated beam parameters at the exit of the second cavity allow for a compact matching section to the SC HELIAC. The resulting beam emittance growth of less than 5 % in each cavity is sufficiently low in all phase planes. The independently powered cavities and their dedicated intertank section, equipped with a quadrupole triplet and beam diagnostics devices, allow for eased commissioning, maintenance, operation, as well as potential further upgrade measures. The cavities are currently tendered, fine adjustments, taking the technical proposals of the cavity manufacturer into account, have to be finally incorporated.

In summary, the *transverse* alignment of superconducting HELIAC components has been improved by a collimation system, the *longitudinal* accelerator performance could be enhanced by using the developed reconstruction method of the longitudinal beam portrait, and the *overall* effective HELIAC acceleration and beam quality is going to be enhanced by the new design of a normal-conducting injector **D**rift **T**ube **L**inac (DTL).

8.2. Outlook

The collimation system, as well as the reconstruction algorithm, were successfully implemented in the Advanced Demonstrator beamline. Both are at disposal for upcoming commissioning activities of the HELIAC.
The reconstruction algorithm could potentially be applied to other accelerator systems, both at GSI and at different other accelerator centers.
The presented method for collimation system design can be applied elsewhere for rapid development of such equipment, whereas the produced collimation system will be extensively used for the Advanced Demonstrator commissioning. The **A**lternating **P**hase **F**ocusing (APF) **I**nterdigital **H**-mode (IH) cavities are currently tendered and are foreseen to be operated as a part of the new dedicated NC injector linac of the HELIAC. On the base of actual cavity performance, it is foreseen to further develop the APF beam dynamics scheme and software for future particle accelerators.
A major milestone for the entire HELIAC project is the Advanced Demonstrator commissioning, foreseen for 2022. The first cryomodule, equipped with an SC rebuncher, three SC **C**rossbar **H**-mode (CH) cavities, and two SC solenoids, is going to be tested. Subsequent user experiments will be carried out at an intermediate output energy of $\leq 3.3\,\mathrm{MeV/u}$. The following project milestones and construction stages are going to extend the variable output energy of the linac up to $7.3\,\mathrm{MeV/u}$ for a mass-to-charge ratio of ≤ 6. The heavy ion SC HELIAC will deliver high quality heavy ion beams for future discoveries of super heavy elements, as well as for potential material research and medical research at **GSI** Helmholtz Centre for Heavy Ion Research (GSI).

A. Appendices

A.1. MENT

A.1.1. Vectorized Algorithm

Algorithm 4: Maximum Entropy Technique: Discrete Version

Data: Measurements $\{A_k\}$, Mappings $\{\Omega_k\}$
Initialize vectors $\{\vec{h}_k = \vec{1}\}$
for $i = 0..N_{\max}$ **do**
  for $k = 0..K$ **do**
    $\vec{f}_{\text{tmp}} = \prod_{k'|k' \neq k}^{K} \Omega_{k'}^{-1} \cdot \vec{h}_{k'}$
    $\vec{A}_{k,\text{tmp}} = \Omega_k \cdot \vec{f}_{\text{tmp}}$
    $\vec{h}_k = \frac{\vec{A}_k}{\vec{A}_{k,\text{tmp}}}$ (where $\vec{A}_{k,\text{tmp}} \neq 0$)
  end
end
Result: Flattened image $\vec{f}$

A.1.2. Reconstruction Results

Supplemental figures for Table 5.1 on page 65

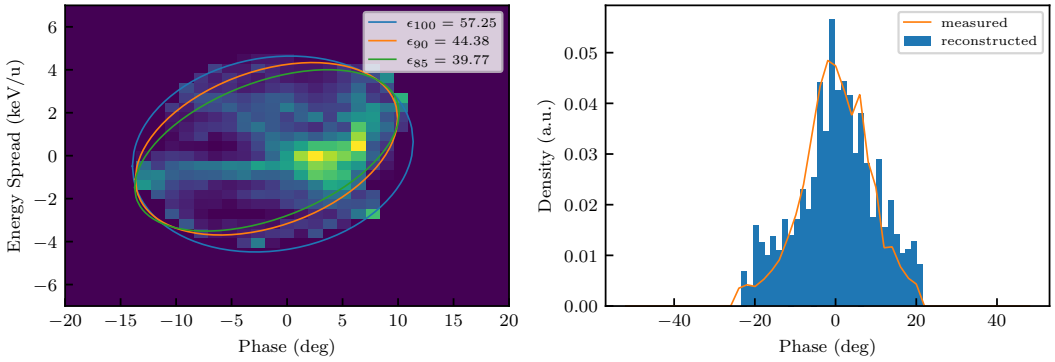

(a) HLI control setting: 4.04 V, 110°, 28.05.2021, $R^2_{\text{train}} = 0.90$, $R^2_{\text{test}} = 0.94$

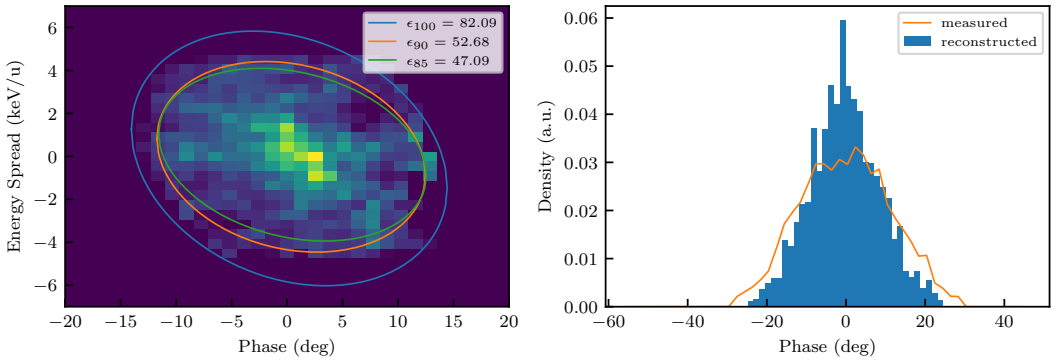

(b) HLI control setting: 4.08 V, 122°, 28.05.2021, $R^2_{\text{train}} = 0.90$, $R^2_{\text{test}} = 0.77$

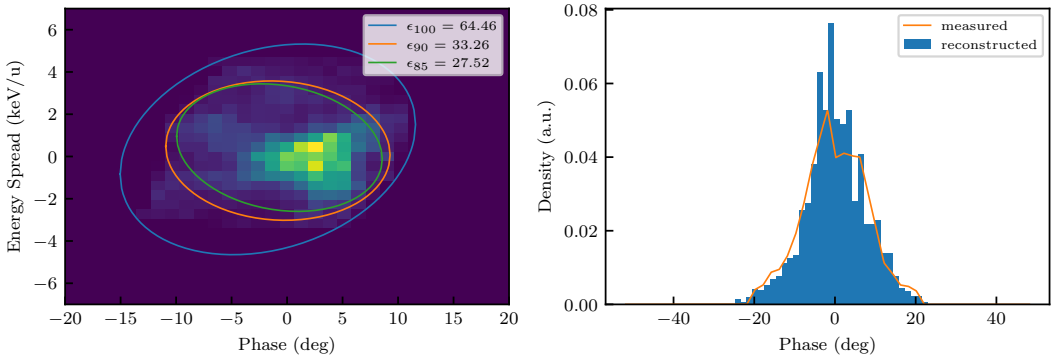

(c) HLI control setting: 4.04 V, 119°, 31.05.2021, $R^2_{\text{train}} = 0.94$, $R^2_{\text{test}} = 0.90$

Figure A.1: Reconstructed longitudinal density-distribution (*left*) and validation of the reconstruction with a dedicated, independent BSM (*right*)

A.2. Preliminary APF Designs

A.2.1. Preliminary One-Tank Layout

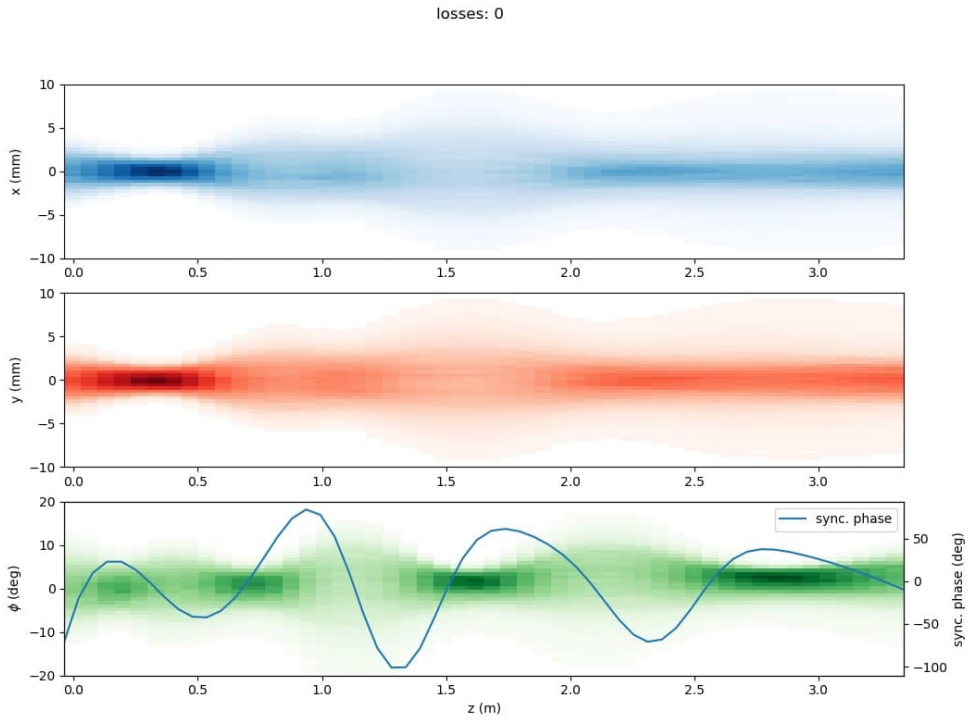

Figure A.2: Draft of a one-tank layout with embedded APF beam dynamics, calculated with non-linear 6D phase plane coupling using DYNAMION.

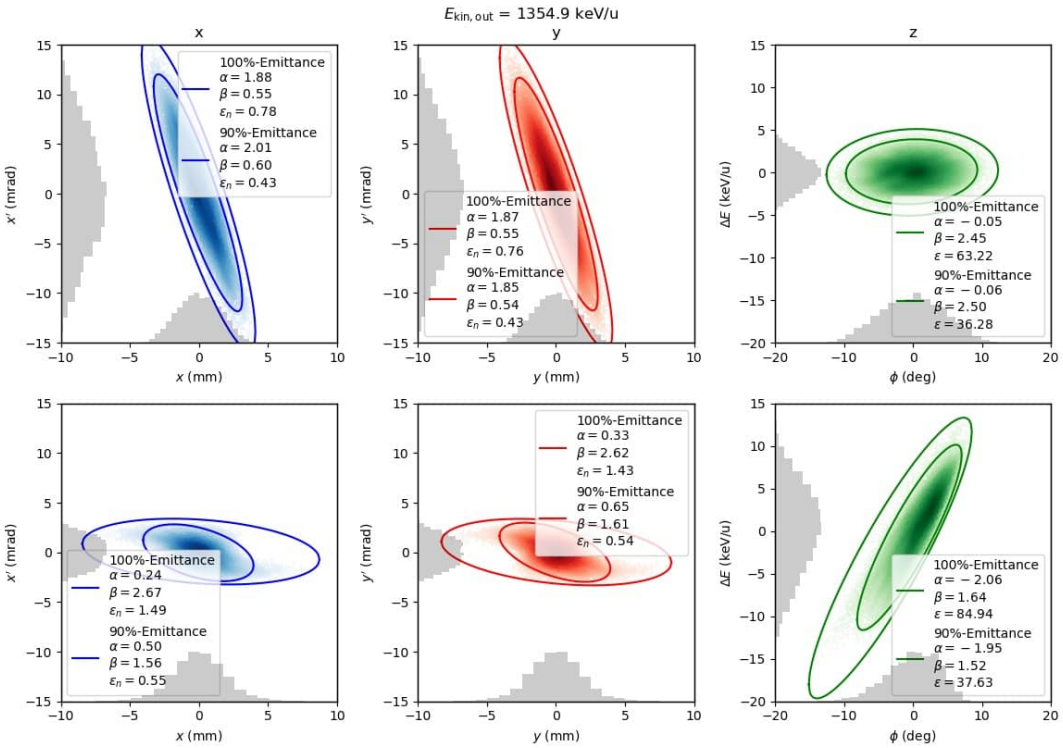

Figure A.3: Input (*left*) and output (*right*) of a one-tank layout with embedded APF beam dynamics.

Acknowledgments

This page intentionally left blank.

List of Acronyms

APF **A**lternating **P**hase **F**ocusing.
ART **A**lgebraic **R**econstruction **T**echnique.

BCT **B**eam **C**urrent **T**ransformer.
BPM **B**eam **P**osition **M**onitor.
BSM **B**unch **S**hape **M**onitor.

CH **C**rossbar **H**-mode.
CHORDIS **C**old or **HO**t **R**eflex**D**ischarge **I**on **S**ource.
CW **C**ontinuous **W**ave.

DTL **D**rift **T**ube **L**inac.

E-mode **E**lectric Mode.
ECRIS **E**lectron **C**yclotron **R**esonance **I**on **S**ource.
EQUUS **EQU**idistant m**U**ltigap **S**tructure.

FAIR **F**acility for **A**ntiproton and **I**on **R**esearch at Darmstadt.
FBP **F**iltered **B**ack **P**rojection.

GSI **GSI** Helmholtz Centre for Heavy Ion Research.

H-mode Magnetic Mode.
HELIAC **HE**lmholtz **LI**near **AC**celerator.
HIM **H**elmholtz **I**nstitute **M**ainz.
HITRAP linear decelerator **H**eavy **I**on **TRAP**.
HLI High Charge State Injector.
HSI High Current Injector.
HWR **H**alf **W**ave **R**esonator.

IAP **I**nstitute for **A**pplied **P**hysics Frankfurt.
IH **I**nterdigital **H**-mode.

KONUS Combined Zero Degree Structure.
KV **K**apchinskiy-**V**ladimirsky.

LEBT **L**ow **E**nergy **B**eam **T**ransport.
LIGHT **L**aser **I**on **G**eneration, **H**andling and **T**ransport.

MEBT **M**edium **E**nergy **B**eam **T**ransport.

MENT **M**aximum **EN**tropy **T**echnique.
MEVVA **ME**tal **V**apor **V**acuum **A**rc Ion Source.
MobEmi **MOB**ile **EMI**ttance Measurement Device.
MUCIS **MU**lti **C**usp **I**on **S**ource.

NC **N**ormal **C**onducting.
NNLS **N**on **N**egative **L**east **S**quares.

PG Beam **P**rofile **G**rid.
PIG **P**enning **I**onization **G**auge.
PMQ **P**ermanent **M**agnet **Q**uadrupole.

QD **Q**uadruole **D**oublet.
QT **Q**uadruole **T**riplet.
QWR **Q**uarter **W**ave **R**esonator.

RB **R**e**B**uncher.
RF **R**adio **F**requency.
RFQ **R**adio **F**requency **Q**uadrupole.
RMS **R**oot **M**ean **S**quared.

S **S**teerer.
SART **S**imultaneous **A**lgebraic **R**econstruction **T**echnique.
SC **S**uper**C**onducting.
SHE **S**uper**H**eavy **E**lement.

TE-mode **T**ransverse **E**lectric Mode.
TM-mode **T**ransverse **M**agnetic Mode.

UNILAC **UNI**versal **L**inear **AC**celerator.

VARIS **V**acuum **AR**c **I**on **S**ource.

Bibliography

[1] M. Block, D. Ackermann, K. Blaum, C. Droese, M. Dworschak, *et al.*, "Direct mass measurements above Uranium bridge the gap to the island of stability," *Nature*, vol. 463, no. 7282, pp. 785–788, 2010.

[2] J. Khuyagbaatar, A. Yakushev, C. E. Düllmann, D. Ackermann, L. L. Andersson, *et al.*, "Search for elements 119 and 120," *Phys. Rev. C*, vol. 102, no. 6, p. 064602, 2020.

[3] W. Barth, W. Bayer, L. Dahl, L. Groening, S. Richter, *et al.*, "Upgrade program of the high current heavy ion UNILAC as an injector for FAIR," *Nucl. Instrum. Methods Phys. Res. A*, vol. 577, no. 1, pp. 211–214, 2007.

[4] W. Barth, A. Adonin, C. Düllmann, M. Heilmann, R. Hollinger, *et al.*, "High brilliance Uranium beams for the GSI FAIR," *Phys. Rev. ST Accel. Beams*, vol. 20, p. 050101, 2017.

[5] L. Groening, W. Barth, W. Bayer, G. Clemente, L. Dahl, *et al.*, "Benchmarking of measurement and simulation of transverse RMS-emittance growth," *Phys. Rev. ST Accel. Beams*, vol. 11, no. 9, 2008.

[6] W. Barth, A. Adonin, C. E. Düllmann, M. Heilmann, R. Hollinger, *et al.*, "U^{28+}-intensity record applying a H_2-gas stripper cell," *Phys. Rev. ST Accel. Beams*, vol. 18, no. 4, p. 040101, 2015.

[7] A. Adonin and R. Hollinger, "Beam brilliance investigation of high current ion beams at GSI heavy ion accelerator facility," *Rev. Sci. Instrum.*, vol. 85, p. 02A727, 2014.

[8] S. Yaramyshev, H. Vormann, A. Adonin, W. Barth, L. Dahl, *et al.*, "Virtual charge state separator as an advanced tool coupling measurements and simulations," *Phys. Rev. ST Accel. Beams*, vol. 18, 2015.

[9] W. Barth, K. Aulenbacher, M. Basten, M. Busch, F. Dziuba, *et al.*, "First heavy ion beam tests with a superconducting multigap CH cavity," *Phys. Rev. Accel. Beams*, vol. 21, p. 020102, 2018.

[10] W. Barth, K. Aulenbacher, M. Basten, F. Dziuba, V. Gettmann, *et al.*, "A superconducting CW-linac for heavy ion acceleration at GSIX," *EPJ Web Conf.*, vol. 138, p. 01026, 2017.

[11] M. Schwarz, S. Yaramyshev, K. Aulenbacher, W. Barth, M. Basten, *et al.*, "Reference beam dynamics layout for the SC CW heavy ion HELIAC at GSI," *Nucl. Instrum. Methods Phys. Res. A*, p. 163044, 2019.

[12] W. Barth, K. Aulenbacher, M. Basten, M. Busch, F. Dziuba, *et al.*, "Superconducting CH-cavity heavy ion beam testing at GSI," *J. Phys. Conf. Ser.*, vol. 1067, p. 052007, 2018.

[13] F. Dziuba, K. Aulenbacher, W. Barth, M. Basten, C. Burandt, *et al.*, "Further RF measurements on the superconducting 217 MHz CH demonstrator cavity for a CW linac at GSI," *J. Phys. Conf. Ser.*, vol. 1350, p. 012185, 2019.

[14] S. Minaev, U. Ratzinger, H. Podlech, M. Busch, and W. Barth, "Superconducting, energy variable heavy ion linac with constant β, multicell cavities of CH-type," *Phys. Rev. ST Accel. Beams*, vol. 12, p. 120101, 2009.

[15] H. Podlech, U. Ratzinger, H. Klein, C. Commenda, H. Liebermann, *et al.*, "Superconducting CH structure," *Phys. Rev. ST Accel. Beams*, vol. 10, 2007.

[16] M. Gusarova, W. Barth, S. Yaramyshev, M. Miski-Oglu, M. Basten, *et al.*, "Design of the two-gap superconducting re-buncher," *J. Phys. Conf. Ser.*, vol. 1067, p. 082005, 2018.

[17] K. Taletskiy, M. Gusarova, W. Barth, M. Basten, M. Busch, *et al.*, "Comparative study of low beta multi-gap superconducting bunchers," *J. Phys. Conf. Ser.*, vol. 1067, p. 082006, 2018.

[18] S. Polozov and A. Fertman, "High-energy Proton beam accelerators for subcritical nuclear reactors," *At. Energ.*, vol. 113, pp. 192–200, 2013.

[19] Z. Wang, Y. He, H. Jia, W. Dou, W. Chen, *et al.*, "Beam commissioning for a superconducting Proton linac," *Phys. Rev. Accel. Beams*, vol. 19, p. 120101, 2016.

[20] I. Mardor, O. Aviv, M. Avrigeanu, D. Berkovits, A. Dahan, *et al.*, "The Soreq Applied Research Accelerator Facility (SARAF): Overview, research programs and future plans," *The European Physical Journal A*, vol. 54, no. 5, p. 91, 2018.

[21] L. V. Grigorenko, B. Y. Sharkov, A. S. Fomichev, A. L. Barabanov, W. Barth, *et al.*, "Scientific program of DERICA – Prospective accelerator and storage ring facility for radioactive ion beam research," *Physics-Uspekhi*, vol. 62, no. 7, pp. 675–690, 2019.

[22] Y. Iwata, S. Yamada, T. Murakami, T. Fujimoto, T. Fujisawa, *et al.*, "Performance of a compact injector for heavy-ion medical accelerators," *Nucl. Instrum. Methods Phys. Res. A*, vol. 572, no. 3, pp. 1007–1021, 2007.

[23] R. Laxdal, K. Fong, M. Laverty, A. Mitra, R. Poirier, *et al.*, "Recent progress in the superconducting RF program at TRIUMF/ISAC," *Physica C: Superconductivity*, vol. 441, pp. 13–20, 2006.

[24] A. E. Aksent'ev, K. A. Aliev, I. A. Ashanin, Y. A. Bashmakov, A. A. Blinnikov, *et al.*, "Modeling of Proton beam dynamics in an accelerator-driver at 600-1000 MeV and investigation of the electrodynamic characteristics of accelerating cavities," *At. Energ.*, vol. 117, no. 5, pp. 347–356, 2015.

[25] F. Dziuba, M. Busch, M. Amberg, H. Podlech, C. Zhang, *et al.*, "Development of superconducting crossbar-H-mode cavities for Proton and ion accelerators," *Phys. Rev. ST Accel. Beams*, vol. 13, no. 4, 2010.

[26] G. Clemente, U. Ratzinger, H. Podlech, L. Groening, R. Brodhage, *et al.*, "Development of room temperature crossbar-H-mode cavities for Proton and ion acceleration in the low to medium beta range," *Phys. Rev. ST Accel. Beams*, vol. 14, no. 11, 2011.

[27] P. Ostroumov and F. Gerigk, "Superconducting Hadron linacs," *Reviews of Accelerator Science and Technology*, vol. 06, pp. 171–196, 2013.

[28] R. Berezov, O. Delferriere, J. Fils, Y. Gauthier, R. Hollinger, *et al.*, "Status of high intensity Proton injector for Facility for Antiproton and Ion Research," *Rev. Sci. Instrum.*, vol. 90, no. 12, p. 123309, 2019.

[29] W. Barth, A. Adonin, S. Appel, P. Gerhard, M. Heilmann, *et al.*, "Heavy ion linac as a high current Proton beam injector," *Phys. Rev. ST Accel. Beams*, vol. 18, p. 050102, 2015.

[30] A. Adonin, W. Barth, F. Heymach, R. Hollinger, H. Vormann, *et al.*, "Production of high current Proton beams using complex H-rich molecules at GSI," *Rev. Sci. Instrum.*, vol. 87, p. 02B709, 2016.

[31] F. Herfurth, Z. Andelkovic, W. Barth, W. Chen, L. Dahl, *et al.*, "The HITRAP facility for slow highly charged ions," *Physica Scripta*, vol. T166, p. 014065, 2015.

[32] S. Busold, A. Almomani, V. Bagnoud, W. Barth, S. Bedacht, *et al.*, "Shaping laser accelerated ions for future applications – The LIGHT collaboration," *Nucl. Instrum. Methods Phys. Res. A*, vol. 740, pp. 94–98, 2014.

[33] A. Ghiorso, T. Sikkeland, A. E. Larsh, and R. M. Latimer, "New element, Lawrencium, atomic number 103," *Phys. Rev. Lett.*, vol. 6, no. 9, pp. 473–475, 1961.

[34] P. Schwerdtfeger, O. R. Smits, and P. Pyykkö, "The periodic table and the physics that drives it," *Nature Reviews Chemistry*, vol. 4, no. 7, pp. 359–380, 2020.

[35] M. Schädel, "Chemistry of the superheavy elements," *Philos. Trans. Royal Soc. A*, vol. 373, no. 2037, p. 20140191, 2015.

[36] Y. T. Oganessian, F. S. Abdullin, P. D. Bailey, D. E. Benker, M. E. Bennett, *et al.*, "Synthesis of a new element with atomic number $Z = 117$," *Phys. Rev. Lett.*, vol. 104, no. 14, p. 142502, 2010.

[37] J. Khuyagbaatar, A. Yakushev, C. E. Düllmann, D. Ackermann, L. L. Andersson, *et al.*, "^{48}Ca $+^{249}$ Bk Fusion reaction ceading to element $Z = 117$: Long-lived α-decaying ^{270}Db and discovery of ^{266}Lr," *Phys. Rev. Lett.*, vol. 112, no. 17, p. 172501, 2014.

[38] Y. T. Oganessian, V. K. Utyonkov, Y. V. Lobanov, F. S. Abdullin, A. N. Polyakov, *et al.*, "Synthesis of the isotopes of elements 118 and 116 in the ^{249}Cf and ^{245}Cm $+^{48}$ Ca fusion reactions," *Phys. Rev. C*, vol. 74, no. 4, p. 044602, 2006.

[39] H. Albers, J. Khuyagbaatar, D. Hinde, I. Carter, K. Cook, *et al.*, "Zeptosecond contact times for element $Z = 120$ synthesis," *Phys. Lett. B*, vol. 808, p. 135626, 2020.

[40] K. Aulenbacher, J. Dietrich, and W. Klag, "Status of the turbine driven HV-generator for a relativistic electron cooler," in *Proc. 12th International Workshop on Beam Cooling and Related Topics*, 2019.

[41] T. Stengler, *Entwicklung eines supraleitenden Beschleunigermoduls für den rezirkulierenden Betrieb am Mainz Energy-Recovering Superconducting Accelerator (MESA)*. PhD thesis, Johannes Gutenberg-Universität Mainz, 2020.

[42] T. Beiser, K. Aulenbacher, M.-W. Bruker, and J. Dietrich, "Preliminary studies of beam-induced fluorescence and status of the beam-current upgrade of the electron-cooler test-bench at HIM," in *Proc. 12th International Workshop on Beam Cooling and Related Topics*, 2019.

[43] W. Barth, R. Hollinger, A. Adonin, M. Miski-Oglu, U. Scheeler, *et al.*, "LINAC developments for heavy ion operation at GSI and FAIR," *Journal of Instrumentation*, vol. 15, no. 12, p. T12012, 2020.

[44] M. Miski-Oglu, K. Aulenbacher, W. Barth, M. Basten, C. Burandt, *et al.*, "Progress in SRF CH-cavities for the HELIAC CW linac at GSI," in *Proc. IPAC'19*, 2019.

[45] "FAIR overview." `https://www.gsi.de/en/researchaccelerators/fair/the_machine`. Accessed: 2021-12-06.

[46] P. Spiller, R. Balss, P. Bartolome, J. Blaurock, U. Blell, *et al.*, "The FAIR heavy ion synchrotron SIS100," *Journal of Instrumentation*, vol. 15, no. 12, pp. T12013–T12013, 2020.

[47] S. Lauber, K. Aulenbacher, W. Barth, F. Dziuba, J. List, *et al.*, "Longitudinal phase space reconstruction for a heavy ion accelerator," *Phys. Rev. Accel. Beams*, vol. 23, no. 11, p. 114201, 2020.

[48] S. Lauber, K. Aulenbacher, W. Barth, M. Basten, C. Burandt, *et al.*, "A dynamic collimation and alignment system for the Helmholtz Linear Accelerator," *Rev. Sci. Instrum.*, vol. 92, no. 11, p. 113306, 2021.

[49] S. Lauber *et al.*, "An alternating phase focusing injector or heavy ion acceleration," (submitted to NIMA).

[50] M. Basten, *Entwicklung und Inbetriebnahme zweier supraleitender 217 MHz CH-Strukturen für das HELIAC-Projekt*. PhD thesis, Goethe University Frankfurt, 2019.

[51] F. D. Dziuba, *"Entwicklung und Test einer supraleitenden 217 MHz CH-Kavität für das Demonstrator-Projekt an der GSI"*. PhD thesis, Goethe University Frankfurt, 2017.

[52] U. Ratzinger, *Effiziente Hochfrequenz-Linearbeschleuniger für leichte und schwere Ionen*. IAP, Goethe University, Frankfurt am Main, Germany, 1998. Habilitation.

[53] U. Ratzinger and R. Tiede, "Status of the HIIF RF linac study based on H-mode cavities," *Nucl. Instrum. Methods Phys. Res. A*, vol. 415, no. 1, pp. 229–235, 1998.

[54] F. Dziuba, M. Amberg, K. Aulenbacher, W. Barth, M. Basten, *et al.*, "First cold tests of the superconducting CW demonstrator at GSI," in *Proc. RuPAC'16*, pp. 83–85, 2017.

[55] P. Gerhard, W. Barth, L. Dahl, A. Orzhekhovskaya, K. Tinschert, *et al.*, "Commissioning of a new CW radio frequency quadrupole at GSI," in *Proc. IPAC'10*, pp. 741–743, 2010.

[56] R. Tiede, U. Ratzinger, H. Podlech, C. Zhang, and G. Clemente, "KONUS beam dynamics designs using H-mode cavities," in *Proc. HB'08*, pp. 223–230, 2008.

[57] J. Klabunde, "The high charge state injector for GSI," in *Proc. LINAC'92*, pp. 570–574, 1992.

[58] A. Feschenko, "Methods and instrumentation for bunch shape measurements," in *Proc. PAC'01*, pp. 517–521, 2001.

[59] G. Riehl, J. Pozimski, W. Barth, and H. Klein, "A multi-functional profile and emittance measurement system," in *Proc. EPAC'90*, pp. 756–757, 1990.

[60] S. Yaramyshev, W. Barth, L. Groening, A. Kolomiets, and T. Tretyakova, "Development of the versatile multi-particle code DYNAMION," *Nucl. Instrum. Methods Phys. Res. A*, vol. 558, no. 1, pp. 90–94, 2006.

[61] S. Yaramyshev, K. Aulenbacher, W. Barth, M. Basten, M. Busch, *et al.*, "Advanced approach for beam matching along the multi-cavity SC CW linac at GSI," *J. Phys. Conf. Ser.*, vol. 1067, p. 052005, 2018.

[62] R. Scrivens, "Classification of ion sources," Tech. Rep. CERN-2013-007.9, CERN, 2014.

[63] M. Reiser, *Theory and design of charged particle beams*, vol. 2. John Wiley & Sons, Ltd, 2008.

[64] P. Spädtke and K. Tinschert, "2D and 3D simulation of ion beam extraction from the ECR ion source," in *Proc. 14th International Workshop on ECR Ion Sources*, p. 143, 1999.

[65] K. Tinschert, R.Lang, J. Mäder, J. Roßbach, P. Spädtke, *et al.*, "Ion beam production from rare isotopes with GSI ECR ion sources," in *Proc. ECRIS08*, pp. 97–101, 2008.

[66] A. Schempp, "Radio-frequency quadrupole linacs," Tech. Rep. CERN-2005-003.305, CERN, 2005.

[67] I. Kapchinskiy and V. Teplyakov, "Linear ion acceleratorwith spatially homogeneous focusing," *Pribory TekhnikaEksperimenta*, vol. 119, no. 2, pp. 19–22, 1970.

[68] K. R. Crandall, R. H. Stokes, and T. P. Wangler, "RF quadrupole beam dynamics design studies," in *Proc. Linear Accelerator Conference*, pp. 205–216, 1979. CONF-790927-17.

[69] T. P. Wangler, *RF linear accelerators.* John Wiley & Sons, Ltd, 2008.

[70] R. Wideröe, "Über ein neues Prinzip zur Herstellung hoher Spannungen," *Archiv für Elektrotechnik*, vol. 21, no. 4, pp. 387–406, 1928.

[71] J. P. Blewett, "Linear accelerator injectors for Proton-synchrotrons," *CERN Symposium on High Energy Accelerators and Pion Physics*, 1956.

[72] M. Bres, A. Chabert, F. Foret, D. T. Tran, and G. Voisin, "The interdigital H-type (IH) structure, an accelerating structure for low energy beams," *Particle Accelerators*, vol. 2, pp. 17–29, 1971.

[73] S. S. Kurennoy, L. J. Rybarcyk, J. F. O'Hara, E. R. Olivas, and T. P. Wangler, "H-mode accelerating structures with permanent-magnet quadrupole beam focusing," *Phys. Rev. ST Accel. Beams*, vol. 15, no. 9, p. 090101, 2012.

[74] U. Ratzinger, "H-type linac structures," Tech. Rep. CERN-2005-003.351, CERN, 2005.

[75] A. Facco, "Low- to medium-β cavities for heavy ion acceleration," *Superconductor Science and Technology*, vol. 30, no. 2, p. 023002, 2016.

[76] H. Podlech, "Superconducting versus normal conducting cavities," Tech. Rep. CERN-2013-001.151, CERN, 2013.

[77] H. Padamsee, T. Hays, and J. Knobloch, *RF superconductivity for accelerators*. John Wiley & Sons, Ltd, 1998.

[78] H. Podlech, *Entwicklung von normal- und supraleitenden CH-Strukturen zur effizieten Beschleunigung von Protonen und Ionen*. IAP, Goethe University, Frankfurt am Main, Germany, 2008. Habilitation.

[79] W. D. Kilpatrick, "Criterion for vacuum sparking designed to include both RF and DC," *Rev. Sci. Instrum.*, vol. 28, no. 10, pp. 824–826, 1957.

[80] H. Wiedemann, *Particle accelerator physics*, vol. 4. Springer International Publishing, 2015.

[81] R. Crandall, K. and P. Rusthoi, D., "TRACE-3D User's manual," Tech. Rep. LA-UR-97-886, Los Alamos National Laboratory, 1997.

[82] E. Courant and H. Snyder, "Theory of the alternating-gradient synchrotron," *Annals of Physics*, vol. 3, no. 1, pp. 1–48, 1958.

[83] P. M. Lapostolle, "Possible emittance increase through filamentation due to space charge in continuous beams," *IEEE Transactions on Nuclear Science*, vol. 18, no. 3, pp. 1101–1104, 1971.

[84] F. J. Sacherer, "RMS envelope equations with space charge," *IEEE Transactions on Nuclear Science*, vol. 18, no. 3, pp. 1105–1107, 1971.

[85] I. M. Kapchinskiy and V. V. Vladimirsky in *Proc. Conference on High Energy Accelerators and Instrumentation*, (Geneva, CERN), p. 274, 1959.

[86] A. Shor, G. Feinberg, S. Halfon, and D. Berkovits, "SARAF simulations with 6D waterbag and gaussian distributions," Tech. Rep. INIS-IL–011, Soreq NRC, Israel, 2004.

[87] J. Struckmeier, J. Klabunde, and M. Reiser, "On the stability and emittance growth of different particle phase-space distributions in a long magnetic quadrupole channel," *Particle Accelerators*, vol. 15, no. 1, pp. 47–65, 1984.

[88] R. W. Garnett and T. P. Wangler, "A design approach for superconducting high-current ion linacs," in *Proc. LINAC'96*, 1996.

[89] R. Tiede, G. Clemente, H. Podlech, U. Ratzinger, A. C. Sauer, *et al.*, "LORASR code development," in *Proc. EPAC'06*, vol. C060626, pp. 2194–2196, 2006.

[90] J. H. Adlam, "A method of simultaneously focusing and accelerating a beam of Protons," *AERE GP/M*, no. 146, 1953.

[91] M. L. Good, "Phase-reversal focusing in linear accelerators," *Phys. Rev.*, vol. 92, p. 538, 1953. Berkeley Radiation Laboratory report.

[92] I. B. Fainberg, "Alternating phase focusing," in *Proc. Conf. on High Energy Accelerators*, (CERN, Geneva, Switzerland), 1956.

[93] I. M. Kapchinskiy, *Theory of linear resonance accelerators*. United States: Harwood Academic Pub, 1985.

[94] V. Kapin, Y. Iwata, and S. Yamada, "Effects of field distortions in IH-APF linac," *Proc. RuPAC*, pp. 459–461, 2004.

[95] U. Niedermayer, T. Egenolf, O. Boine-Frankenheim, and P. Hommelhoff, "Alternating-phase focusing for dielectric-laser acceleration," *Phys. Rev. Lett.*, vol. 121, no. 21, p. 214801, 2018.

[96] G. N. Kropachev, *Focusing of charged particles in linear accelerator*. Phd thesis, ITEP, Moscow, 1994. UDK:621.384.64.

[97] D. A. Swenson, "Alternating phase focused linacs," in *Particle Accelerators*, vol. 7, pp. 61–67, 1976.

[98] T. Hattori, K. Yamamoto, N. Hayashizaki, H. Kashiwagi, Y. Takahashi, *et al.*, "A study of a test APF-IH type linac as an injector for cancer therapy," *Nucl. Instrum. Methods Phys. Res. B*, vol. 188, no. 1, pp. 221–224, 2002.

[99] M. Otani, T. Mibe, M. Yoshida, K. Hasegawa, Y. Kondo, *et al.*, "Interdigital H-mode drift-tube linac design with alternative phase focusing for Muon linac," *Phys. Rev. Accel. Beams*, vol. 19, no. 4, p. 040101, 2016.

[100] Y. Iwata, S. Yamada, T. Murakami, T. Fujimoto, T. Fujisawa, *et al.*, "Alternating-phase-focused IH-DTL for an injector of heavy-ion medical accelerators," *Nucl. Instrum. Methods Phys. Res. A*, vol. 569, no. 3, pp. 685–696, 2006.

[101] Y. Nakazawa, H. Iinuma, Y. Iwata, Y. Iwashita, M. Otani, *et al.*, "Development of inter-digital H-mode drift-tube linac prototype with alternative phase focusing for a Muon linac in the J-PARC Muon G-2/EDM experiment," *J. Phys. Conf. Ser.*, vol. 1350, p. 012054, 2019.

[102] X. Li, Y. Pu, F. Yang, X. Xie, Q. Gu, *et al.*, "RF design and study of a 325 MHz 7 MeV APF IH-DTL for an injector of a Proton medical accelerator," *Nuclear Science and Techniques*, vol. 30, no. 9, p. 135, 2019.

[103] A. Adelmann *et al.*, "OPAL A versatile tool for charged particle accelerator simulations," *Journal of Computational Physic*, 2019.

[104] V. Aseev, P. Ostroumov, E. Lessner, and B. Mustapha, "TRACK: The new beam dynamics code," in *Proc. PAC'05*, pp. 2053–2055, 2005.

[105] H. Grote and F. Schmidt, "Mad-X - An upgrade from mad8," in *Proc. PAC'03*, vol. 5, pp. 3497–3499, 2003.

[106] D. Uriot and N. Pichoff, *TraceWin*, 2015.

[107] K. Makino and M. Berz, "COSY INFINITY Version 9," *Nucl. Instrum. Methods Phys. Res. A*, vol. 558, pp. 346–350, 2006.

[108] S. Yaramyshev, W. Barth, G. Clemente, L. Dahl, V. Gettmann, *et al.*, "A new design of the RFQ channel for GSI HITRAP facility," in *Proc. LINAC'12*, 2012.

[109] J. C. Butcher, *The numerical analysis of ordinary differential equations: Runge-Kutta and general linear methods*. USA: Wiley-Interscience, 1987.

[110] J.-B. Lallement, G. Bellodi, V. Dimov, A. Lombardi, and M. Yarmohammadi Satri, "Linac4 transverse and longitudinal emittance reconstruction in the presence of space charge," in *Proc. LINAC'14*, pp. 913–915, 2014.

[111] K. Hock, M. Ibison, D. Holder, B. Muratori, A. Wolski, *et al.*, "Beam tomography research at Daresbury laboratory," *Nucl. Instrum. Methods Phys. Res. A*, vol. 753, pp. 38–55, 2014.

[112] R. Gordon, R. Bender, and G. Herman, "Algebraic reconstruction technique (ART) for three-dimensional electron microscopy and X-ray photography," *Journal of Theoretical Biology*, vol. 29, pp. 471–476, 1971.

[113] D. Malyutin, M. Gross, I. Isaev, M. Khojoyan, G. Kourkafas, *et al.*, "Longitudinal phase space tomography using a booster cavity at PITZ," *Nucl. Instrum. Methods Phys. Res. A*, vol. 871, pp. 105–112, 2017.

[114] C. L. Lawson and R. J. Hanson, *Solving least squares problems*. Philadelphia, PA, USA: Society for Industrial and Applied Mathematics, 1987.

[115] J. Radon, "Über die Bestimmung von Funktionen durch ihre Integralwerte längs gewisser Mannigfaltigkeiten," *Akad. Wiss.*, vol. 69, pp. 262–277, 1917.

[116] D. E. Dudgeon and R. M. Mersereau, *Multidimensional digital signal processing*. Prentice Hall Professional Technical Reference, 1990.

[117] S. Kaczmarz, "Angenäherte Auflösung von Systemen linearer Gleichungen," *Bulletin International de l'Académie Polonaise des Sciences et des Lettres. Classe des Sciences Mathématiques et Naturelles. Série A, Sciences Mathématiques*, vol. 35, pp. 355–357, 1937.

[118] P. Virtanen, R. Gommers, T. E. Oliphant, M. Haberland, T. Reddy, *et al.*, "SciPy 1.0: Fundamental algorithms for scientific computing in Python," *Nature Methods*, vol. 17, pp. 261–272, 2020.

[119] S. Gavrilov, A. Feschenko, and D. Chermoshentsev, "Bunch shape monitors for modern ion linacs," *Journal of Instrumentation*, vol. 12, no. 12, pp. P12014–P12014, 2017.

[120] R. Singh, S. Lauber, W. Barth, P. Forck, M. Miski-Oglu, *et al.*, "Comparison of Feschenko BSM and fast faraday cup with low energy ion beams," in *Proc. IBIC'21*, 2021.

[121] S. Glantz and B. Slinker, *Primer of applied regression & analysis of variance*. McGraw-Hill Education, 2000.

[122] B. Walasek-Hoehne, C. Andre, P. Forck, E. Guetlich, G. Kube, *et al.*, "Scintillating screen applications in accelerator beam diagnostics," *IEEE Transactions on Nuclear Science*, vol. 59, no. 5, 2, pp. 2307–2312, 2012.

[123] T. Giacomini, S. Barabin, P. Forck, D. Liakin, and V. Skachkov, "Development of residual gas profile monitors at GSI," in *AIP Conf. Proc.*, vol. 732 of *Beam Instrumentation Workshop 2004*, pp. 286–293, 2004.

[124] T. Sieber, W. Barth, F. Dziuba, A. Feschenko, P. Forck, *et al.*, "Bunch shape measurements at the GSI CW-linac prototype," in *Proc. IPAC'18*, pp. 2091–2094, 2018.

[125] M. Vossberg, A. Schempp, C. Zhang, W. Barth, and L. Dahl, "The new GSI HLI-RFQ for CW-operation," in *Proc. LINAC'11*, pp. 494–496, 2011.

[126] "CST MicroWave Studio." `https://www.cst.com`. Accessed: 2021-07-21.

[127] M. Basten *et al.*, "Continuous wave interdigital H-mode cavities for alternating phase focusing heavy ion acceleration," (submitted to RSI).

[128] I. Pinayev, Y. Jing, D. Kayran, V. N. Litvinenko, J. Ma, *et al.*, "Using solenoid as multipurpose tool for measuring beam parameters," *Rev. Sci. Instrum.*, vol. 92, no. 1, p. 013301, 2021.

[129] O. Brunner, S. Calatroni, E. Ciapala, M. Eshraqi, R. Garoby, *et al.*, "Assessment of the basic parameters of the CERN superconducting Proton linac," *Phys. Rev. ST Accel. Beams*, vol. 12, no. 7, p. 070402, 2009.

[130] V. Palmieri, A. Porcellato, V. Ruzinov, S. Stark, L. Badan, *et al.*, "Installation in the LNL ALPI linac of the first cryostat with four Niobium quarter wave resonators," *Nucl. Instrum. Methods Phys. Res. A*, vol. 382, no. 1, pp. 112–117, 1996.

[131] P. Forck, "Minimal invasive beam profile monitors for high intense Hadron beams," in *Proc. IPAC'10*, pp. 1261–1265, 2010.

[132] B. Ledroit and K. Aulenbacher, "Collimation of target induced halo following MAGIX at MESA," *J. Phys. Conf. Ser.*, vol. 1350, p. 012138, 2019.

[133] V. Rizzoglio, A. Adelmann, C. Baumgarten, M. Frey, A. Gerbershagen, *et al.*, "Evolution of a beam dynamics model for the transport line in a Proton therapy facility," *Phys. Rev. Accel. Beams*, vol. 20, no. 12, p. 124702, 2017.

[134] L. Arnaudon, O. Aberle, R. Assmann, J. Bacher, V. Baglin, *et al.*, "Linac4 technical design report," Tech. Rep. CERN-AB-2006-084, CERN, 2006.

[135] R. Miyamoto, H. Danared, M. Eshraqi, and A. Ponton, "Numerical study of a collimation system to mitigate beam losses in the ESS linac," in *Proc. IPAC'12*, 2012.

[136] M. Yarmohammadi Satri, A. M. Lombardi, and F. Zimmermann, "Multiobjective genetic algorithm approach to optimize beam matching and beam transport in high-intensity Hadron linacs," *Phys. Rev. Accel. Beams*, vol. 22, no. 5, p. 054201, 2019.

[137] V. A. P. Aguiar, N. H. Medina, N. Added, E. L. A. Macchione, S. G. Alberton, *et al.*, "SAFIIRA: A heavy-ion multi-purpose irradiation facility in Brazil," *Rev. Sci. Instrum.*, vol. 91, no. 5, p. 053301, 2020.

[138] O. Romanenko, V. Havranek, A. Mackova, M. Davidkova, M. Cutroneo, *et al.*, "Performance and application of heavy ion nuclear microbeam facility at the nuclear physics institute in Řež, Czech Republic," *Rev. Sci. Instrum.*, vol. 90, no. 1, p. 013701, 2019.

[139] K. Yamamoto, S. Kato, H. Harada, M. Yoshimoto, Y. Yamazaki, *et al.*, "Performance of the beam collimation system in the J-PARC RCS," *Prog. Nucl. Sci. Tech.*, vol. 4, pp. 243–246, 2014.

[140] F. Gao and L. Han, "Implementing the Nelder-Mead simplex algorithm with adaptive parameters," *Computational Optimization and Applications*, vol. 51, no. 1, pp. 259–277, 2012.

[141] M. Miski-Oglu, M. Amberg, K. Aulenbacher, V. Gettmann, W. Barth, *et al.*, "Steps towards superconducting CW-linac for heavy ions at GSI," in *Proc. SRF'15*, 2015.

Curriculum Vitae

This page intentionally left blank.

This page intentionally left blank.

This page intentionally left blank.

This page intentionally left blank.

This page intentionally left blank.